Design and Fabrication of an Open-Architecture Selective Laser Melting System

by

Stuart Polak Baker

B.S. Mechanical Engineering
B.S. Electrical Engineering
United States Military Academy, 2014

Submitted to the Department of Electrical Engineering and Computer Science
in partial fulfillment of the requirements for the degree of

Master of Science in Electrical Engineering and Computer Science

at the

MASSACHUSETTS INSTITUTE OF TECHNOLOGY

February 2017

Signature of Author .... Signature redacted .....
Department of Electrical Engineering and Computer Science
January 31, 2017

Certified by..... Signature redacted .....
A. John Hart
Associate Professor of Mechanical Engineering
Thesis Supervisor

Accepted by ..... Signature redacted .....
Leslie A. Kolodziejski
Chair, Department Committee on Graduate Students

Design and Fabrication of an Open-Architecture Selective Laser Melting System

by

Stuart Polak Baker

Submitted to the Department of Electrical Engineering and Computer Science
on January 31, 2017, in partial fulfillment of the
requirements for the degree of
Master of Science in Electrical Engineering and Computer Science

Abstract

Additive manufacturing (AM) is a rapidly advancing manufacturing paradigm that involves selective placement of material, layer-by-layer, as determined by a three-dimensional digital model. AM allows for freeform geometries and optimized structures that are impractical or impossible to create with traditional manufacturing practices. Among several mainstream AM methods, powder bed fusion is compatible with both plastics and metals, and thereby allows construction of a wide spectrum of end-use parts. A significant challenge in exploring this process from a research perspective is the predominance of commercial systems which are costly and offer limited flexibility to the user. To address this challenging lack of access, this thesis develops a low-cost and open-architecture laser powder bed fusion metal printer to enable the exploration of new materials and process concepts. Starting with a broad review of additive manufacturing, this thesis then explains the powder bed fusion process and reviews the design considerations for powder bed fusion equipment. This understanding is then applied to design an open-architecture galvanometer-driven optical scanning system. In addition, two deposition chambers are constructed, including a high-pressure vessel with a novel multi-layer recoating build platform that allows for the study of pressure in the powder bed fusion process. The operational performance is then evaluated, and the capability to achieve programmed scanning of the laser is demonstrated through point-wise and raster scan melting.

Thesis Supervisor: A. John Hart
Title: Associate Professor of Mechanical Engineering

Acknowledgments

Graduate school has been an incredible journey of discovery, not just delving into the research side of academia, but also having the experience of living in such a fascinating city. While challenging at every turn, it has been enormously rewarding having the opportunity to study at MIT. This work, and the amazing experience I had during graduate school, was possible only through the help and support of so many people.

- To my advisor John Hart, thank you for welcoming me into your group. As a paragon of hard work, dedication, and scientific excellence, I cannot think of a better role model to aspire towards. Your mentorship throughout my graduate school experience taught me how to ask the right questions when embarking on research and to seek the fundamentals science concepts that underpin every challenge.

- To Martin Feldmann, a inveterate professional and an amazing friend, your counsel throughout this project made it possible to turn a wild idea into an amazing scientific system.

- To Ed Corbett and John Kuconis of Lincoln Laboratory, this work was made possible by your tireless support and funding. Thank you for welcoming me to the lab first as a cadet, and then inviting me back as a researcher.

- To my fellow ACAMers - Jon Gibbs, Ryan Penny, and Yu Zou - thank you for your help and support in building the system, and for a little patience as we worked out the bugs. I look forward to continuing to help grow the system in whatever way I can.

- To my fellow Mechanosynthesis Group members, the say your labmates can make or break your graduate school experience, and you truly made it awesome. Thank you for welcoming me into the group and helping me to succeed in my endeavors, I could not have asked for a better group of people to work with..

- To all of the amazing friends I met on my journey - Ross Finman, Abhinav Rao, Sebastian Claici, Lucy Du, Jamison Go, Andrea Carney, Ahmed Helal - thank you for making graduate school an absolutely amazing experience. I cannot image making it through this academic foray without your help, support, and uplifting shenanigans. Of all of the wonderful experiences of graduate school, what I treasure most are the new friends made and the many adventures embarked upon.

- Lastly, to my parents Brad and Cynthia Baker, thank you for your unconditional love and support. I am eternally grateful for your patience, all those years ago, as I tore apart everything I could get my hands on. That spark of curiosity you nurtured grew into an insatiable thirst for knowledge and a lifelong passion for engineering.

Contents

THIS PAGE INTENTIONALLY LEFT BLANK

List of Figures

THIS PAGE INTENTIONALLY LEFT BLANK

Chapter 1

Introduction

The purpose of this thesis is to develop and demonstrate an inexpensive, open-architecture powder bed fusion additive manufacturing system. Additive manufacturing is a production technique that rapidly produces complex parts with unique geometries that no other manufacturing process can create. Beyond geometry, this technique opens up opportunities to integrate novel materials as well as explore new deposition strategies such as graded material deposition. This thesis contributes a system that is not only an open-architecture tool to help meet the exponentially growing interest in additive manufacturing research, but also a means of reducing the barrier to entry into powder bed fusion research. If additive manufacturing is to be leveraged in addressing the many unique manufacturing challenges facing design engineers, characterizing and understanding the processes is key to maximizing performance. However, central to that advancement in characterization is developing and providing access to the research tools necessary.

1.1 Additive Manufacturing

Additive manufacturing is an emerging paradigm in manufacturing technology that centers on the concept of depositing material to reach the desired shape, as opposed to traditional manufacturing techniques which rely on reshaping or removing the parent material. The ASTM International Subcommittee F42.91, Terminology in Ad-

ditive Manufacturing Technologies, describes additive manufacturing as the process of converting a 3-dimensional model into a physical part by the controlled joining of materials, often in a layer-wise manner [1]. This is in stark comparison to subtractive manufacturing which starts with a large billet of material and then uses successive material removal processes to reduce that billet to the desired shape. Figure 1-1 shows a representation of the difference between additive and subtractive manufacturing.

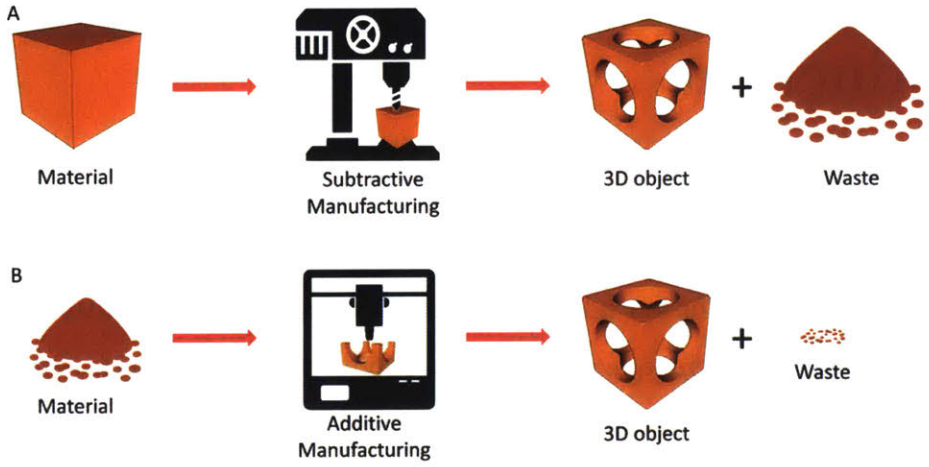

Figure 1-1: Comparison between additive manufacturing and subtractive manufacturing [2].

1.1.1 Types of Additive Manufacturing Processes

The additive manufacturing technology landscape encompasses a broad range of techniques with widely varying mechanisms of operation. One challenge in analyzing the available processes is that the breadth of terminology used can create significant confusion. To address this confusing terminology landscape, ASTM International committee F42 and International Organization for Standardization (ISO) Technical Committee 262 jointly developed ISO/ASTM 52900:2015, a standard for defining the terminology with additive manufacturing [1]. Within this standard, ASTM defines 7 additive manufacturing process categorizations:

- Material Extrusion
- Material Jetting
- Binder Jetting

- Sheet Lamination
- Vat Photopolymerization
- Powder Bed Fusion
- Directed Energy Deposition

This list is meant to be a general categorization for the field, not necessarily a thorough hierarchical structure. As such, there are many derivative or new processes that do not strictly fall within one of the categories listed above.

Extrusion Deposition

Extrusion deposition functions by extruding a continuous filament of material out of an orifice onto a build platform. To generate a 3-dimensional part, this process extrudes material in a layer-wise fashion, repetitively printing a 2-dimensional pattern on top of previously printed layers. These 2-dimensional layers are themselves constructed by continuously extruding the build material along a curvilinear path to create filled structures. Examples of object being constructed via extrusion deposition can be seen in figure 1-2.

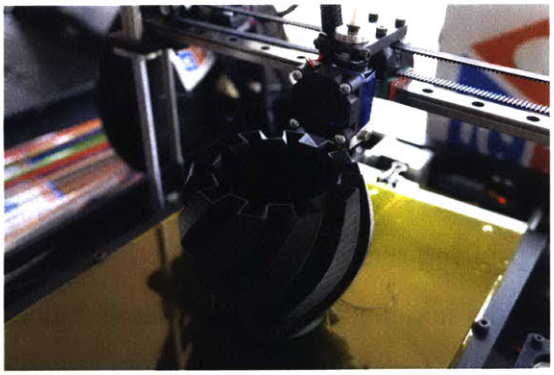

(a)

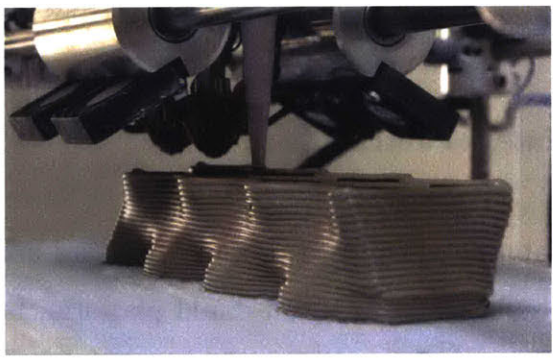

(b)

Figure 1-2: An example of (a) fused deposition modeling on a hobbyist grade printer as well as (b) a system extruding a ceramic paste that is then fired after printing to give a ceramic building brick [3][4].

There are multiple mechanisms through which the material in extrusion deposition can reach the desired mechanical properties, but generally fall into the broad categories of chemically cured or thermally cured. In chemically cured systems, the

feedstock is one or more compounds prepared ahead of printing and are extruded out of a syringe or pressure pump onto the build surface. These materials are deposited in a liquid or gel state and then cure through one of a variety of chemically driven mechanisms such as solvent evaporation, polymer cross-linking, or ceramic curing by firing. In thermally cured systems, referred to as fused deposition modeling (FDM), the desired mechanical characteristics are achieved through heat transfer. With FDM printing, the structural materials are in a category of polymers referred to as thermoplastics, acrylonitrile butadiene styrene (ABS) and polylactic acid (PLA) being two common choices. Thermoplastics are differentiated from other polymers in that they exhibit a melting point, and can transformed into a flowable state for extrusion. This extrudable state is achieved by heating the material above its melting point, often in a small conduction heating chamber which is fed from a spool of thermoplastic filament. Once melted, the plastic is forced through an orifice by the pressure of the feedstock being forced into the melt chamber, extruding it into a filament which is drawn out to create the 2-dimensional build pattern. As the material is deposited, it resolidifies as it cools through heat transfer.

Material Jetting

Material jetting is a process that uses inkjet printing techniques to directly deposit a build material onto a build platform, much like inkjet printing onto paper but in successive layers. Often this process follows the ink deposition with a curing process such as exposure to ultraviolet light for photopolymers. Like other processes, this process deposits material in a layer-wise manner to build up a 3-dimensional part. One advantage of this process is that it can print multiple materials within a single part by using multiple inkjet heads, each loaded with a different material. Another advantage is that this process can create high-resolution parts due to the precision of the inkjet printing process. However, these advantages come with the disadvantages of high machine cost and being limited to specific inks, such jet-able UV-cured inks.

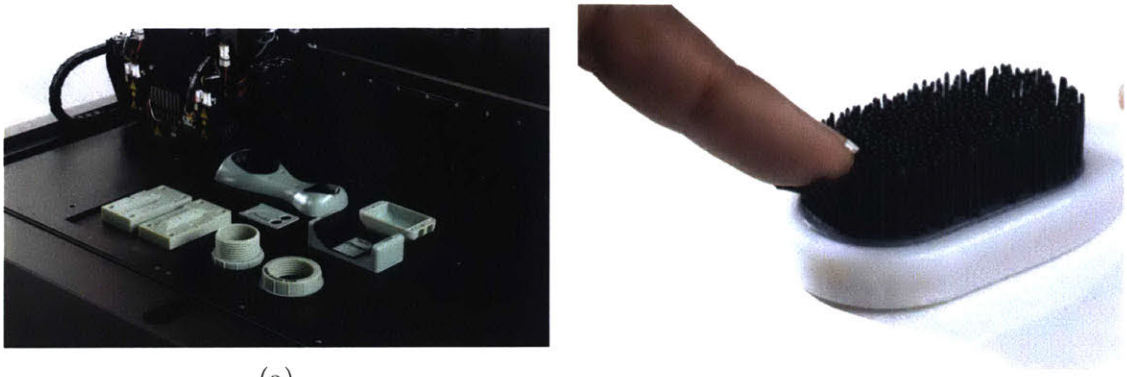

(a) (b)

Figure 1-3: (a) Build platform of a material jetting 3D printer with an assort of fabricated parts and (b) a multi-material part printed using material jetting [5][6].

Binder Jetting

Binder jetting is a process similar to material jetting in that it leveraged inkjet printing techniques to deposit material, but differentiates itself by depositing a binder instead of the structural material. The process starts with a build platform covered with a thin layer of powdered build material, such as plastics or metals. An inkjet head then patterns down an adhesive binder that selectively bonds the powdered build material. An example of a multi-row inkjet head dispensing adhesive can be seen in figure 1-4. A new layer of powder is then deposited, and the process is repeated in a layer-wise fashion to generate a 3-dimensional part. While this process is limited to a single build material because recoating systems can only lay down one material, it does offer the advantage of being a relatively fast process, depending on the size of the inkjet head. One caveat is that the material generally must be post-processed through sintering or material infusion in order to produce the desired mechanical properties.

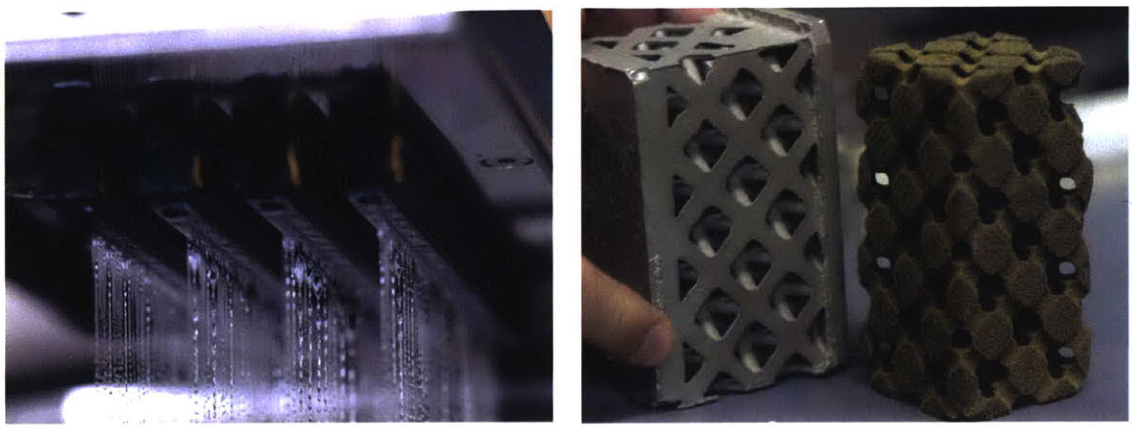

(a) (b)

Figure 1-4: Depiction of (a) multi-jet binder jet print head jetting out the binding medium as well as (b) a binder jet fabricated mold insert (right) with the cast part (left) [5][7].

Sheet Lamination

Sheet lamination is a process that constructs a part from consecutive sheets of build material adhered together in a vertical stack. The process begins with a sheet of the build material that is cut in a pattern representing a 2-dimensional slice of the desired object. This cut sheet is then placed on top of the build platform, or previously laid sheets, to create a 3-dimensional stack. Either during the layering process or after the stack is complete, the layers are adhered together to create a solid part. The method of adhesion varies greatly and includes using adhesive-backed build material, adhesives dispensed between layers, ultrasonic welding of materials, and post-curing with heat. This process has a unique range of materials available due to the widely varying mechanics of the process, including not just metals and plastics, but also organic materials such as paper and composites like fiberglass or carbon fiber that are infused with epoxy. Paper systems can also be combined with inkjet printing to create realistic looking representations as seen in figure 1-5.

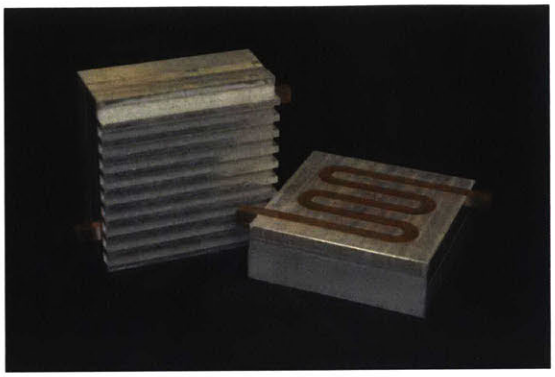

(a)

(b)

Figure 1-5: Parts fabricated with sheet lamination where (a) ultrasonic consolidation is used to fuse layers of aluminum and copper for an integrated heat exchanger and (b) paper is color printed and then glued together to create a grapefruit model [8][9].

Vat Photopolymerization

Also referred to as stereolithography, this is a process that centers on the use of photosensitive polymers that cure when exposed to a specific frequency of light. The process begins with a build platform that has a thin layer of the photopolymer across its surface. An energy source, often a focused ultraviolet or blue laser, rasters across this interface, selectively polymerizing the build material. The build platform is then incremented by the layer height so that a new layer of liquid photopolymer can flow in and create the next layer. In some systems, a blade recoats the surface of either the bottom of the tank or the top of the vat to replenish and smooth the photopolymer. The new layer is then exposed like the last, and the process repeats to create a 3-dimensional part.

One common separating characteristic in vat photopolymerization systems is the distinction between bottom-up and top-down systems. In a bottom-up system, the resin vat has a transparent window integrated into the bottom. The layer of build material is created between the inverted build platform and that transparent window. In contrast, a top-down system does not have this windows and instead submerges the build platform in the resin vat. The build layer is created by the distance between the top of the submerged build platform the top free-surface of resin in the vat. A representation of each type of system can be seen in figure 1-6. To transition to the

next layer, bottom-up systems must first peel the part off of the bottom window and then raise up whereas in a top-down system the build platform is simply lowered down. In both systems, a recoating blade is often used, but for differnet reasons. In bottom-up systems the blade is used to ensure that there is no material adhered to the transparent window as well as ensuring fresh resin flows in. In top-down systems, the blade is used to deposit the resin in an even layer for the next exposure.

Newer systems substitute the point-wise polymerization of the material with a digital light processing (DLP) projector that exposes the entire build surface at the same time to increase build speed. The DLP systems use a digital micromirror device, a micro-opto-electromechanical system, that is constructed of a rectangular array of mirrors that can rotate to turn each pixel on or off. Another method for increasing build speed is the use of an oxygen-permeable window for bottom-up systems that prevents the polymer from adhering to the window as oxygen inhibits polymerization in a thin film above it. This oxygen-inhibition system is referred to as continuous liquid interphase production (CLIP), and has the unique quality of not showing distinct print layers like other systems [10]. Photopolymerization-based processes have the advantage of being able to produce high-resolution parts with sharp features, but are limited to using a single photopolymer at a time and are sensitive to ambient ultraviolet light.

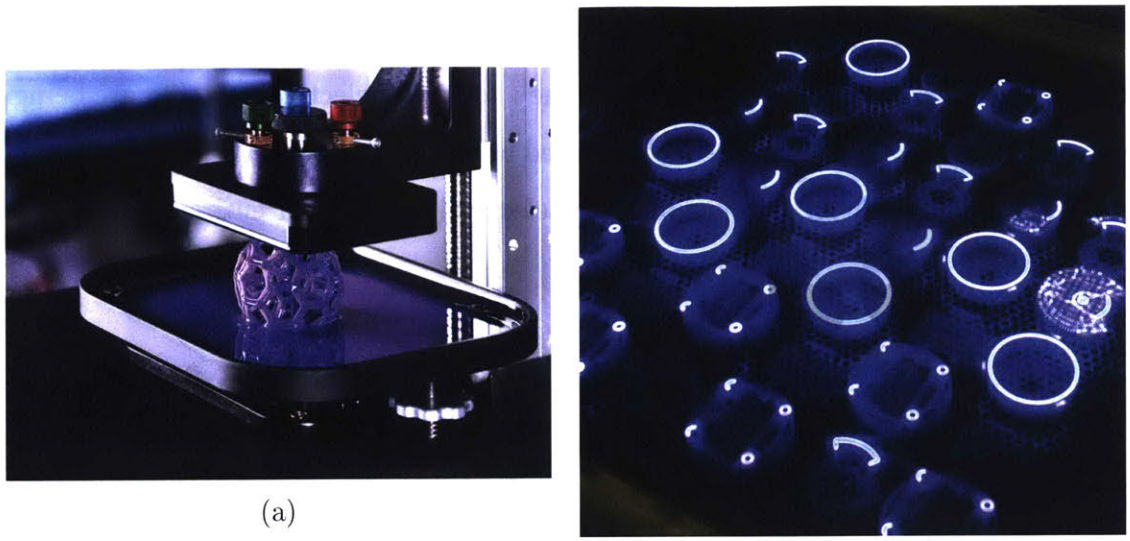

(a) (b)

Figure 1-6: Mid-print depiction of (a) a bottom-up system drawing the part out of the resin as well as (b) a top-down system exposing the top surface of the resin vat to create the next layer in the print [11][12].

Powder Bed Fusion

Powder bed fusion is a process that combines a bed of powdered build material with a directed energy source to selectively sinter or melt the build material. This process may also be referred to as selective laser sintering (SLS), selective laser melting (SLM), direct metal laser sintering (DMLS), or electron beam melting (EBM). To generate a 2-dimensional slice of a 3-dimensional part, a thin layer of powdered build material is spread across a build platform. The energy source is then rastered across the powder, sintering or melting it in selected regions. The build platform is then lowered and a new layer of powder is spread across the previously exposed layer. The process then repeats to generate a stack of 2-dimensional slices which combine to create a full 3-dimensional part. This process is similar to the binder jet printing technique previously mention ed, but instead of adhering the material with adhesive, it sinters or melts the particles together. Also like binder jet printing, this process can handle a wide range of materials from plastic to metals to ceramics, but is generally limited to a single build material at a time. The energy source is most often a high-power laser, as demonstrated by nearly all selective sintering/melting machines, but one notable

exception is a line of machines that substitutes the laser with a high-power electron beam produced by Arcam AB. Additionally, new forms of selective sintering are being explored that involve inkjet depositing infrared absorptive ink and then exposing the surface to high-intensity IR radiation that selectively sinters an entire layer in one exposure.

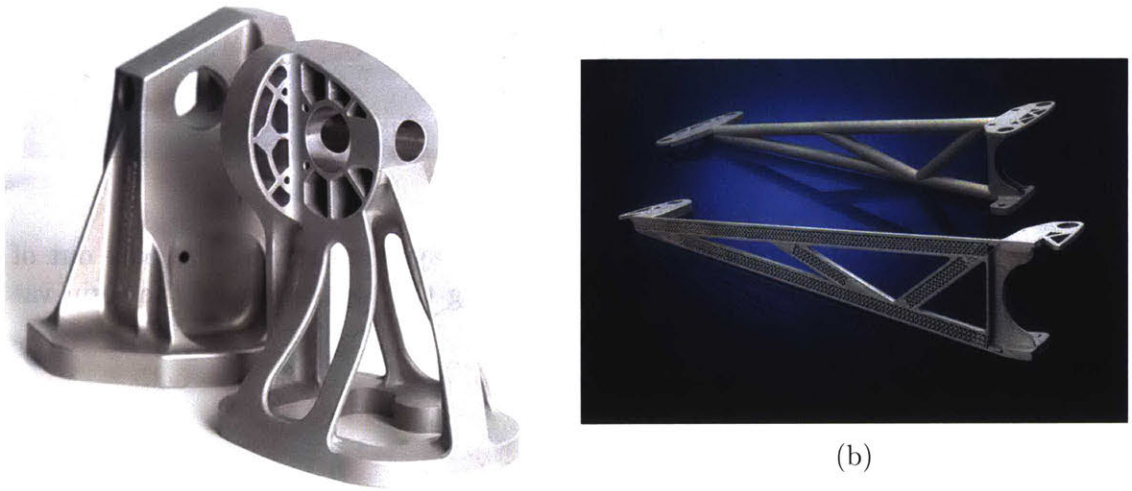

(a) (b)

Figure 1-7: Examples of powder bed fusion printing that demonstrate (a) the 7% weight savings between an optimized freeform fabricated part (front) and a traditionally manufactured part (back) and (b) a lattice structure printed within an enclosed structure [13][14].

Directed Energy Deposition

Directed energy deposition is a technology centered on the combination of an energy source with a projected material stream. The most common form of this process combines a high-power laser source with material nozzles that spray powdered build material in the path of the laser. As the build material moves into the path of the laser, it is melted and then deposited onto the build surface. While lasers are a common energy source, directed energy deposition can also work with electron beams, plasma torches, or even traditional gas torches. Like other point-wise material deposition techniques, such as FDM, this process generates an infilled 2-dimensional shape sliced

from a larger 3-dimensional body, and iteratively stacks those slices to create the desired shape. An interesting capability of using a powdered build material is that multiple materials can be fed through multiple nozzles, allowing for graded material deposition. In different implementations of this process, the laser energy source can be replaced with an electron beam and the powdered build material swapped for a wire feed mechanism. Regardless of the implementation, the build material is nearly always some form of metal. A common application of this technique is to deposit material on to existing objects, which opens up opportunities for repairing damaged parts such as reconstructing a damaged turbine blade from a jet engine as seen in figure 1-8. This freeform deposition does come at the cost of producing a course surface finish due to the large melt pool generated from projecting the material in front of the energy source, often requiring post-processing such as machining to make the part useful. To circumvent this shortcoming, this process is often integrated into subtractive manufacturing systems, such as 5-axis vertical machining centers, to combine additive and subtractive manufacturing [15].

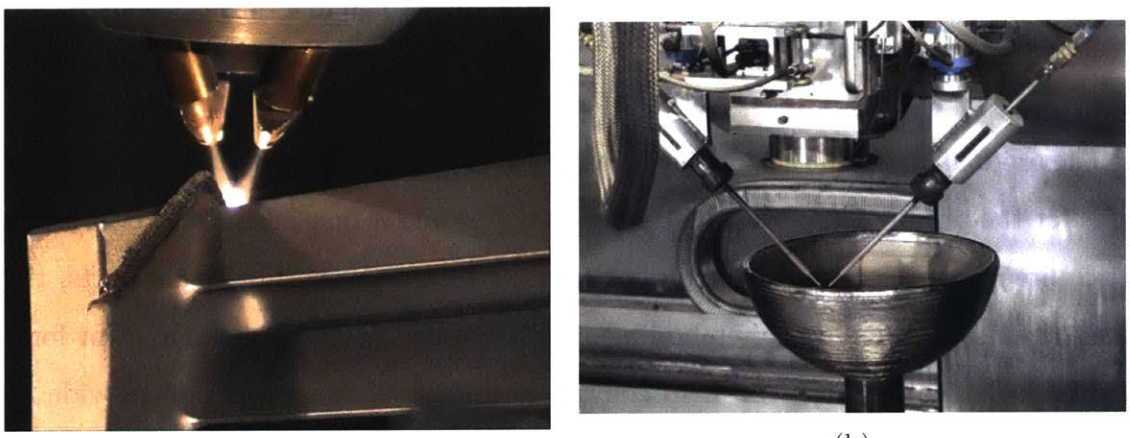

(a) (b)

Figure 1-8: Representations of the DED process where (a) a DED system is used to repair an existing turbine blade and (b) a Sciaky wire-fed e-beam system is manufacturing a titanium pressure vessel for a satellite [16][17].

1.2 Applications, Motivation, and Problems

1.2.1 Applications

The unique characteristics of additive manufacturing process allow for a wide range of applications. The three primary application spaces for additive manufacturing are visual and design aids, molds and tooling, and directly manufactured parts. Figure 1-9 shows the distribution of how companies use additive manufacturing technology in their product development and manufacturing.

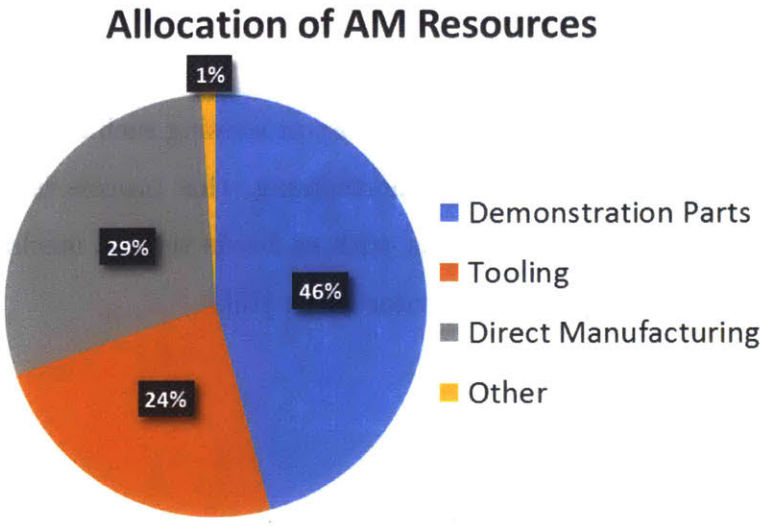

Figure 1-9: Distribution of the application of additive manufacturing resources between major part categories [18].

The original, and still the most popular, reason for leveraging additive manufacturing is for the production of demonstration parts. While it may seem counterintuitive to acquire a large, expensive piece of equipment to create non-functional parts, the advantage lies in the physical embodiment of a design. Having a demonstrator for a complex technical concept can help convey the intent of the design and provide an understanding that is clearer than what would be obtained from engineering drawings. An example of this has been leveraged in the medical community to create models of complex surgical operations so surgeons can better visualize the work they are going to perform [19]. Education and outreach also fall within this realm, additive

manufacturing allows educators to create complex demonstrators for a wide variety of complex scientific and engineering concepts such as biological systems [20]. Another application for a non-functional model is to help the design engineer understand the fit and assembly of the components. By having a physical prototype to manually inspect, an engineer may discover difficulties in assembly or manufacturing that would not be apparent on a screen. This allows engineers to quickly iterate through design concepts and inexpensively optimize the product. Examples of each of these application can be seen below in figure 1-10.

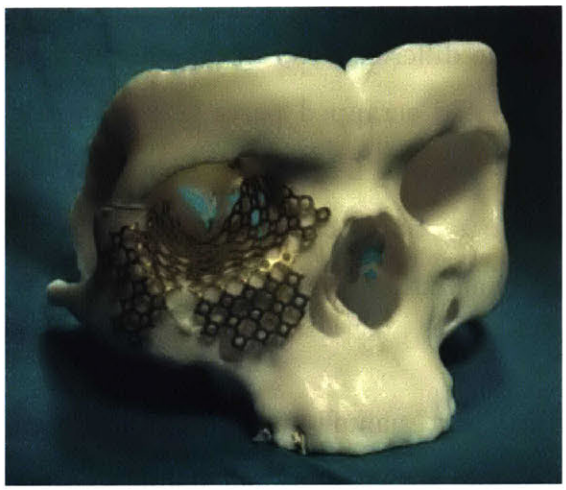

(a)

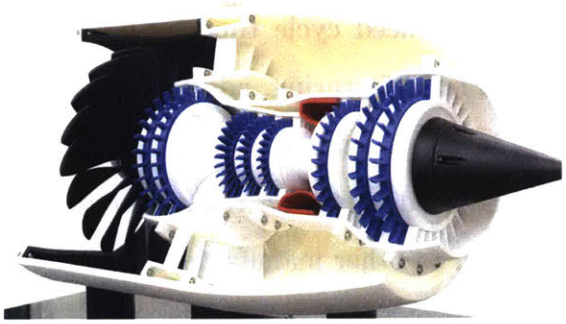

(b)

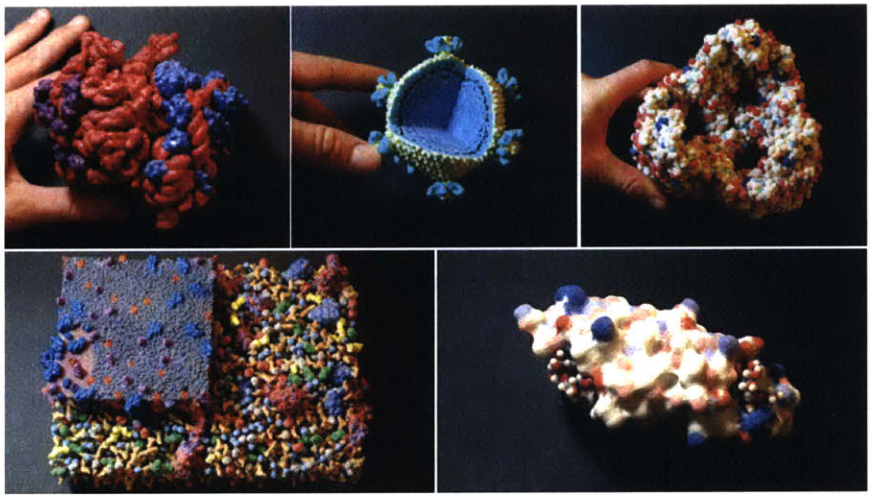

(c)

Figure 1-10: Examples of additive manufacturing for demonstration including (a) a skull used as a surgical training device, (b) a cross-section of a jet turbine engine, and (c) various biological systems [19][21][20].

Additive manufacturing of tooling for manufacturing and assembly is opening up new possibilities for manufacturing customization and efficiency. For prototyping or low-run production in polymers, molds can be directly printed used as fine-tuning tools before the expensive process of cutting metal for a long-run production mold. For metals, consumable molds for investment casting can be printed, providing an alternative to the expensive and slow process of the developing the wax positives, and sand casting molds can be customized for every need. Taking this a step further, metal additive manufacturing can be used for the direct production of tooling components such as molds. These unique molds outperform traditional molds by leveraging embedded channels for optimized cooling, and the difference can be significant, one example reduced cycle time by 60% and eliminated scrapped parts [22]. Outside of parts manufacturing, additively manufactured jigs and fixtures are being used to assist in the assembling and inspection of products. Small changes with additively manufactured parts can reduce monetary and time costs by an order of magnitude compared to other manufacturing methods [18][23].

Additive manufacturing also allows for direct part manufacturing with improved performance by incorporating features not feasible with traditional manufacturing techniques. Optimized channel design that achieve better heat transfer or flow properties hold the potential for significant improvement in fluid applications. The University of Maryland has printed a metal heat exchanger that provides a 20% increase in performance and a 20% decrease in weight over traditional designs [25]. The aerospace industry has a significant interest in additively manufactured parts as it offers the potential to provide better weigh-optimized parts than other manufacturing techniques. An example is GE's LEAP fuel injector nozzle that reduces 18 parts down to 1, eliminates a brazing operation, provides 25% weight savings, and 500% improvement in durability [26]. Another example is an aircraft mounting bracket that achieved a 7% weight reduction compared to its traditionally manufactured counterpart, seen in figure 1-12 [13]. Likewise, the medical and dental industries have started building custom implants using additive manufacturing. Align Technology, the makers of the Invisalign orthodontic aligners, produces 17 million aligners annually, each

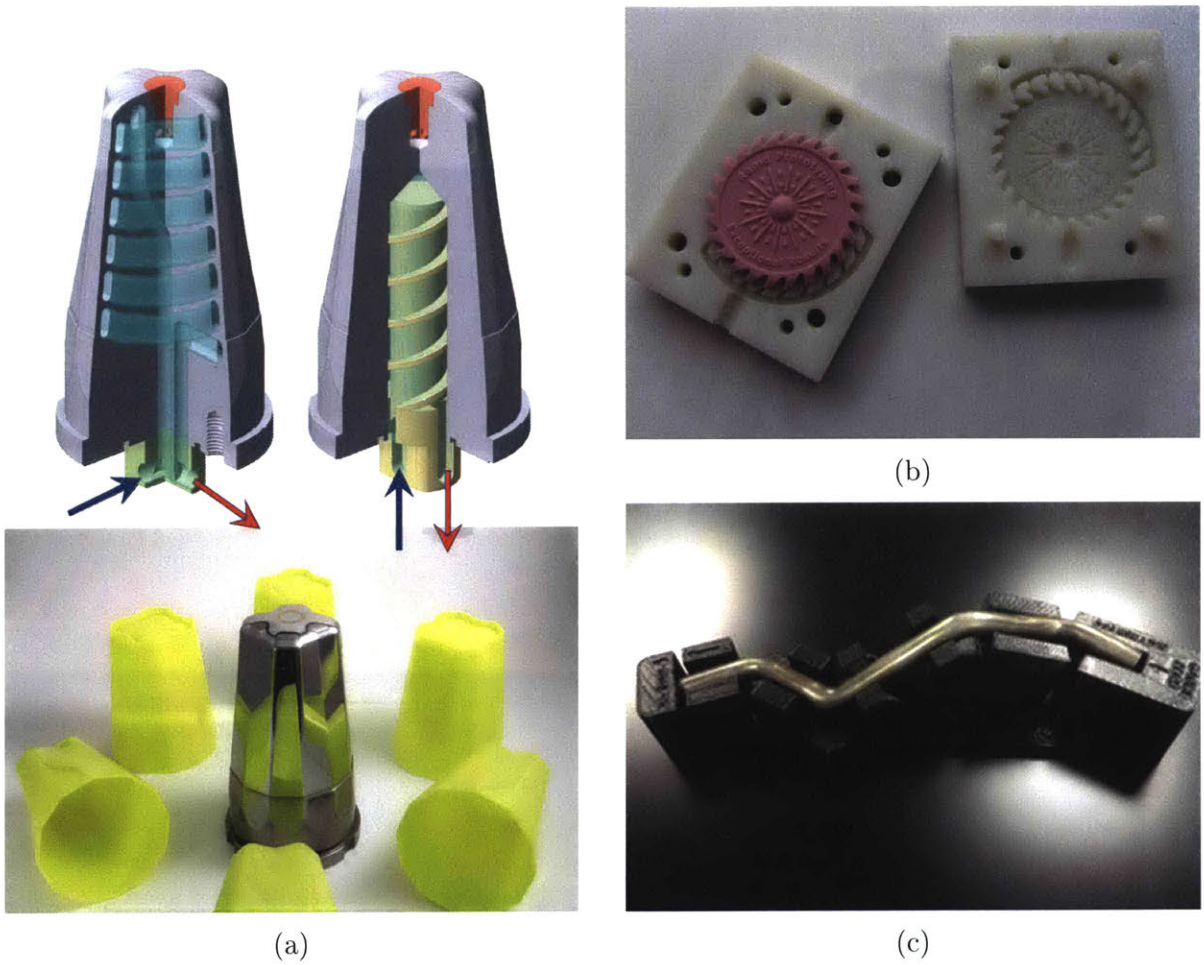

(a) (b) (c)

Figure 1-11: Examples of additively manufactured tooling including (a) and injection molding die with optimized cooling channels (left) compared to a traditionally manufacture die (right), (b) a mold printed for casting polymers, and (c) custom designed fixture for holding a bent structural tube [22][24][23].

one manufactured by thermoforming a plastic sheet over an additively manufactured mold[18].

1.2.2 Motivation

Primary manufacturing processes achieve efficiency through economies of scale that is difficult to challenge, but this efficiency is eroded by the costly, time-consuming secondary manufacturing processes, known subtractive manufacturing, required to finish a part. Additionally, as design tools evolve to provide design engineers a greater degree of freedom, and as performance requirements continuously increase, the desired

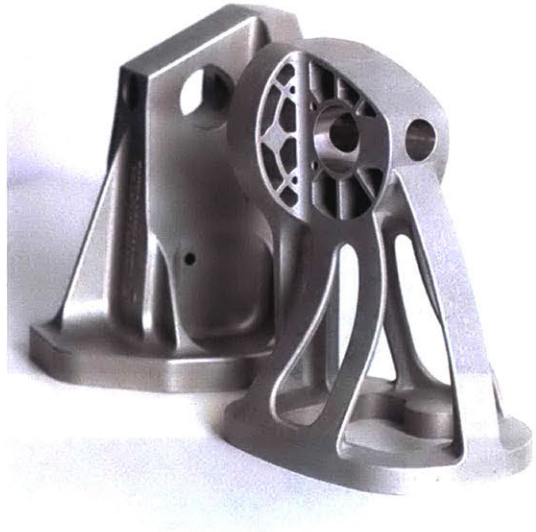

(a)

(b)

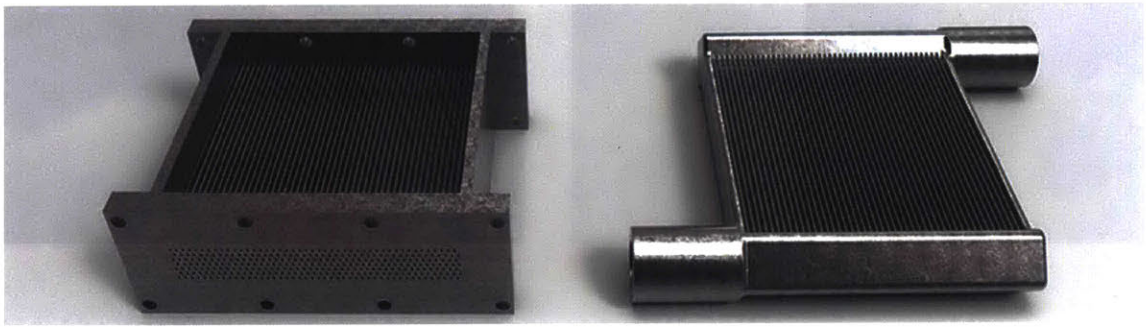

(c)

Figure 1-12: Examples of direct additively manufactured parts including (a) an aircraft bracket (front) that achieves a 7% weight reduction over its traditionally manufacture counterpart (back), (b) an integral fuel nozzle assembly for a jet engine that eliminated 17 parts, and (c) an optimized heat exchanger (right) with 20% better performance than its traditional counterpart (left) [13][27][25].

end products skyrocket in complexity. With subtractive manufacturing, material is removed from a starting billet to achieve the desired shape, dimensional tolerances, and surface finish. The challenge is that as parts increase in complexity, the amount of material removed increases, and that wasted material carries a cost. Figure 1-13 shows the drastic difference from start to finish and the material that must be removed.

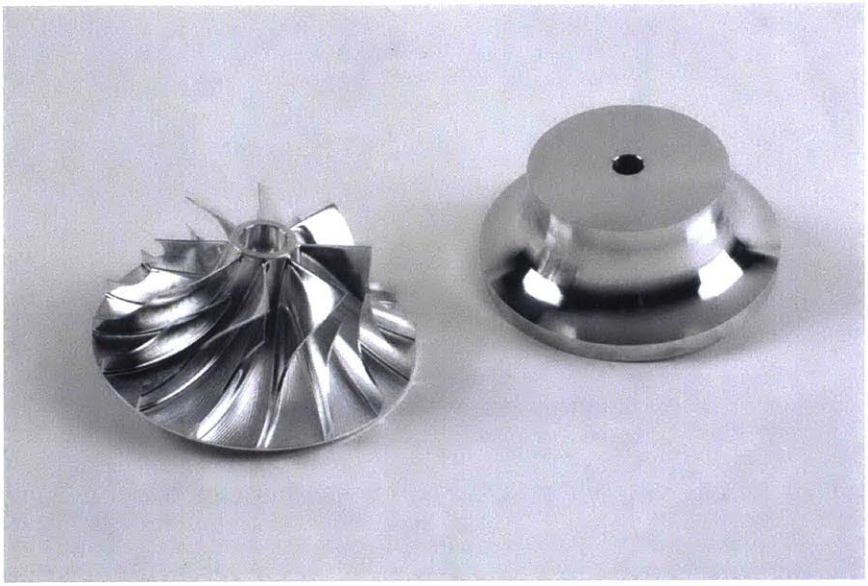

Figure 1-13: Beginning billet (right) and finished supercharger impeller (left) showing the large amount of material that must be removed when manufactured using subtractive manufacturing techniques [28].

Beyond material waste, parts with a high degree of complexity often require many equally complex fixturing systems to hold them for manufacturing. The complex fixtures incur significant manufacturing costs and labor penalties that quickly render small production runs or highly complex parts economically unfeasible. This also assumes that the desired shapes can even be produced with traditional manufacturing processes. Limited to subtractive manufacturing, design engineers are presented with a significantly limited design space as features such as internal channels may not be possible. With clever design some of these limitations can be overcome, but often require multiple parts to create the desired product which brings with it increased cost, complexity, and potential for failure. Traditional subtractive manufacturing, while advantageous in many circumstances, has significant shortcomings.

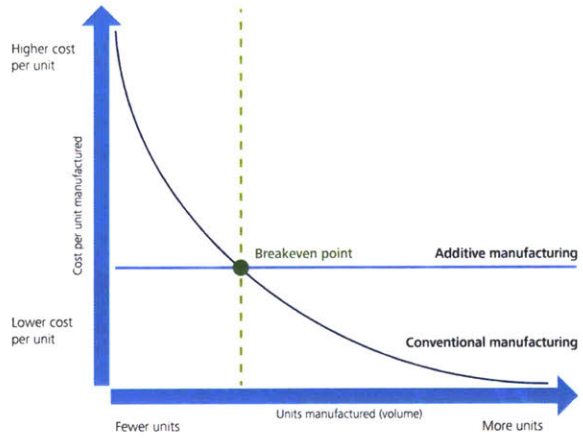

Figure 1-14: Plot of the cost per part based on the number of units manufactured [29].

Additive manufacturing opens up the design space for engineers and makes a new generation of designs possible. From a structural perspective, this new manufacturing process allows for an increase in the lightweighting of parts by creating geometries that are structurally optimized but previously unavailable because they are not manufactured with subtractive manufacturing. Not being constrained by material removal, additive manufacturing also allows for multiple parts to be integrated together, reduces the manufacturing costs and part count while increasing reliability. As discussed previously, the GE LEAP fuel nozzle is an excellent demonstration of these concepts by reducing part count and increasing reliability. Fluid systems can also benefit significantly from the freedom that additive manufacturing offers as it can create freeform channels optimized to heat transfer, fluid flow, or mixing. Beyond performance improvement, entirely new structures are possible such as lattice frameworks shown in figure 1-15. The structures have unique structural and functional properties that have been largely unexplored because they cannot be manufactured with any other process.

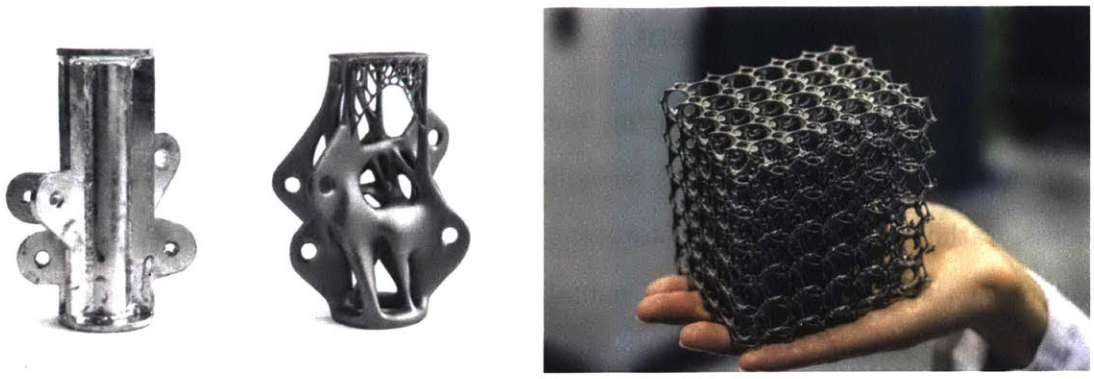

(a) (b)

Figure 1-15: Examples of non-traditional structures such as a (a) tensional integrity structure fabricated through traditional means (left) compared to a weight-optimized structure and a (b) printed metal lattice [30][31].

The new proliferation of additive manufacturing allows for a new manufacturing and supply paradigm centered on reconfigurable, just-in-time, decentralized production. In replacing traditional manufacturing processes like injection molding and casting, there is a significant reduction of tooling necessary for part production as well as a corresponding reduction of cost and labor required to maintain that tooling. Beyond replacing traditional manufacturing processes, additive manufacturing allows for agile manufacturing operations. Every job on an additive system can be different, providing the opportunity for manufactures to customize and modify parts on the fly to adapt to changing market needs. While some processes still retain an advantage in economies-of-scale, these advantages can be blended with the strengths of additive manufacturing by centrally producing core components with traditional practices and locally producing components that differ by region with decentralized additive manufacturing facilities. Outside of new product production, in logistics and maintenance, this same reconfigurability can be leveraged to reduce the warehouse storage of components necessary. By producing components on an as-needed basis, additive manufacturing has the potential to replace entire warehouses of parts.

1.2.3 Problem Statement

The interest in additive manufacturing, and the research that drives it, is increasing at an exponential rate. As industries recognize additive manufacturing as a production process, rather than a rapid prototyping tool, research institutions are beginning to increase their focus in additive manufacturing research to meet industry needs for enhanced performance, wider material selection, and verification of parts. One great indicator of this is that the Solid Freeform Fabrication Symposium, one of the leading conferences on additive manufacturing technology, has seen an explosion in the number of attendees as seen in figure 1-16. Likewise, the number of patents granted and being applied for in the additive manufacturing industry is increasing at a high rate, as are the revenues for additive manufacturing parts and services.

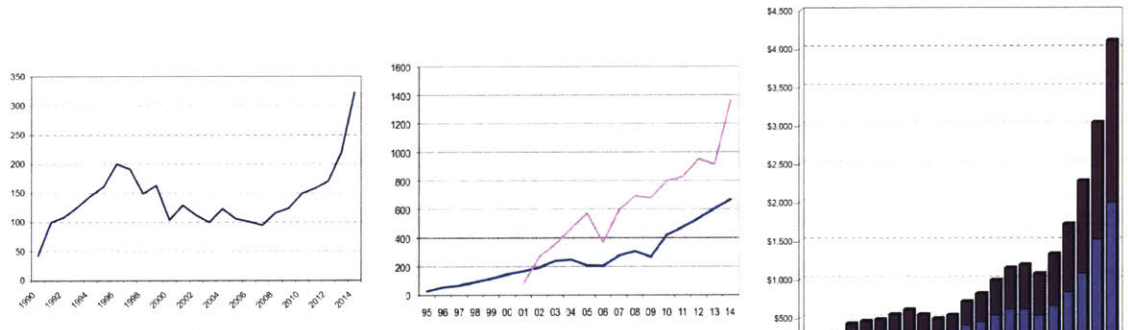

(a) (b) (c)

Figure 1-16: Rapid growth in the additive manufacturing sector as demonstrated by the (a) number of attendees at the Solid Freeform Fabrication Symposium, (b) number of patents granted (blue) and applied for (magenta), and (c) the revenue of additive manufacturing parts and services (magenta) and the machine sales (blue) in millions of dollars [18].

Despite the explosion of interest in additive manufacturing, there are significant challenges facing researchers who hope to join this rapid increase in research opportunities, beginning with the cost of entry. Great strides have been made on the availability of low-cost additive manufacturing machines, but there are some additive manufacturing processes, particularly powder bed fusion, that are only accessible through industrial-grade machines. Multiple companies produce and sell SLM

machines for commercial purposes, and many of those machines have been used for conducting research. In the area of laser-powered SLM machines, Keyence, EoS, SLM Solutions, and 3D Systems are examples of companies who market industrial-grade systems, and they range in price from $\$200,000$ to well above $\$1 million$ [18]. While many large institutions, or those with a significant research background in additive manufacturing, may be able to afford commercial machines, the cost of entry is a significant barrier for small institutions looking to enter the field.

Even with the requisite funding, another significant challenge in conducting research with commercial machines is the access they provide for control. These commercial machines were designed to operate in a manufacturing environment, as such they are not open-source/open-architecture systems which limits researchers to a minimum level of controllability that the manufacturer provides. As-purchased, these machines are designed to be "black box" systems where the end user provides the part file, and the machine takes cares of all of the rest of the operation. While there is some control over process parameters, there is a significant difference between this process tuning and the fine-grain control that would be possible with complete access to the underlying system. Manufacturers are beginning to allow for some limited control over the machines' process parameters, but that access often requires official collaborations and/or restrictive written agreements.

Despite the growth of interest and funding for SLM-oriented research, as well as the wealth of benefits to researchers in gaining access to all of a machine's parameters, the demand for an inexpensive, open-architecture SLM machine is going largely unfilled. No company currently offers an SLM machine capable of both polymer and metal fusion with full control of process parameters, let alone a system that can be purchased for less than several hundreds of thousands of dollars. There have been several attempts to venture into this space, with varying levels of success. The University of Texas at Austin has developed their own testbed for investigating high-temperature polymer selective laser melting [32]. While a custom design, it is limited to polymer materials and, short of one brief academic review paper, no information on the system's design has been released. OpenSLS and You-SLS

are two systems under active development that are open-source SLS/SLM machines [33][34]. While well documented and inexpensive to reproduce, neither system replicates the performance of commercial systems. Like the UT Austin system, both of these machines are limited to polymer build materials. Additionally, both use an XY-gantry system for directing the laser, and have more in common with traditional laser cutting systems than modern industrial SLM machines. On the commercial front, there have been a host of smaller companies looking to break into the low-end market of laser powder bed printing. Norge Systems' Ice1/Ice9 [35], Aurora Labs' S-Titanium [36], Sharebot's SnowWhite [37], and Sintratec's S1 [38] are all attempts to produce a consumer-grade SLS machine. Although these systems have more in common with their commercial brethren than the current open-source systems, such as using galvanometer mirror control systems, none of these machines have made it beyond marketing literature. While there are current efforts, both free and for-profit, towards developing an SLS/SLM system on a physically smaller and less expensive scale than current commercial machines, none of them posses the extensive operator control, wide material selection, and performance needed for research applications.

1.3 Thesis Outline and Summary

Given the current gap in powder bed printer technology, there is a clear need for an inexpensive, open-architecture system that will allow for unrestricted research in laser powder bed printing. This work seeks to address whether or not it is feasible to build an open-source/open-architecture laser powder bed fusion system leveraging commercial-off-the-shelf components to keep the cost below $50,000$.

Chapter 1 - Introduction Discusses the concepts of production environments and manufacturing processes as well as introduces the concept of additive manufacturing. The AM process is then broken down into its seven major constituents, each of which is described. The motivation for using AM and applications of that technology are then discussed to illustrate the need for additional research.

Chapter 2 - Powder Bed Fusion A discussion on the history of the selective laser melting process, the design of the machines used, and the anatomy of the parts that it produces. Also includes a brief discussion of the influence of pressure on the process.

Chapter 3 - System Construction Walks through the design and construction of a 1-dimensional linear test platform as well as a multi-station, galvanometer-steered selective laser melting platform.

Chapter 4 - System Testing Provides a description of the experimental processes used to verify the operation of the systems developed and discusses the challenges to implementing the designs.

Chapter 5 - Conclusion and Future Work Summarizes the work presented within this thesis and provides a brief discussion on the future avenues of research including a study exploring the selective laser melting process under varying atmospheric conditions.

This thesis makes the following contributions:

1. The design and construction of an open-architecture selective laser melting (SLM) 3D printer, including: galvanometer-based laser steering unit, optical positioning tower, pressurized build chamber, multi-layer powder recoating system, and safety enclosure.
2. Reconfigurable hardware control system for driving the experimental setup with expansion capabilities to integrate real-time feedback and control.
3. A modular, open-source software pipeline that converts industry-standard STL files into the control signals necessary to operate the system.
4. Extensive documentation and discussion of the system architecture and operation to allow for replication and modification, leveraging commercial-off-the-shelf (COTS) components wherever possible.

5. Experimental verification of system operation for SLM of nylon and stainless steel, via parametric experiments exploring the relationship between laser power, scan speed, and melt track geometry.

Chapter 2

Powder Bed Fusion

2.1 History of Powder Bed Fusion

Despite being a relatively young technology, additive manufacturing has a rich history. In 1979 Ross Householder created what is considered the original patent, number 4,247,508, which described a three-dimensional matrix of casting and mold materials for additively constructing castings. Householder's idea, seen in figure 2-1, was to selectively place either sand or a concrete mixture in a matrix and then harden the concrete with water. While this may not sound much like modern additive manufacturing techniques, this patent represents the first general instance of controllably placing different materials to create objects. Householder had thought of using a laser or other directed energy source to use the technique with other materials, but was never able to build any working devices [39].

The first functional selective laser sintering system can be traced back to an aspiring inventor named Carl Deckard. Starting work in 1984 as graduate student at the University of Texas at Austin, Carl Deckard worked under then assistant professor Dr. Joe Beaman. Having explored the concept of selective laser sintering manufacturing in his master's thesis in 1986, he developed the first prototype SLS system, dubbed Betsy, seen in figure 2-2. Demonstrated in 1987, Betsy looks nothing like modern incarnations - built around a Commodore 64 computer, 100 W Nd:YAG laser, and a fast scanning mirror system - but possesses all of the same key systems.

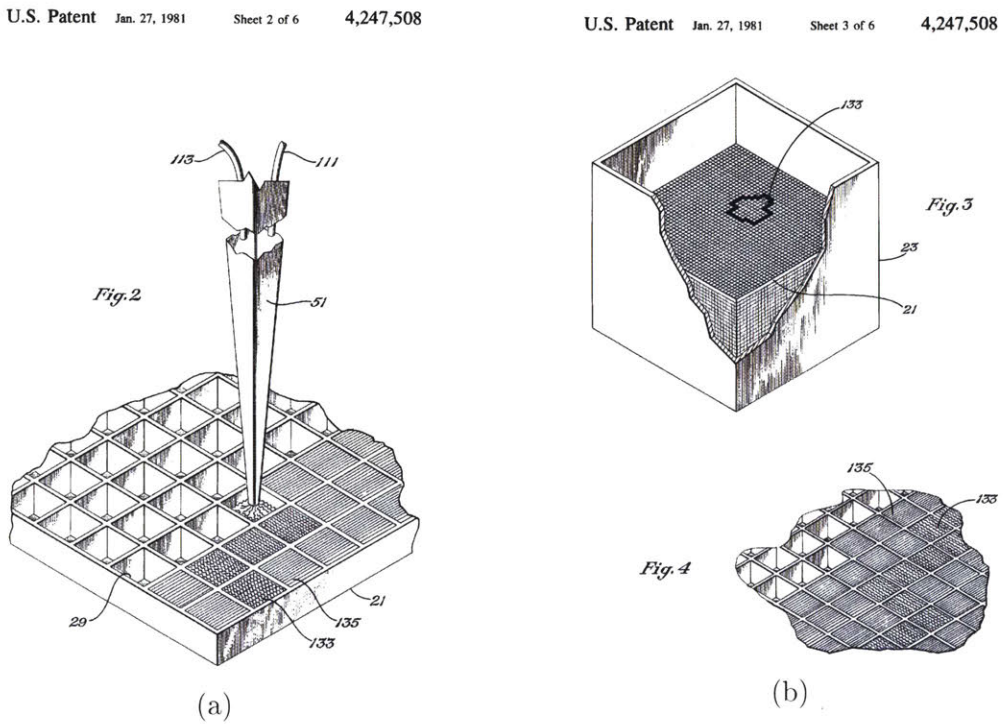

(a) (b)

Figure 2-1: Pictures from Householder's original patent showing the concept of selectively laying down concrete and sand [40].

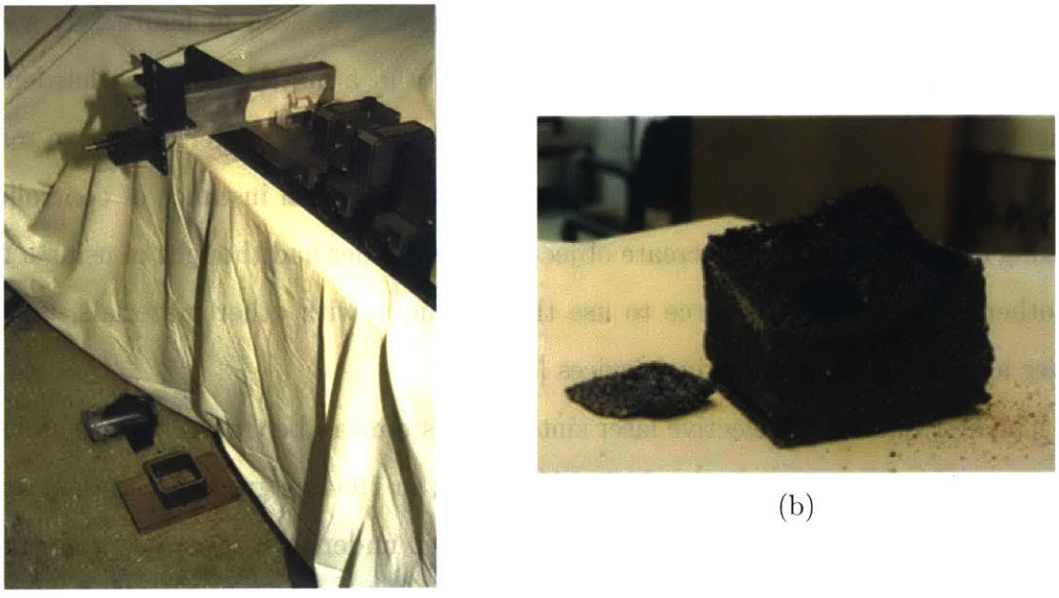

(a) (b)

Figure 2-2: The machine that started selective laser sintering, (a) Betsy and (b) a part Deckard fabricated on Betsy [39].

Deckard continued his work at UT Austin in pursuit of a PhD, but also worked to commercialize his inventions. Through a company originally called Nova Automation and later renamed DTM Corp., Deckard filed for several patents, including a heated powder handling system and a counter-rotating roller recoater. Using Deckard's and Householder's patents (licensed from Householder), and having secured $6 million from Goodrich Corp., a chemical and aerospace manufacturing giant, DTM Inc. unveiled the first commercially built SLS/SLM machine in 1989. While only four machines were built, two of which can be seen in figure 2-3, and none were sold commercially, the DTM machines were the first SLS/SLM systems to be produced outside of academia [39].

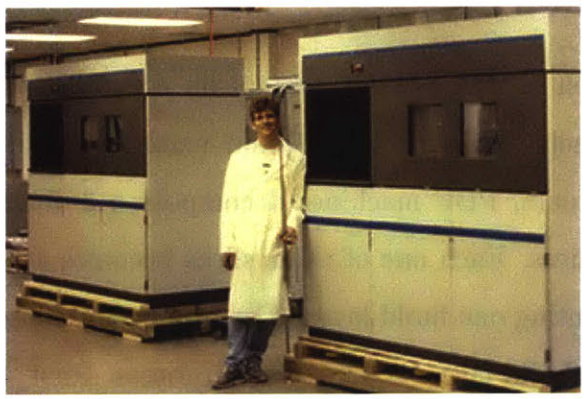

Figure 2-3: Two of the four 125s that DTM produced in 1990 [39].

While Deckard and DTM achieved many significant firsts in plastic SLS technology, others quickly began to expand upon the technology. Manriquez-Frayre and Bourel, also located at the University of Texas at Austin, were the first to demonstrate selective laser sintering of binary metallica media, expanding beyond the plastic materials that Decker had used [41]. While DTM Inc. was the first commercial entity to bring an SLS system to market, they were not the first to bring a selective laser melting (SLM) to market. In 1995, Electro Optical Systems (EOS) Inc. brought to market the EOSINT M 250, seen below in figure 2-4, the first commercial SLM system.

Figure 2-4: An original EOS INT M250, the first selective laser melting machine to meet the commercial market [42].

2.2 The Powder Bed Fusion Process

The powder bed fusion (PBF) process centers on controlling an energy source to selectively sinter or melt fine particles of build material to form a solid part. To construct a complete part, PBF machines decompose a 3-dimensional body into a set of 2-dimensional slices. Each one of these slices becomes a raster pattern for the energy source, representing one build layer. The process for constructing a single one of those 2-dimensional build layers is a three step process. First, the recoating system of the machine lays down a thin layer of the powdered build material. Second, the energy source selectively fuses portions of the build surface, creating the 2-dimensional slice of the 3-dimensional object. Third, the build platform is lowered down to allow for a new layer of material to be deposited. From there, the process repeats itself until all of the 2-dimensional slices have been stacked on top of each other to create the three dimensional part. A depiction of this process and of the constituent elements of the machine can be seen in figure 2-5.

The laser melting of the powdered build material is a complex process that is highly sensitive to the material properties, build patterns, and process parameters. The bed of build material looks, on a small scale, like a random stacking of spheres. Due to the uncompressed nature of the build material, in order to not damage the underlying portions, the density is only 40% to 60% [44]. As the laser radiation strikes

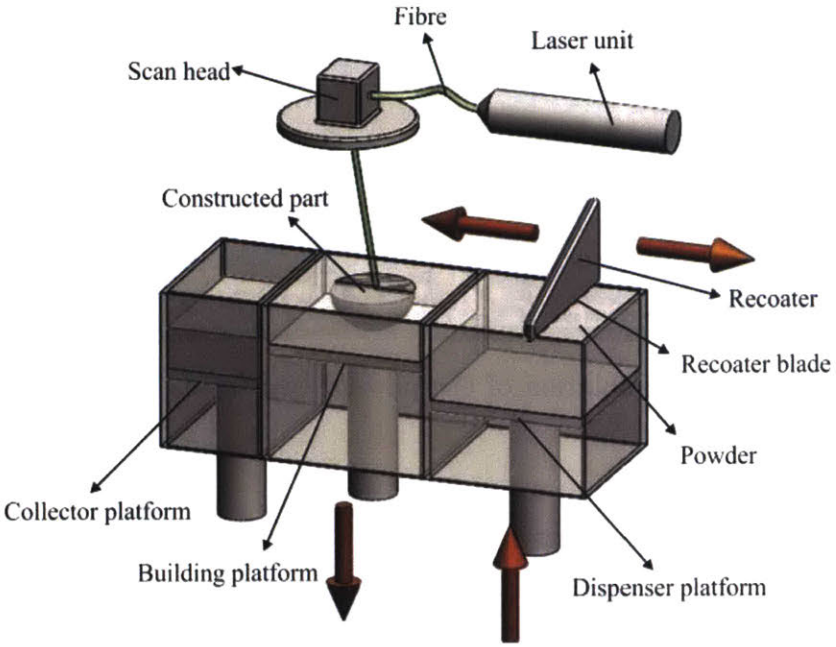

Figure 2-5: A simplified model of a powder bed fusion system [43].

the build material, it is absorbed not only by the top layer of particles, but also some of the lower particles as laser radiation travels through the pores. Although much of the incident radiation is absorbed by the particles themselves, a significant portion is reflected. This reflected light is then absorbed or reflected by other particles, creating quasi-volumetric heating. As the particles melt, viscous flow due to surface tension consolidates them together into a melt pool. Once the melt pool is formed, the thermal dynamics change as the energy flow is now into the melt pool, which transfers it to the surrounding material through conduction, radiation, and intra-pore convection. When the melt pool is formed, several complex fluid dynamic elements also influence the formation and movement of the melt pool such as surface tension, Marangoni convection, and recoil pressure. A depiction of this process can be seen below in figure 2-6

Due to this complex interaction, many parameters play a significant role in the production of a part. Figure 2-7 shows a breakdown of the three main categories of parameters: process, machine, and material. Given the scope of this work, the process and machine parameters are key in that they can be controlled through either design of the machine, or are controlled by the machine.

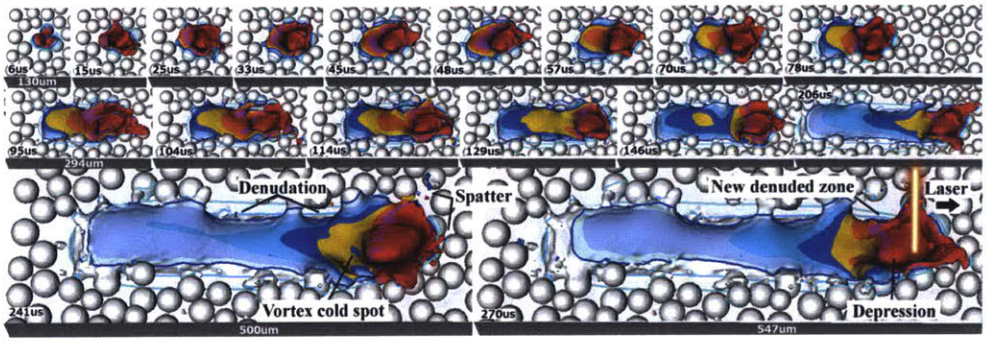

Figure 2-6: Powder-level simulation of the powder bed fusion process depicting the formation of the melt pool [45].

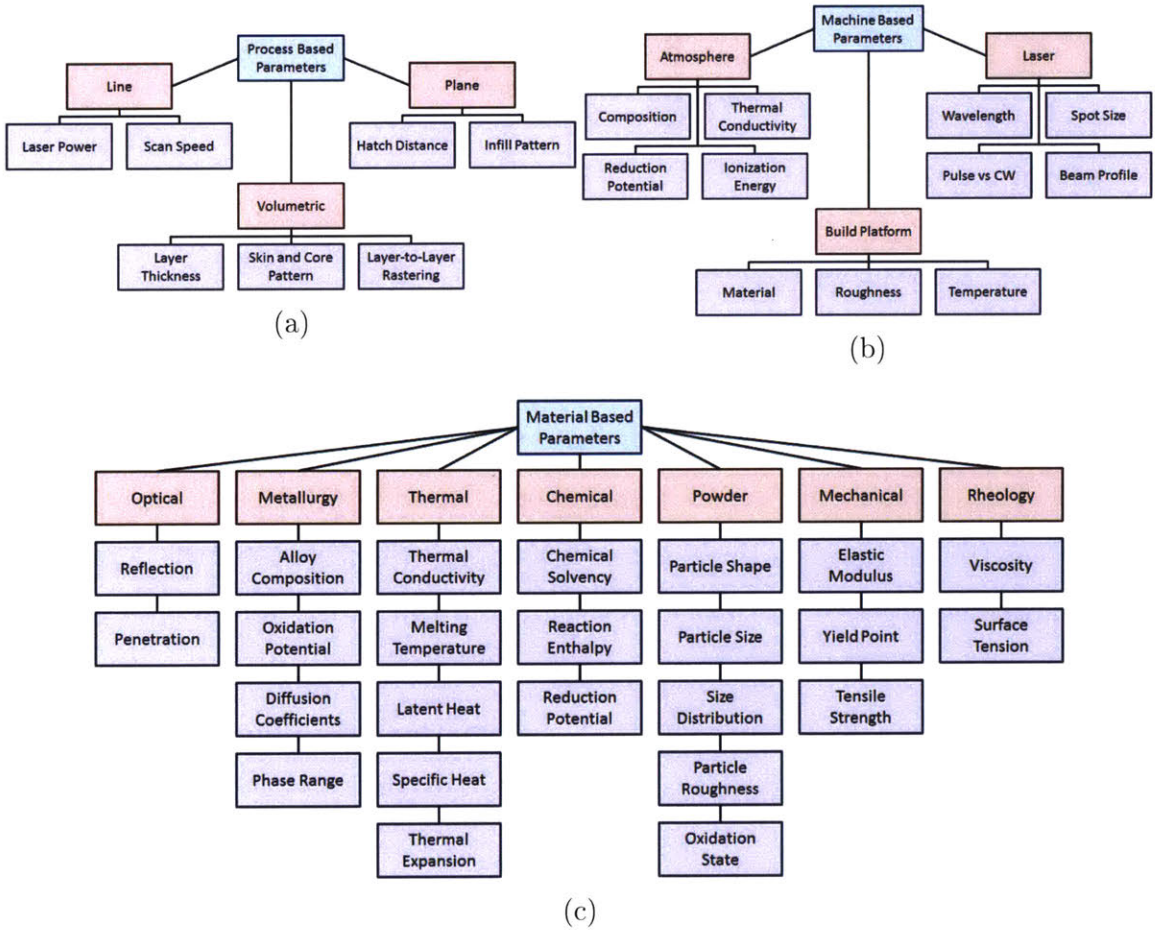

Figure 2-7: Breakdown of the various parameters influencing the powder bed fusion process including (a) process parameters, (b) machine parameters, and (c) material parameters [46].

One resultant quality of the input parameters and machine design is the final density of the part. An important distinction based on the density of the final part is whether a system is producing low density or high density parts. Low density parts

are those where the powdered build material is not completely melted together to form a build object, but is instead only partially melted or sintered. For some applications, a sintered part is sufficient in terms of mechanical properties. When sintered parts are not capable of meeting the performance requirements, parts can be infused with a secondary metal, such as bronze, or some other bonding agent to provide greater mechanical properties. This is an extra and distinct processing step that goes beyond the normal PBF work flow. In contrast, newer, higher performance machines are capable of fully melting the build material, generating parts with densities greater than 98%.

2.3 The Machines and The Parts They Make

2.3.1 Anatomy of a Powder Bed Fusion Machine

Despite the complexity of the physics involved in the powder bed fusion process, the machines can be decomposed into a simple set of common components. From Betsy to the most sophisticated machines available today, there are four components used in a powder bed fusion system: a build stage, powdered build material, recoating system, and steerable energy source. In more complex systems, the machines may also be fitted with environmental control and/or sensing and feedback control. A simplified model of an SLM machine can be seen in figure 2-8. The build platform is a precise vertical motion stage that positions the build plate, on top of which the part is constructed. This is tightly coupled to the recoater which is used to distribute a thin, even coating of the powdered build material over the build platform creating the build layers. A steerable energy source is then used to selectively melt the build material in each successive layer to create the desired part.

The machine performs three sequential operations to generate each layer of the desired part. The process of building a part begins with the recoating system spreading a thin, typically 20 to 100 µm, layer of the powdered build material across the build platform. The steerable energy system then melts select parts of the newly coated

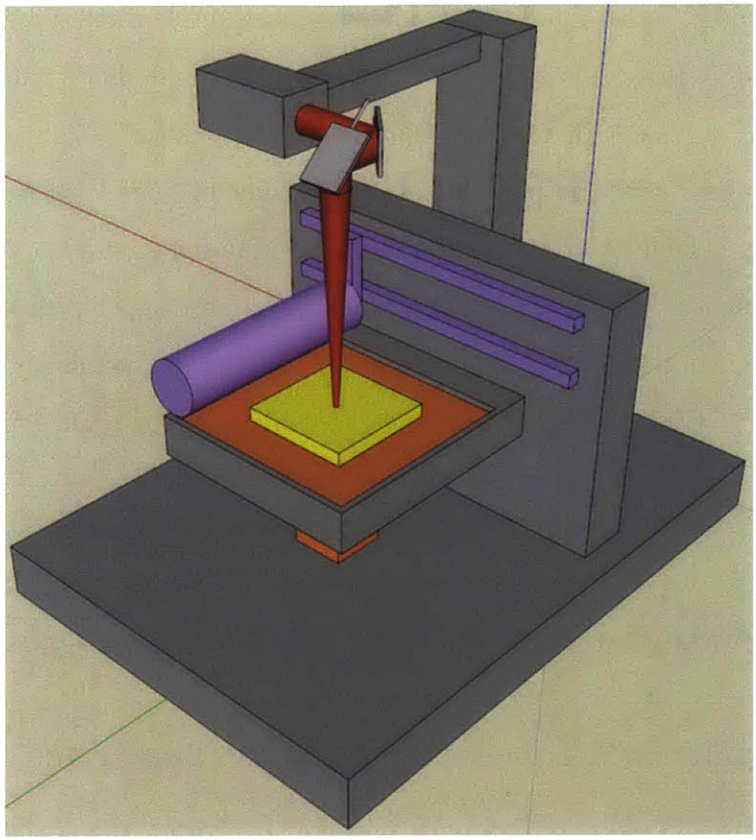

Figure 2-8: Simplified SLS/SLM system showing laser and positioner (gray), recoater (purple), vertical stage (orange), and powderbed and workpiece (yellow).

layer of powder by directing the energy at the desired location(s). Once the selective melting is complete, the build platform lowers by the layer height of the system, and the recoater lays down a new layer of material. This process repeats until the entire part has been built.

Energy Source

In powder bed fusion, a directed energy beam is responsible for sintering or fusing the build material to generate the final, fused part. There are two primary means of conveying the energy required to sinter or fuse the material: photons and electrons. The photon-based systems, i.e. laser-driven systems, make up the majority of the SLS/SLM market. The single alternative to this process is produced by Arcam AB, and uses a controlled electron beam, similar to a scanning electron microscope, in place of a laser.

Laser Systems In photon-based systems, the energy required is generated by a high-power laser module. There are a wide variety of lasers that can be used, from semiconductor lasers to fiber lasers, and each operates on a different principle. The type of laser module selected for a machine depends, among many factors, on the desired wavelength of light. The selection of wavelength itself depends on a variety of requirements as well, but two of the primary influences are the spectral absorbance of the working material and the availability of high-power modules in the desired wavelength. Figure 2-9 shows the spectral absorbance of nylon 6 and Ti6Al4V, two common build materials. Of the available laser technologies, the two most common are fiber lasers and semiconductor lasers.

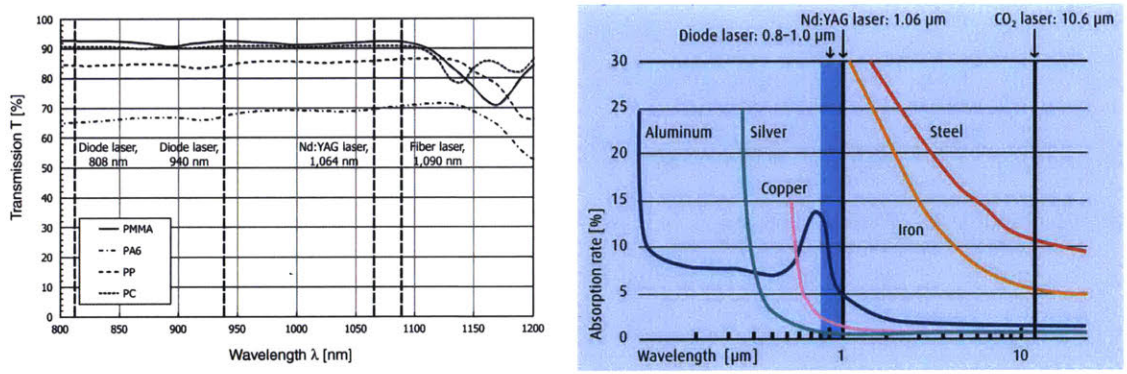

(a) (b)

Figure 2-9: Material absorbtion graphs for (a) common plastics including PA6, PC, PMMA and PP as well as (b) for common metals inlcuding aluminum, copper, and steel [47][48].

One common laser type in commercial systems is a fiber (or fibre) laser. Fiber lasers are a class of diode-pumped solid-state lasers (DPSSLs) that use an optical fiber doped with rare-earth elements as the active gain medium. A diagram of this construction can be seen in figure 2-10. Doping elements such as erbium, ytterbium, and neodymium are common, and that is where the common term Nd:YAG comes from - neodymium-doped yttrium aluminum garnet. The energy is pumped into the fiber using one or more fiber-coupled laser diodes, passes through either a dichroic mirror or a fiber Bragg grating, and energizes the lasing medium within the doped section. The resulting energy escapes the other end of the fiber through another

dichroic mirror or fiber Bragg grating, and is generally coupled into a fiber for directing the energy. One characteristic of these lasers is that they can operate in either a continuous wave (CW), where they continuously emit laser energy, or pulsed emission mode, where laser energy is emitted in intermittent bursts.

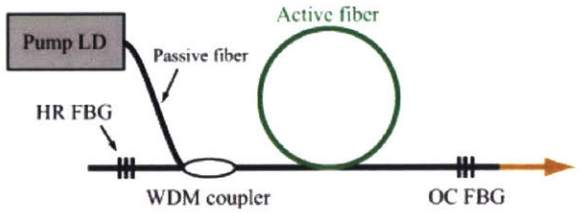

Figure 2-10: Diagram of a diode-pumped solid-state fiber laser showing the pump laser diodes (LD), wavelength division multiplexer (WDM), high reflectivity (HR) and output coupling (OC) fiber Bragg gratings (FBG), and the active fiber [49].

Another common optical topology used to generate the laser energy is a semiconductor laser. The gain for generating the output is created by pushing current across a semiconductor junction, often a p-n or p-i-n junction. While fiber lasers make use of semiconductor laser diodes to pump the fiber gain medium, semiconductor-based fiber-coupled lasers do not use the fiber as a gain medium, but are instead using the laser diodes as the output source directly. One important note is that a laser diode can only generate a few hundred milliwatts operating in a single transverse mode, so multiple diodes are bridged together and operate in multiple transverse modes to generate larger amounts of power. The side effect of this is that the system requires a large-diameter, multi mode fiber core and suffers from greater divergence **spi**

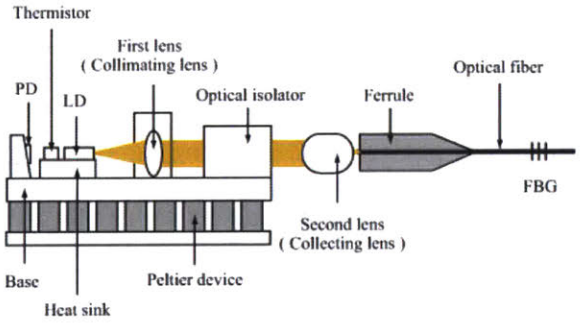

Figure 2-11: Diagram of a fiber-coupled laser diode module showing the laser diode (LD), optical elements, and output fiber Bragg grating (FBG) within the output fiber [49].

In comparing fiber lasers with semiconductor lasers, several distinctions can be drawn. DPSSLs possess higher beam quality due to the fiber active medium having waveguide-like properties that can reduce thermo-optical distortion. Additionally, DPSSLs can also be built to generate high output powers as the active medium can be made longer to generate more power, even in the 10 of kilowatts. Lastly, in addition to being compact and reliable, these lasers generate a single-mode beam that can be coupled into a small-core fiber allowing for small focal size at the objective. Semiconductor lasers are not without their own advantages though. Laser diode systems are cheaper and more efficient as the DPSSL crystals are not 100% efficient. Additionally, fiber lasers are highly temperature sensitive and suffer from beam instability, such as mode hopping and power fluctuations, if operated outside of their stability range, while laser diodes are much more thermally tolerant. Lastly, the output of laser diodes can be easily modulated.

Electron Beam Systems In electron beam melting (EBM), the process is nearly identical to the laser-based process, but the laser power source is replaced with an electron beam source. Current EBM machines use a scaled-up version of a scanning electron microscope (SEM): a filament generates a beam of electrons that is then driven through a set of lenses for focusing and deflecting the beam to the desired pattern. One important caveat of using EBM compared to laser-based systems is that the system must be under vacuum to eliminate gas molecules which would rapidly spread and attenuate the electron beam. The most common electron source is a thermionic gun which creates a stream of electrons from a heated filament, often tungsten, via thermionic emission

Design Considerations In designing a powder bed fusion machine, selecting an energy source may be largely dictated by the availability of the different energy sources. Building a system around an electron energy source may be challenging from the perspective of acquiring a high-power electron source. One potential candidate is an off-the-shelf electron beam welding system, which, as the name implies, welds mate-

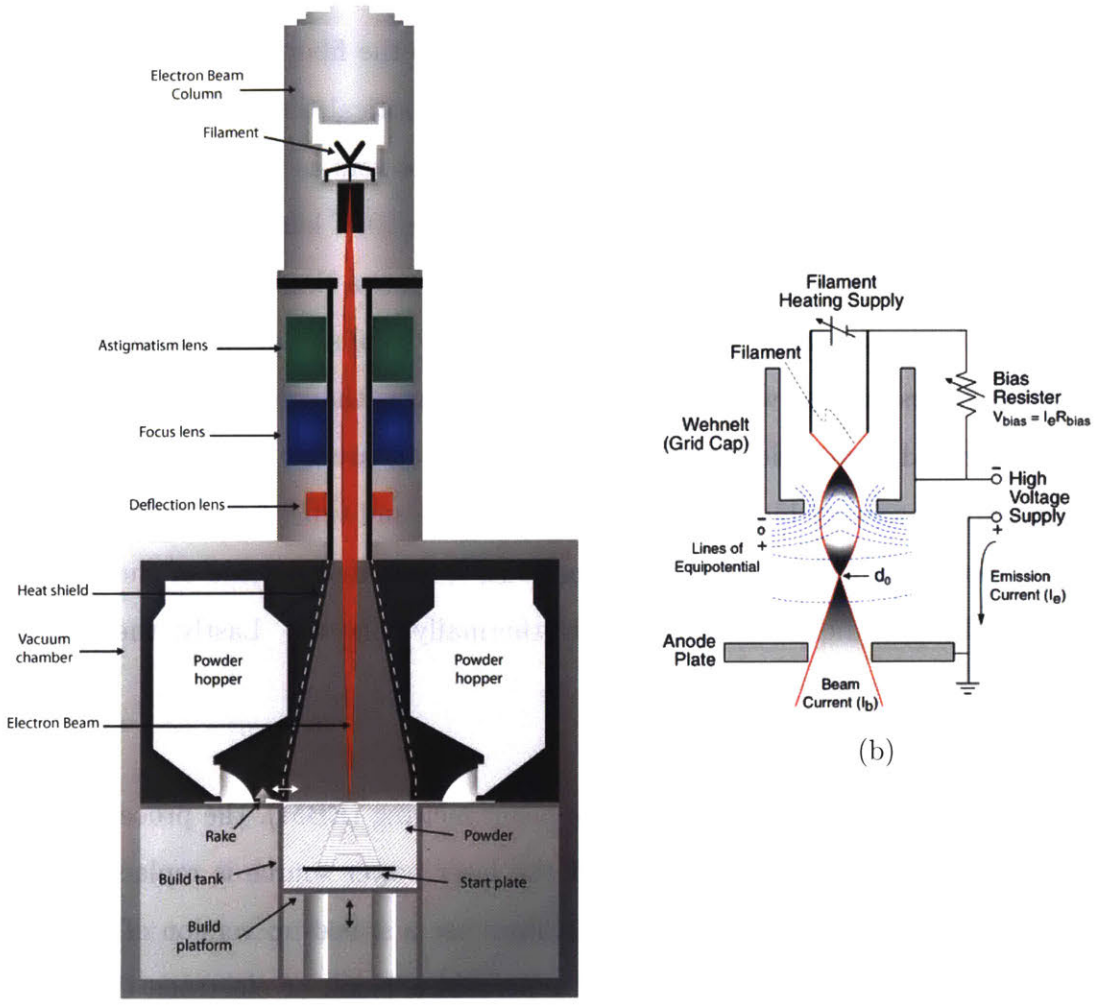

Figure 2-12: Anatomy of an electron beam melting powder bed fusion machine showing (a) the overall electron beam source construction including the filament and the various lenses, and (b) the construction of a thermionic gun, one method of generating electrons [50][51].

rials together with an electron beam. These systems are commercially available and are nearly identical to commercial EBM systems used in additive manufacturing save for the fact that the build chamber is designed to house parts to be welded together instead of having a powder build platform.

In comparison to designing a system around an electron gun, constructing a system with a laser energy source provides a wide range of options. While high-power electron beam sources may not be prevalent, high-power laser sources are readily available

due to their widespread commercial and scientific applications. In selecting a laser, aspects to consider include the wavelength of the laser, mode of operation (continuous wave versus pulsed), output power, and focused spot size. These design requirements will likely dictate the type of lasers to choose from due to the qualities of each laser generation topology, as discussed above. Cost will also play a significant significant factor as the laser is often the most expensive component in a laser-driven system.

Beam Steering System

The beam steering system is responsible for guiding the energy generated by the energy source to the appropriate spot on the build platform. Given the differences between laser and electron beam systems, the beam steering systems are widely different from a mechanical aspect, but correlated from a functional perspective.

Laser Beam Steering System In laser based systems, the beam steering system is responsible for three primary tasks: beam conditioning, beam directing, and beam focusing. The first step in coupling the beam into the system is to condition the beam output. Conditioning the input beam consists of manipulating the beam profile coupled into the beam steering system into a the form that is needed. For example, in fiber-coupled lasers, the requirement is to convert the diverging beam coming out of the end of the fiber into the desired beam shape, often a collimated beam which can be done with the aptly named collimator shown in figure 2-13, so that the beam can be sent through the rest of the optical pipeline.

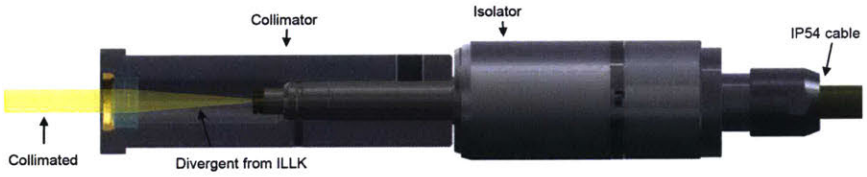

Figure 2-13: Diagram of a collimator produced by SPI Lasers to convert the diverging beam exiting their fiber laser fiber into a collimated beam [52].

Next, the system must control the trajectory of the beam such that it lands on the desired portion of the build platform. There are a wide variety of beam steering

systems, but most are a combination of linear displacement of mirrors and rotational displacement of mirrors. An example of a purely linear system is an XY-gantry system common on large-bed laser cutters where the laser objective is translated linearly along two axes to position the beam. In contrast, an example of a purely rotational system is a dual-axis galvanometer, or galvo for short, seen on laser engraving machines. A 2D galvo combines mirrors mounted on two orthogonal rotation axes to allow the beam to be rastered over a 2-dimensional region.

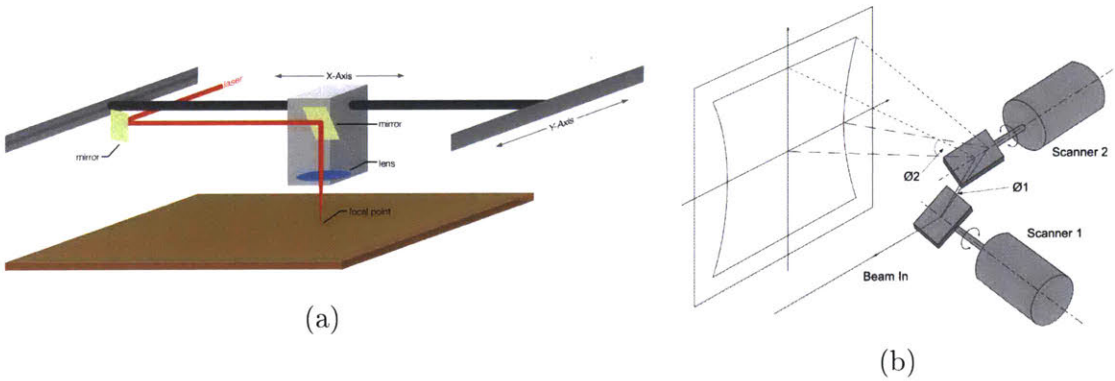

(a) (b)

Figure 2-14: Simplified diagrams of (a) a linear-linear laser positioning system like those found in laser cutters as well as (b) a rotation-rotation laser positioning system like those found in most laser PBF machines [53][54].

The last function of the beam steering system is to appropriately focus the laser beam to achieve the desired spot size. The focusing method depends largely on the mechanism that is used to steer the laser beam. For the common 2D galvo, the simplest solution is to use an F-theta lens, which is actually the combination of three lenses, to focus the beam onto a flat working plane. This lens derives its name from the equation that relates the location of the spot to the mirror angle: $x = L_{focus} \times \theta_{mirror}$. While the F-theta lens eliminates the non-linear relationship of the mirror angle to the beam position and creates a flat focal plane, it does come with the drawback in that the entire optical head must be moved to adjust the focused spot size. In more advanced systems, the focusing is done dynamically by affixing a focusing lens to a linear sled and rapidly positioning the lens to control the focal length of the beam before it enters the beam steering system. So called dynamic focus systems have the ability to focus over a much wider range and allow for variable spot size.

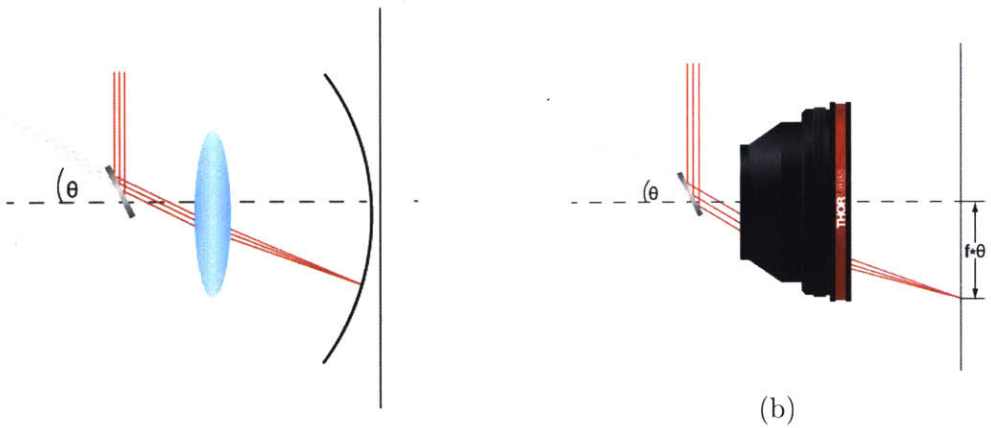

(a) (b)

Figure 2-15: Demonstration of (a) the non-flat focal plane created by a standard spherical lens, and (b) the focal plane created by an F-Theta lens [55].

Electron Beam Steering System In EBM systems, all focus and direction control occurs in the magnetic control coils. In these systems, the beam passes through three lenses, a depiction of which can be above in figure 2-12. The first lens is the astigmatism lens, also known as the stigmator. The purpose of the stigmator is to correct for astigmatism, or out-of-round, profile of the beam exiting from the electron source. Following the astigmatism lens, the beam passes through the one or more focus lenses, also referred to as condenser lenses. As the name implies, the focus lenses control the focal distance of the beam, converting the collimated beam into a converging one. The last set of magnetic lenses the beam passes through is a set of deflection lenses. The deflection lenses deflects or bends the beam off of the center axis, directing it to a specific area on build platform.

Design Considerations Design considerations for selecting a laser steering system largely center on the desired beam scan speed and positioning accuracy. The laser wavelength and means of transferring the laser energy may also play into what components can be selected due to absorption or damage thresholds. The desired scan speed will dictate the choice between two rotational mirros, one rational and one translational mirror, two translation mirrors, and other more complex systems. The most widely available systems that can meet the $1\,\frac{\mathrm{m}}{\mathrm{s}}$ speed required by powder

bed fusion are dual-axis galvanometer mirror heads. These systems are widely used in a variety of commercial applications such as laser engraving and laser cutting, as well as scientific applications, such as optical coherence tomography. These systems can even be purchased with integrated controllers that run industry-standard G-code [56].

Another design consideration is the means by which the laser beam will be focused. In most laser marking and cutting applications, the object remains at a fixed distance from the objective and the marking region is approximately planar. In these situations, an F-theta lens meets all of the focusing requirements of the system in a compact, single-part solution. However, if varying the spot size of the laser is desired, or if the work plane is non-planar, a dynamic focusing system is required to change the focal length of the laser on the fly. In selecting a means of focusing a laser, the ability to dynamically change the focal length must be weighed against the significant increase in cost and system complexity.

Build Platform

The build system is the structure that supports the part as it is built and lowers it for each layer. The build platform is constructed of four primary elements: the build chamber, the build plate, the support structure, and the vertical stage. These are assembled together with the build platform sitting atop the support structure that interfaces it to the vertical stage, and all of the components are sleeved inside the build chamber. The simplest component is the build chamber which is an enclosure that encompasses all of the components of the build system and contains the build powder within the build volume.

The build plate is a section of material used to serve as a bottom floor for the build chamber and often as an anchoring point for the part being made. The build plate is often as simple as a plate of material, potentially the same as the build material, that is bolted to the support structure. Due to the rapid heating and cooling of metal parts, and the associated rapid thermal expansion, the parts must be anchored to the build platform to prevent them from warping. One distinction between plastic and

metallic systems is that plastics do not undergo the same level of stress and warping as their metal counterparts, a comparison of these two setups can be seen in figure 2-16. Due to the lower thermal movement, plastic parts do not have to be anchored to the build plate. Instead, they can be packed and arranged to maximize part density in the build volume.

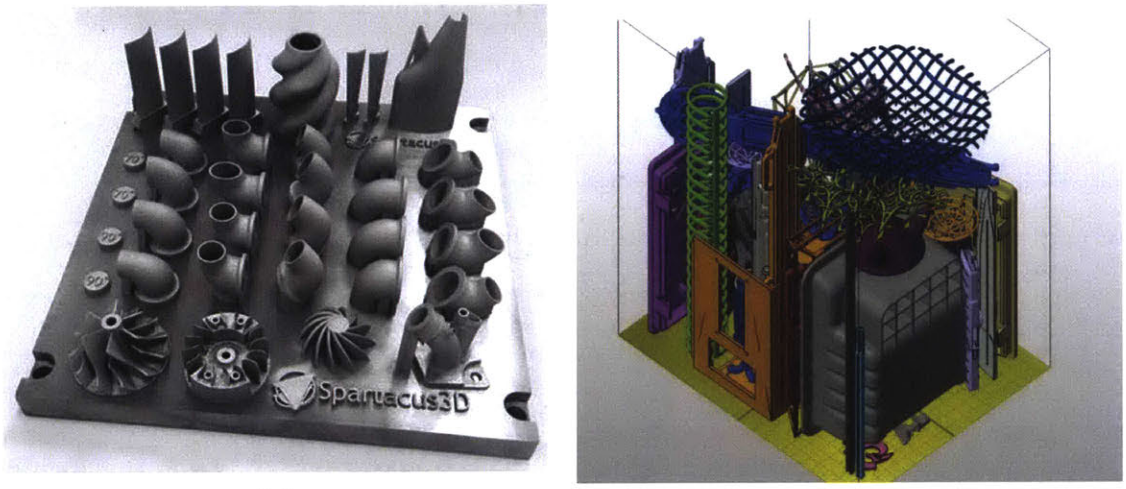

(a) (b)

Figure 2-16: Parts laid out on their build platform in (a) metal and (b) plastic powder bed fusion demonstrating how plastic parts do not need to be anchored and can therefore be stack to maximize space usage [57][58].

The support structure and vertical stage are used to control the position of the build plate within the build volume. The support structure itself is the system that links the build plate to the vertical stage, and can take many different forms depending on how the vertical stage is designed. While this may be a simple mechanical linkage, it can also serve other functions such as heating the build platform.

The vertical stage is a linear motion stage responsible for raising and lowering the build plate as the part is built. This stage can be broken into three main components: the linear guidance mechanism, feedback sensor, and drive mechanism. The linear guidance mechanism provides the required mechanical constraint to ensure the stage only moves in the appropriate direction. Some of the most common linear bearings consists of a combination of ball-bearing or sleeve-bearing carriages with either round rails or profile rails. Other technologies, such as v-groove bearings or air bearings,

could function in the required capacity, but complexity or precision requirements may rule them out. For feedback, the stage can be fitted with either a linear encoder that reads the position of the stage along its travel, or an encoder on the drive motor to measure the movement of the motor. Due to the large temperature changes the system is subjected to, optical encoders coupled with glass scales are popular. In order to move the build platform, the stage must have a means of converting electrical energy into mechanical motion. In building linear motion stages, there are a wide variety of drive mechanisms including a leadscrew or ball-screw, belt-drive system, linear magnetic motor, or voicecoil motor. Ball-screws have become popular for their combination of cost, accuracy, and durability. Due to the hostile environment in which the stage is located, particularly if the system employs a heated build chamber, belt-drives are challenging to implement. So too are linear magnetic motors and voicecoil actuators due to the constant energy consumption they require when holding a load in the vertical direction, and the changing load which makes proper counterbalancing not possible.

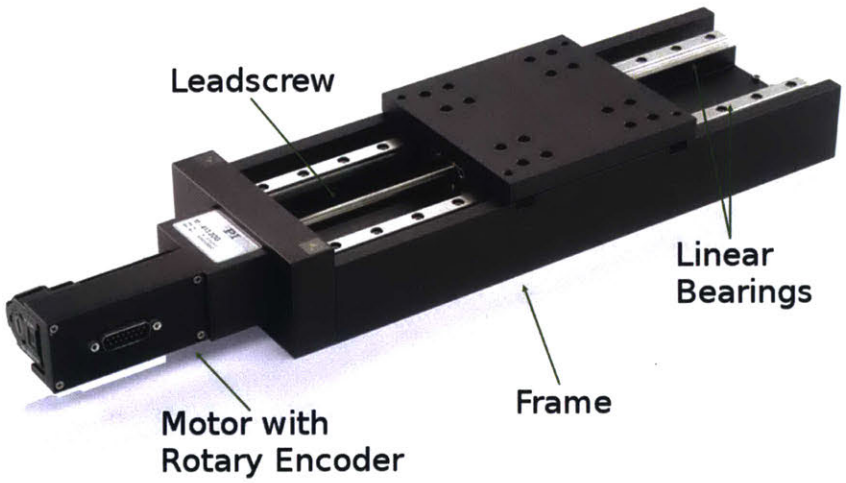

Figure 2-17: Examples linear stage showing the primary components [59].

The primary design consideration for the build system centers on the desired shape and volume of the build chamber. The size of this chamber and the space constraints of the system will dictate the choice between selecting an off-the-shelf linear actuator and a custom design system. The next key performance point is the

desired layer thickness and accuracy as these relate to the linear stage. The size and weight of the build volume combined with the desired motion accuracy will control which linear motion design choice are available. The build plate possesses its own design considerations such as what it is made of and how it is connected to the support structure. Additionally, as discussed in section 2.3.1, heating the build platform and build chamber can play a significant role in the quality of the parts produced.

Powder Handling and Recoating

In all forms of powder bed fusion machines there is a mechanism for storing, feeding, and applying the powdered build material to the build area. Starting with the powder storage, there must be some form of container within the system that contains the powdered build material during the build process. Two approaches are most often used for storing the powder: a powder feed chamber, and a powder feed hopper. Representations of both systems can be seen in figure 2-18.

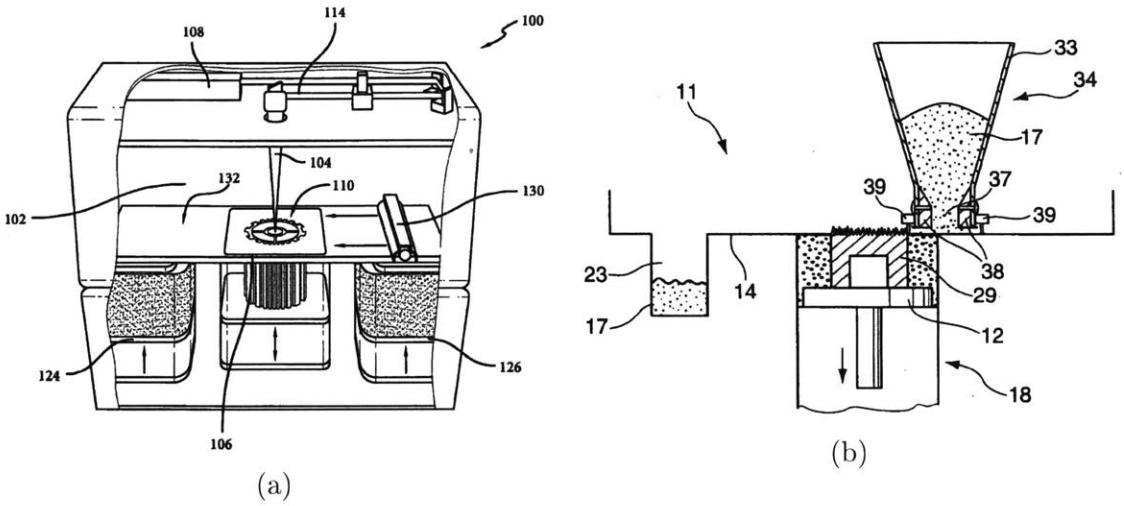

Figure 2-18: Examples of powdering being fed using (a) a powder feed chamber next to the build platform as well as (b) a powder feed hopper integrated into the recoater [60][61].

Common on many older designs, and where plenty of space is available, the powder feed chamber consists of a secondary build chamber located next to the actual build chamber, but full of powder. As the powder is needed, the piston rises in the powder chamber, bringing new build material above the surface of the chamber where it is

swept across by the recoating blade onto the build surface. Often there is a third chamber located past the build chamber that the excess powder is swept into. This approach has the advantage of requiring minimal space above the build surface as the only item that must fit is the recoater. It does come at the cost of requiring a significant amount of space below the build surface, essentially three times the actual build volume.

A different approach is to meld the recoater and powder storage together to form a moving hopper. In the powder feed hopper, as the name implies, the recoating assembly is expanded to incorporate a powder hopper next to or between the recoating blades. As the system moves across the lowered build platform, material can flow out of the hopper to create the next build layer. This has the advantage that the elements are stacked vertically so the machine can be produced with a smaller footprint and does not require any additional actuation as the powder flows by gravity. It does have the side effect of bringing more complexity to the recoater design as the entire hopper must now move.

Integral to the process of transferring the powder from the storage space to the build volume is applying it in a thin, even, consistent layer. The recoating process plays a critical role in the final qualities of a part and can both be a tool for the designer and a significant obstacle to creating good parts, figure 2-19 shows a few example designs. From the positive perspective, controlled well the layer thickness can be adjusted to control the microstructure of the parts produced [62]. However, if the layer becomes too thick, or inconsistent across the build surface, this can lead to high surface roughness on the finished part as well as porosity, lower density, and reduced mechanical strength [63][64].

From a functional perspective, the accuracy and uniformity with which the deposited layer is laid comes down to the design of the recoating system. In achieving this accuracy, a significant design constraint for the recoater is the potential for a part strike. In fusing layers, it is possible to create a feature that may protrude above the new build height, which means that the recoater will strike that feature during the recoating process. With this constraint in mind, there are a wide variety of recoater

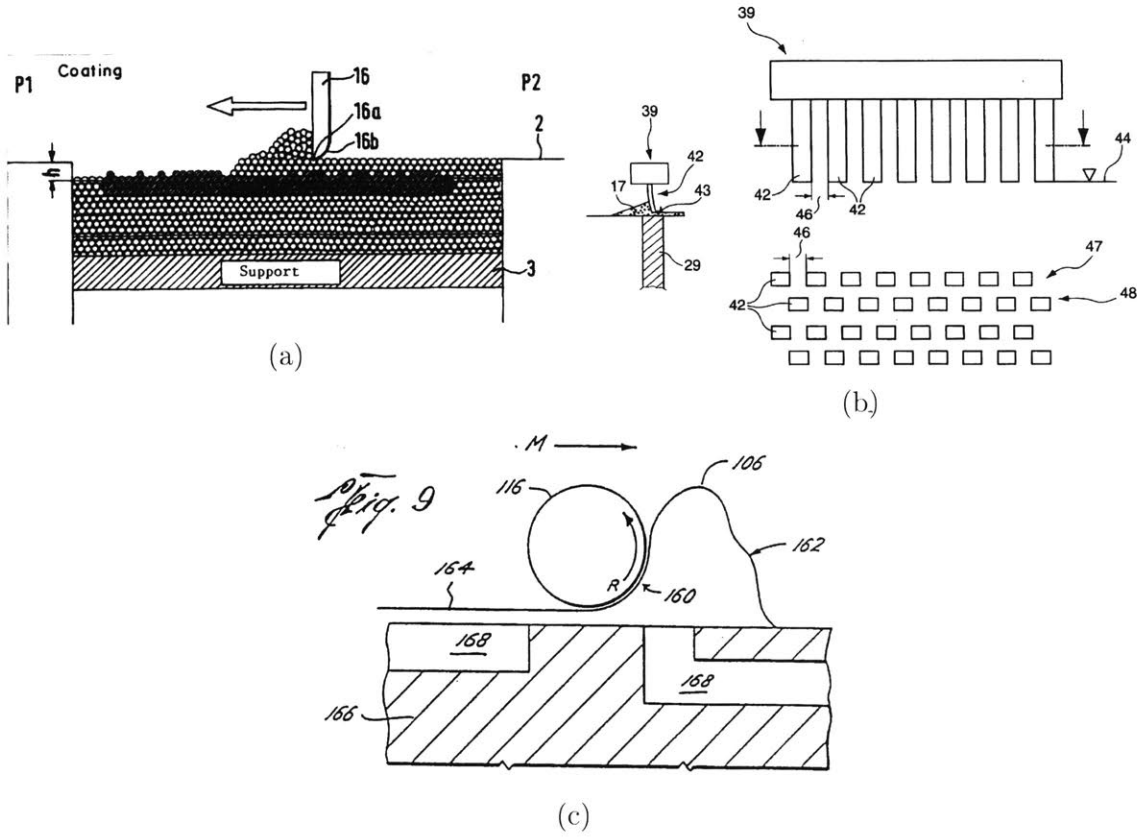

Figure 2-19: Various kinds of recoating systems including (a) rigid recoating blade, (b) flexible recoating blade array, and (c) counter-rotating roller [65][61][66].

designs, but they can largely be classified into two categories: blades and rollers. A blade style recoater is essentially a knife edge that is raked across the build surface, and come in the form of everything from a single rigid piece of metal, to multiple rows of interspersed flexible teeth [65][61]. The blade style recoaters achieve an even layer by pushing a wave of material ahead of the blade and shaving it down to the desired thickness. In contacting a protrusion, the reaction depends on the construction of the blade - rigid ones may just shear off the protrusion, potentially damaging the underlying part, while flexible blades deform around it.

In contrast to blade recoaters, roller style recoaters spin as they move across the build surface. Consisting of a counter-rotating cylinder, or other moving surface, the roller is driven across the platform pushing a wave of powder ahead of it [66]. When encountering a protrusion, the roller style recoaters can deflect over it stead of striking it. One additional feature of the roller is that it can compact the build material as

it recoats, generating a higher density powder bed. However, this does come with the potential to damage the part if it is particularly fragile, and may not produce as uniform a layer due to powder movement and compaction. One method for getting around this is to combine the systems and have both a roller and a blade used in succession - the blade recoater lays a thicker than normal layer and then the roller recoater compacts it down as seen in figure 2-20. A different extension of the roller recoater is to replace it with a horizontal grinding drum, this serves the function of both recoating the powder and remove any protruding surfaces [67].

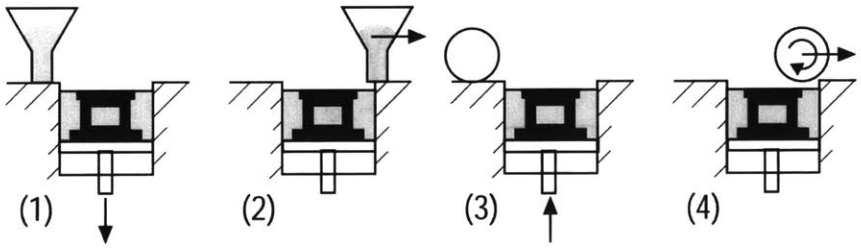

Figure 2-20: Combined process in which a rigid recoater lays down a thick layer that is then compacted by a forward rolling drum [68].

The design of the recoater changes as the layer thickness shrinks beyond a certain point. While the layer thickness is largely determined by the vertical stage in the build platform, the recoater can play an important role at small scales. In designing for very small layer thicknesses, those below 25 µm, special design considerations for the recoater have to be taken into considerations due to the fact that gravity-driven flow is no longer sufficient to properly fill in the layer. Instead, the powder is laid down in one direction, and then a doctor blade is drawn across in the other direction [69].

In designing the powder control system, the designer has to make trade offs based on the space available. The largest dictating factor is the size and shape of the machine, and where the powder system can be located. In some specialized designs, it may only be feasible to construct the powder hopper in one corner. If highly space constrained, it may be more reasonable to have a small hopper and refill from an external source as needed. Additional features such as heating systems or agitators may also be incorporated into the hopper. As discussed in section 2.3.1, the storage

vessel may be equipped with a heating system as it improves part quality by ensuring the material is up to temperature before being applied. When it comes to designing the recoater, while there are a whole host of design constraints to consider, the complexity trade-off comes to the forefront. Traditional rigid recoaters offer good performance but come with the danger of striking the part. If the designer is willing to accept additional complexity, incorporating rolling elements has the potential to increase part performance from higher powder bed density.

Environmental Control

The environment in which the build material is processed, including the temperature of the powder bed as well as the content, pressure, and flow of the ambient gas within the build chamber, plays an important role in the formation of the final part. From a machine design perspective, this contributes to whether or not the build platform, feedstock, recoating system, and ambient gas are heated as well as if and how the gas flows across the build surface.

Preheating the powder bed, ambient atmosphere, feedstock, and recoater roller/blade system all contribute to the thermodynamic process of the energy source interacting with the build layer. This effect has been shown to influence everything from the final microstructure of the printed materials to the level of distortion in the printed parts [70][71]. However, this impact is not universal as there are some materials that do not benefit from preheating [72]. Given the advantages for many materials, most commercial systems are equipped with a heated build environment. Additionally, the contents of the atmosphere, in particular the presence of oxygen, plays an important role in the quality of the part. As oxygen content is reduced, oxidation of the material decreases, which leads to better laser absorption, less balling, and faster build speeds [73].

Laser Fusion Environmental Conditions An important event in the laser-driven powder fusion process is the generation of a laser plume in the region where the laser strikes the build surface, and how that plume interacts with the build space environ-

ment. The build space may be left open to the environment, sealed and filled with a shielding gas, or even held under or above atmospheric pressure. The selection of this environment is important because it plays an important role in the formation of the weld plume, impacts laser performance, and potentially contributes to porosity. The source of these factors is the weld plume itself, a cloud of multiple materials that forms due to the laser-metal interaction. The weld plume consists of plasma generated from metal ionization [74], metal condensates from gaseous metal vaporizing from the melt pool and then recondensing [75], as well as liquid spatter and powder particles ejected from the build surface [76]. Figure 2-21 shows a depiction of what the plasma plume and ejected materials look like.

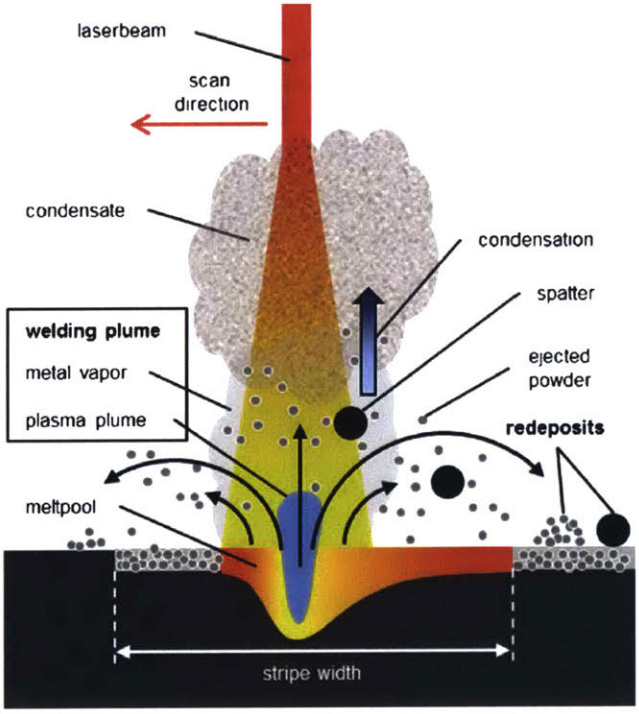

Figure 2-21: Representation of the various process by-products generated during the laser-driven powder fusion process [77].

The plume and material redeposition have a significant impact on the repeatability of the SLM process as well as playing an important role in the final porosity of the part. The plume both absorbs and reflects incident laser radiation, up to 40% [78][79], reducing power delivered to the bed, dropping the intensity of the laser spot, and leading to reduced strand diameter of the melt pool. Additionally, this plume

scatters incoming radiation resulting in a larger spot size and lower energy density which ultimately leads to poorer consolidation of the build material. The redeposited material generated alongside the plasma plume also impacts final part quality. By scattering particles across the surface, this ejection of materials artificially increases the powder layer thickness. This increase in thickness can lead to poor adhesion and porosity in subsequent layers in addition to generating features that may be struck by the recoater [80]. By properly shielding the build surface from the plasma plume and particle redeposition, the final part porosity can be significantly reduced [77][81]. While controlled gas flow holds the potential to significantly improve process performance, it has yet to be widely implemented in commercial systems.

EBM Environmental Conditions In electron beam melting, the chamber must be under vacuum to function properly, which leads to a different set of consequences. In order to prevent gas molecules from interfering with the electron beam, the build chamber is held at less than $5 \times 10^{-2} Pa$ [82]. However, this pressure must be increased slightly with a small amount of helium to reduce the electrical charging of the build chamber, bringing the pressure up to 0.3 Pa. The consequence of this is that there is increased melt pool vaporization and a shift in the mechanisms of heat transfer **gong_13__proc_param_ebm**

Design Implications In choosing to control the atmosphere of the build chamber, the complexity of the system design and control increases significantly. Simply displacing atmospheric gases with a controlled mixture only requires an air-tight vessel, or semi-sealed vessel with positive chamber pressure. To achieve chamber pressures above or below atmospheric pressure, the complexity of the design increases significantly as the vessel must now be capable of withstanding the forces acting on the build chamber, which is essentially a pressure vessel. Both systems bring the added complexity of incorporating a gas control system including the gas source(s), mixing and regulation, piping, and feedback control if present. Additionally, all of the control and drive mechanisms crossing the boundary of the build chamber must be designed

in a way that is gas-tight. In summary, the addition of atmospheric control presents the potential for significant process improvement, but also brings with it a significant increase in design complexity and fabrication cost.

Sensing and Control

Sensing and control within the powder bed fusion process leverages closed-loop feedback from system monitoring to improve process performance. The concept of feedback control applies across multiple time scales, each of which has its own means of sensing and contribution to product quality. On the shortest timescale, sensing can be used in online control of process parameters such as laser power and scan speed. Examples of this include optical monitoring of the laser emission profile and power as well as thermal monitoring of the melt pool size and temperature. On a longer timescale, feedback control can be implemented between printed layers. By using optical scanning and non-contact profilometry, defects on each layer can be tracked and used to determine part performance, or corrected for in subsequent layers. The longest timescale for control is inter-part control in which part measurements and performance metrics are integrated into the next build process to optimize quality.

Integrating sensing and control into the powder bed fusion process has demonstrated the capacity to reduce defects, improve part quality, and provide additional material property control. Within a build layer this can be seen in creating overhangs in parts, the different thermal properties from printing over previous layers to printing over powder leads to defects such as high surface roughness and balling. A similar phenomenon is seen in acute corners where the laser must reverse direction due to the dwell time of the laser in the corner. By implementing feedback control, an example system can be seen in figure 2-22, these defects can be mitigated, creating a higher quality part with more consistent overhangs and corners [83]. Between layers, feedback control can be used to detect and report machine performance and part quality. An excellent example is using optical sensing to determine the wear condition of the recoater blade [84]. Over time, the recoater blade wears and begins to create ridges in the powder bed which leads to part inconsistency, feedback allows this to be detected

and reported. Beyond corrective action, feedback control can also be used to control material properties. By closely controlling the temperature of the melt pool, the final microstructure of the parts can be manipulated over the volume of the part. [85].

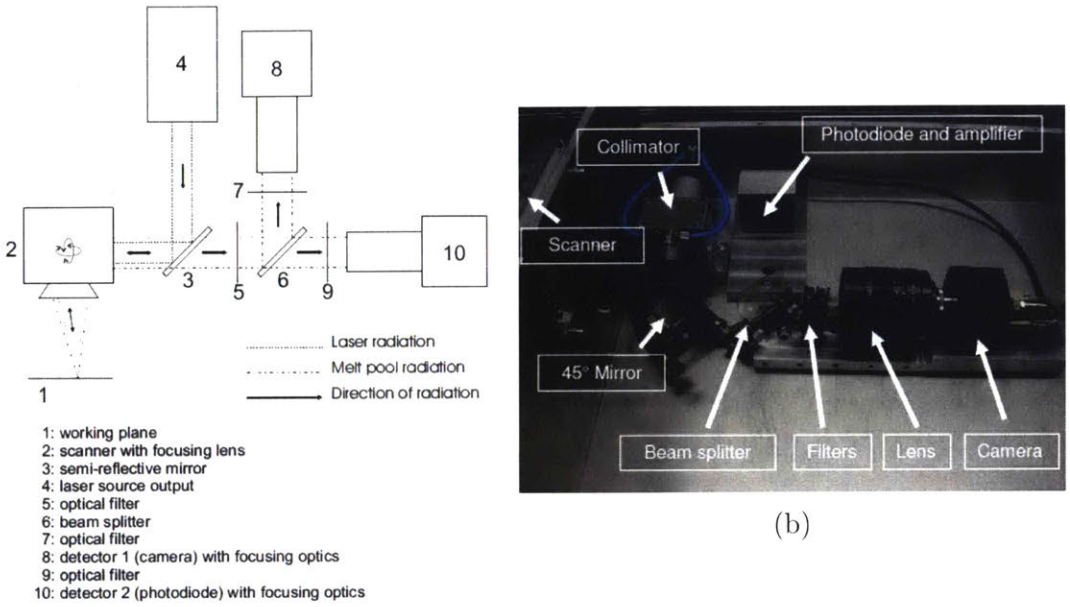

Figure 2-22: Schematic and implementation of a two-sensor, photodiode and camera, used for online control of laser power and other process parameters [83].

While integrating online feedback and control presents many opportunities for process improvement, it carries with it significant challenges to implementation. The primary obstacle to feedback control is the data bandwidth required. For a system scanning at $1\,\frac{\mathrm{m}}{\mathrm{s}}$, measurements must be taken at a rate of 10 kHz in order to reach a spacial resolutio of 100 µm. While this may be a reasonable sampling rate for a point sensor such as a photodiode, visual sensing methods, such as thermal cameras, carry significant data given they are recording a 2-dimensional field. Another obstacle to implementation is properly calibrating and sensing the environment. Thermal imaging systems, some of the most widespread for feedback control, only function when the emissivity of the material is known. Not only do all of the build materials need to be characterized to quantify their emissivity, but additional compensation is needed as the emissivity changes from the powdered state to the consolidated state.

2.3.2 Anatomy of a Powder Bed Fusion Part

Build Materials

The raw feedstock for powder bed fusion is a fine powder of the desired build material. Feedstock is available in a variety of pure metals including titanium, tantalum, copper, and gold as well as a broad range of alloys including those based on titanium, nickel, iron, and aluminum [86]. For plastics, material options include Nylon, ABS, thermoplastic elastomers, and polyamides [87]. While virgin, or unused, powder is the best material to work with, it possible to reuse non-fused powder to reduce production costs, and many commercial systems are equipped with complex powder recovery systems to do this. However, the use of recycled powder can impact part quality due to the potential for handling contamination, dealloying, chemical contamination, and exposure to oxygen and humidity.

To create these powders, there are a variety of production methods depending on the desired final properties and overall quality. Some of the most common methods for producing the feedstock are centrifugal or rotary atomization, gas atomization, and plasma-based methods such spheroidization and rotating electrode processing. Figure 2-23 shows samples of some of the most common means of producing the powder feedstock.

There are a host of different feedstock qualities that play a role in the final product. From a physical perspective, the size and shape play an important role in the flow mechanics of the powder, as does the surface morphology. On the chemical side, the composition and uniformity of the powder is also important as is the inclusion of any impurities or gases. From a machine design perspective, these physical characteristics contribute to two key functional properties: flowability and apparent density. Flowability is how well the powder flows, and has a significant impact on the powder handling and recoating system. Apparent density is how well the powder packs when it is laid down, important for the design of the recoater system. Ideally, the feedstock would be highly spherical and contain little to no surface satellites to allow for the greatest flowability and apparent density.

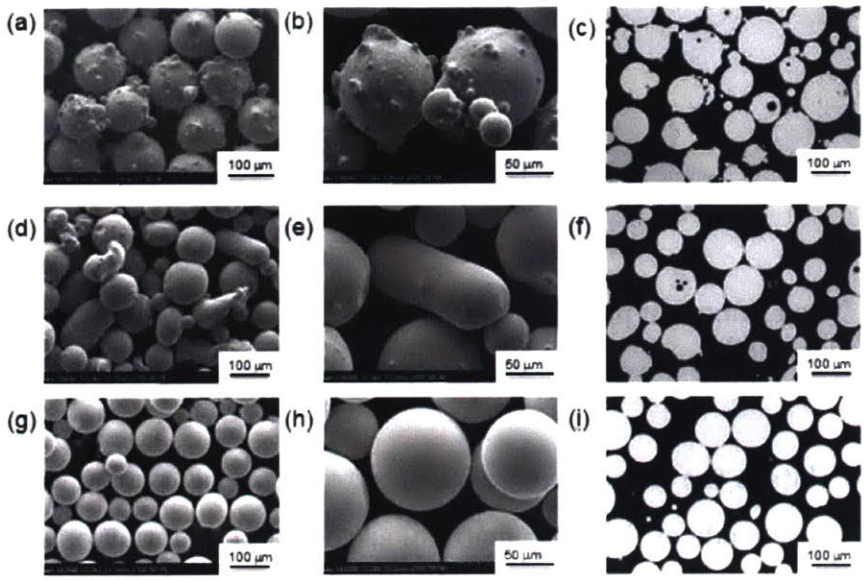

Figure 2-23: SEM images of samples of (a) gas atomization, (b) rotary atomization, and (c) plasma rotating electrode processing atomization. [88].

Particle size, and particle size distribution, play a key role in the handling properties of the feedstock and the final part quality. For laser-based processes, the feedstock generally ranges from 10 µm to 45 µm while EBM systems generally use larger feedstock at 45 µm to 106 µm to compliment their thicker layers [89]. The size and distribution of the feedstock plays a role in the absorption of the incoming energy, the dynamics of the melt pool, and the formation of defects [90]. Powders with narrower particle size distributions tend to exhibit higher ultimate tensile strength and hardness. In contrast, powders with wider particle size distributions tend to produce parts with higher density, smoother surface finishes, and require less energy to fuse [91]. Regardless of the distribution used, it is important that the powder handling system does not significantly alter it, or allow the powder to separate such that the distribution changes over the volume of the build.

Part Macrostructure

When removed from the machine, the part consists of three primary components: build plate, support structure, and the part itself. An image of this can be seen in figure 2-24.

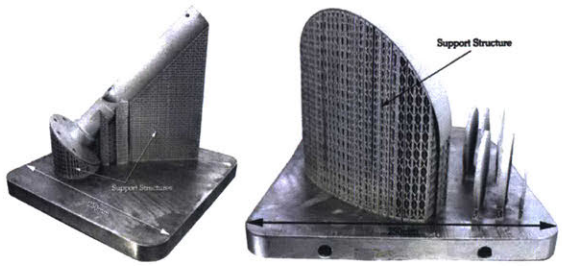

Figure 2-24: Two example of parts still anchored to their build plates with the support structure in place [92].

The build plate is the substrate on which the top serves as the foundation for the part. This may be made of the same material as the build material, or be a different material. It is separated from the part by cutting it off with a saw or using a wire EDM machine, or, in some cases, the part can be broken off the substrate by hand.

The support structure is a sacrificial scaffold that supports the part throughout the printing process by providing mechanical and thermal anchoring. These structures play a key role in preserving part features, such as inclined surfaces below 35° and overhanging structures, that are not properly supported by the powder bed alone. The support structure also mechanically anchors the part so that it does not warp and crack due to the stresses induced in rapid thermal cycling. Figure 2-25 shows part warping and cracking that occurs when the support structure is not properly designed. Like the build platform, the support material must be removed from the part by either cutting it away, or manually broken off.

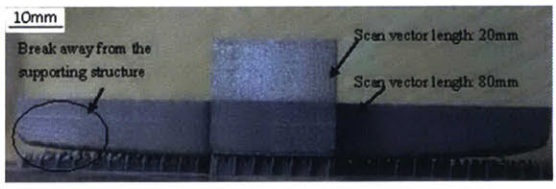

(a)

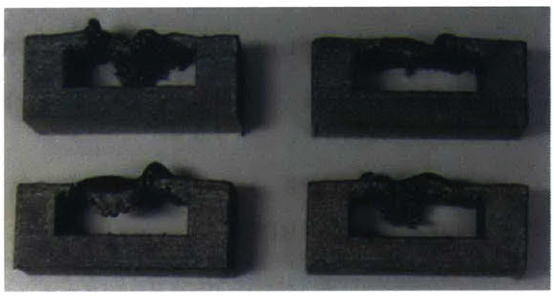

(b)

Figure 2-25: Examples of part failure due to insufficient support including (a) part warping and lifting of off the build plate and (b) build failure on an overhang [93][94].

The part itself can also be broken down further on a macroscopic scale into the skin or perimeter and the infill. A boundary or perimeter feature is any surface that defines the shape of the part. Collected together, all of the boundary surfaces form an empty shell of the part. Contrasting this is the infill region, which is the volume enclosed by the boundary surfaces. Figure 2-26 shows a slice from a generic part and denotes the perimeter and the inner hatch scan paths. The distinction between these is important because the laser scan strategy and process parameters are different for each of these.

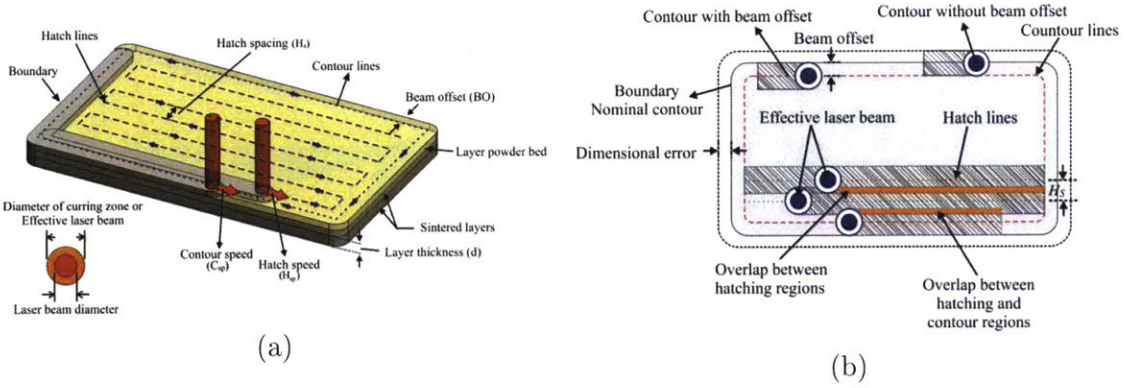

Figure 2-26: The beam trajectories and process parameters used to generate a single build layer [43].

An important part quality that the scan strategy can contribute to is the outer surface roughness. The surface roughness of a part is derived from two sources. The first source of surface roughness is the thickness of the layers used to print. Due to surface tension as the material cools, the edges of each layer are rounded instead of vertical. The other source of roughness is satellite attachment to the perimeter of the part. As the build material is fused, it is possible for particles to partially fuse to the exterior without melting. Figure 2-27 shows the two forms of roughness combined together.

Simply reducing the layer thickness to increase part smoothness is a trade off with time. While it may seem an easy solution to reduce the layer thickness in an effort to improve surface roughness, each layer requires a fixed amount of time to build. Halving the layer thickness in hopes of halving the roughness factor has the consequence of doubling the build time. Additionally, the powder feedstock size plays

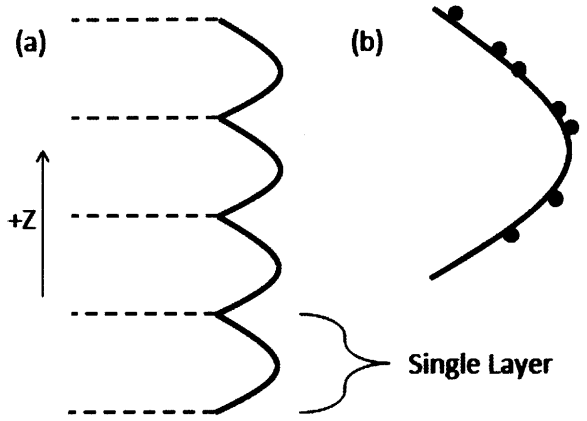

Figure 2-27: A drawing of the two primary contributors to surface roughness: (a) layer thickness and (b) satellite particle adhesion [95].

a significant role in limiting the minimum layer thickness that can be consistently laid down due to the flow mechanics. Table 2.1 shows the layer thickness ranges for laser and electron systems in addition to the feature sizes achievable. In designing a part, as with layer thickness, there is a lower limit on the feature size that can be achieved. Through a combination of thermodynamic, minimum focal size, and powder size, commercial production powder bed fusion systems are limited to features sizes no smaller than 100 µm.

Table 2.1: Comparison of feature sizes in laser and electron-based systems [96][97][98][99][100].

Parameter	**Laser-Based**	**Electron-Based**	**Units**
Layer Thickness	10-100	50-200	μm
Build Rate	up to 105	55-80	$\frac{cm^3}{hr}$
Min Feature Size	100	100	μm

Part Microstructure

Central to the performance of the fabricated parts is the microstructure of the fused material. For metals, the microstructure is particularly of interest as the mechanical properties can change significantly based off the microstructure that develops in the fusing process. One challenge is that the phase formation of the microstructure is highly dependent on the process parameters and build material, and the parameters

needed to provide a high density macrostructure, may create a microstructure that is less than ideal. Another common feature that occurs on the microscale is the most frequent defect in powder bed parts - the generation of pockets or inclusions that reduce the density of the part.

The most common grain structure in powder bed fusion is a highly-oriented columnar grain structure oriented vertical to the build plate. While the build material can play a role in the grain structure produced, this columnar structure is common across many build materials due to the remelting of several layers beneath the build layer [101][102][103]. An example of this highly oriented grain structure can be seen in figure 2-28.While the columnar structure is common, the grain structure of the part is also dependent on the scan strategy employed to create the infill. The repeated island scan strategy, where small squares are fused together to reduce the buildup of residual stress, generates fine, repeating square of compact columnar grains. In contrast, the rectilinear rastering, repeatedly running lines across the length of the part, generated much larger, unordered columnar grains [104].

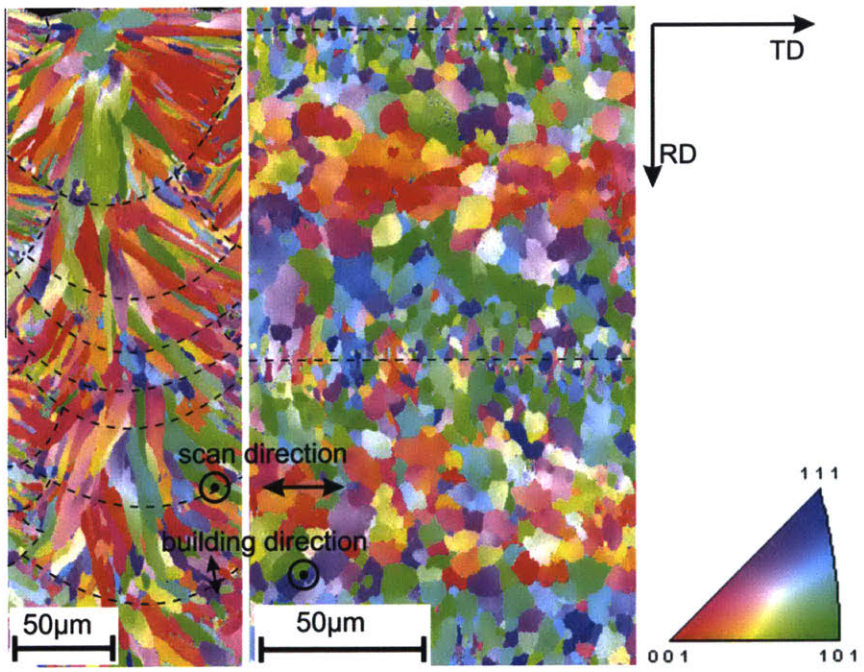

Figure 2-28: A colored EBSD map showing the (left) front view and (middle) top view of a sample of AlSi10Mg fused with a bidirectional, longitudinal scan strategy. Dashed lines represent the melt pool borders [105].

Regardless of scan strategy, the rapid solidification of the melt pool contributes to a smaller average grain size when compared to traditional casting methods [106]. This rapid solidification can also lead to the precipitation of an intermetallic phase with process parameters that lead to high heat input with alloyed build materials [101]. Additionally, there is a distinct difference between the infill and the perimeter of the part. Fine-grained equiaxed microstructures tend to form on the perimeter of the part while the interior infill regions have a highly oriented structure as mentioned previously. The difference in the microstructure is derived from the difference in melt sizes as the perimeter is generally fused at high speed with a fine spot size in order to generate a sharply defined perimeter. In contrast, the infill is fused with larger spot sizes and larger melt pools in order to fuse the inner region as quickly as possible. The pattern of different grain structures can even be seen within the melt pool itself as the crystal structure varies from the edges to the center due to the different cooling rates [105].

One of the many desired features in powder bed fusion is to be able to selectively control the crystal grain structure of the part being produced. As mentioned in section 2.3.1, this can partially be achieved through the manipulation of the build layer thickness, but not necessarily across the build layer. Increasing the fidelity of the feedback and process control allows for control within the build layer, as has been seen with EBM process of Ti6Al4V where the metallic grain size was controllably increased and decreased by 50% [107]. The technique has been taken even farther to allow for control of the crystallographic orientation within the build plane by controlling the scan strategy and heat source modes to promote either steady-state or transient thermal gradients [108]. Figure 2-29 shows a depiction of the crystal orientation control. This is a remarkable achievement as the site-specific control of crystallographic orientation of grains within metal parts had been unachievable until additive manufacturing methods were developed.

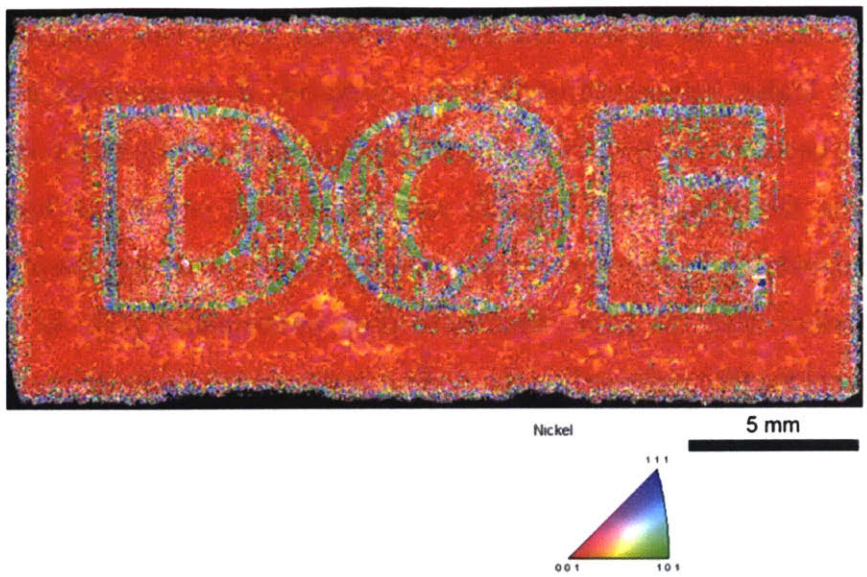

Figure 2-29: An EBSD cross-section of an FCC nickel component fabricated on an EBM machine showing the locally controlled crystallographic orientation [108].

2.4 Influences of Pressure

Changes in pressure alter the melting and boiling points of materials and could offer a control mechanism for controlling defect generation as well as creation of new kinds of part features. In particular, for materials such as metals and alloys, increasing pressure creates an increase in the temperature gap between the melting and boiling and temperatures. This is significant in that is allows for a greater range in temperature before a process runs the risk of excessively vaporing the base material, or altering the percentages of the alloying elements. In order to build at a desired rate, it is necessary to create a melt pool of a specific diameter and depth traveling at a specific speed. To create this melt pool, there has to be the requisite energy input into the system to melt the build material and form it into a solid feature integrated into the layer below it.

Forming a features happens through the formation of a melt pool at the laser-material interface, and the transfer of energy from the laser into the melt pool, and then into the surrounding material. Due to thermal resistance, a temperature gradient forms over the melt pool: the material is right at its melting point at the edge of the pool, and the temperature increases towards the laser contact region. The faster

a part is constructed, the greater the energy transfer across that resistance, which gives rise to a higher temperature gradient. However, if the material in the laser contact region becomes too hot, exceeding the boiling temperature of the material, or certain alloying elements, it will begin to vaporize forming jets of gas, high-velocity convection currents and vapor condensate plumes, which push and distort the melt pool and interfere with the laser, leading to poor performance [77]. In particular, as the melt pool surface approaches the boiling point, recoil pressure on the surface of the pool generates an exponentially increasing normal force, accelerating the pool [109].

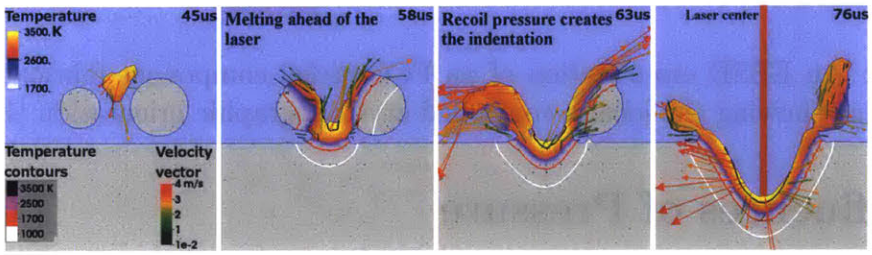

Figure 2-30: Velocity and temperature fields of a later 2D slice showing the effect of recoil pressure driving the molten metal out of the path of the laser. [109].

Outside of melt pool dynamics, pressure plays a significant role in the composition of alloys. Each elemental compound in an alloy has its own melting point and vapor pressure, and, while alloys for powder bed processes are generally engineered to match melting points, this difference can create process problems. An examples of this is AZ91D, a magnesium die casting alloy with zinc as a major alloying element. An issue with high-energy processing this compound, a popular structural alloy, is that zinc has a vapor pressure an order of magnitude higher than magnesium [110]. Due to this significant difference, the final part had a significantly decreased zinc content that the standards for AZ91D, altering its mechanical and chemical properties [111]. Increasing the environmental pressure could help suppress the loss of the zinc, and prevent significant dealloying.

An example material that is both a popular structural material and difficult to work with is magnesium. At atmospheric pressure, magnesium is a challenging material to work with due to the limited gap between the melting and boiling points.

Recent experiments have verified that magnesium can be fused at atmospheric pressure, but the produced parts did not have smooth sides or definite straight edges due to the vaporization of the powdered build material [112]. However, the issue of excess vaporization can be overcome using pressure. The calculated solid-liquid, solid-vapor, and liquid-vapor transitions lines plotted as a function of pressure can be seen in figure 2-31. At atmospheric pressure, 101.3 kPa, the gap between the melting and boiling points of magnesium is only $452°C$. By increasing the system pressure by 1.029 kPa, or approximately 10 times atmospheric pressure, the boiling temperature increases to $790°C$. The increase in pressure affords an additional $338°C$ of temperature range over which the system can operate. This increase in the molten temperature band allows for greater process control that eliminates the need for alloying of the build material to suppress its boiling point.

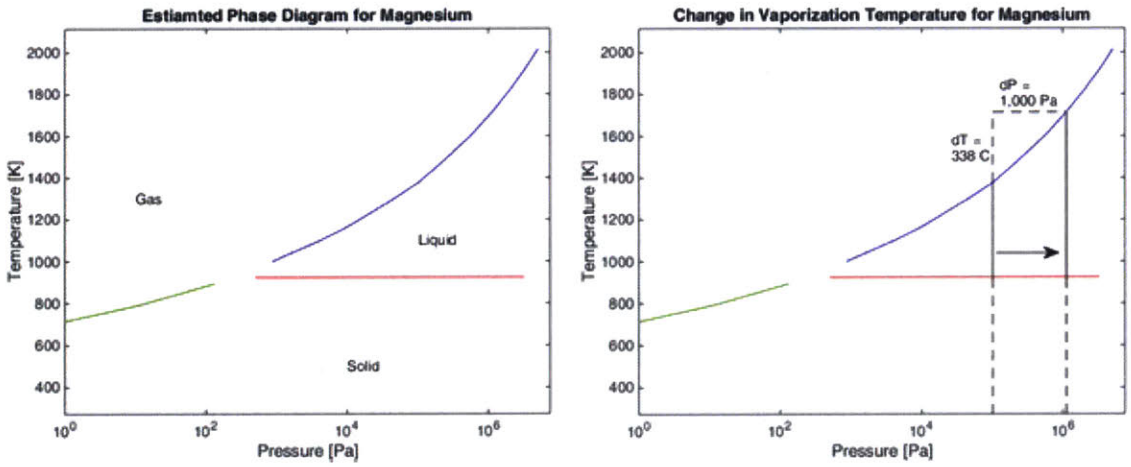

(a) (b)

Figure 2-31: Estimated magnesium phase diagram (a) from incomplete thermodynamic data in literature, and (b) the impact of increasing atmospheric pressure [113][114][115].

Another role in which pressure has a potential application is the creation of variable density structures. The contrasting point between this application and those mentioned above is that the pressure is not the environment's pressure, but pressure generated within a part that can create voids. Chemicals known as gassars are designed to generate large volumes of gas when they decompose due to thermal or chemical activation. Gassars have long been used in the fabrication of metals foams by

blowing bubbles into a vat of molten metal. These rigid metallic foams have a broad application space in shock absorption, sounds damping, and prosthetics [116][117]. Figure 2-32 shows pair of examples of metal foams and their application.

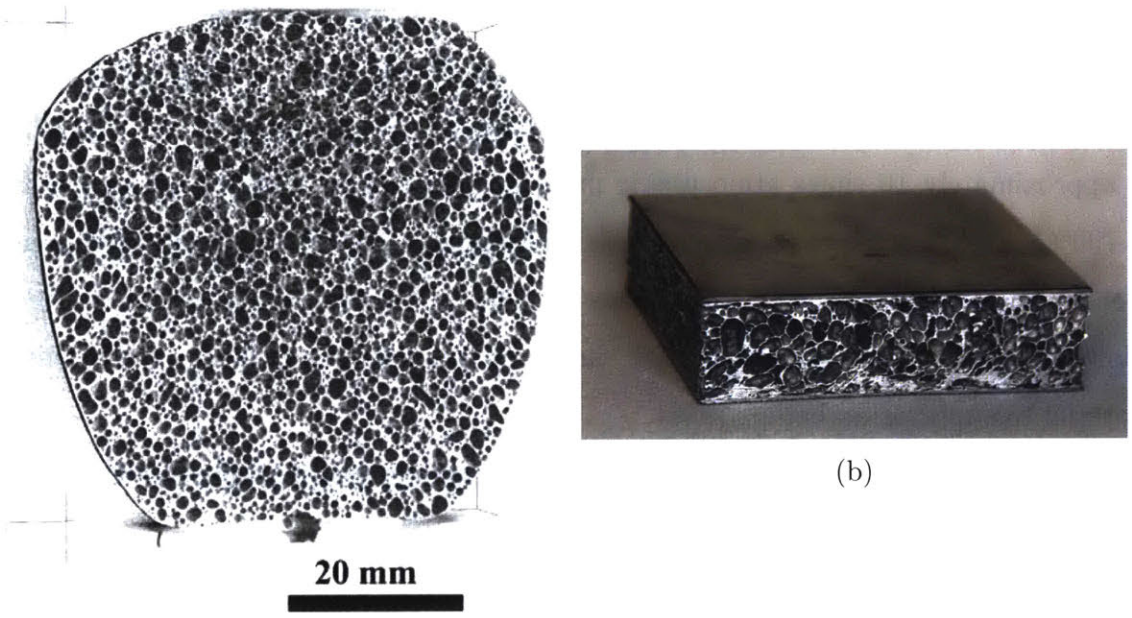

(a) (b)

Figure 2-32: Metal foams present a unique combination of stiffness, ductility, and low density structures as seen in (a) which are commonly used in laminated panels (b) that offer stiffness but low weight [118][119].

Leveraging gassars within powder bed fusion opens up the opportunity to create parts with variable density. Initial work has demonstrated the feasibility of generating micron-sized pores in powder bed fusion parts, seen below in figure 2-33. By incorporating ammonium carbonate (NH_4HCO_3), boric acid (H_3BO_3), or potassium tetrafluoroborate (KBF_3) into the build material, the particles became suspended in the melt pool during the material melting process [120][121]. As the pool cools and begins to solidify, the gassars decompose and give off gas due to heat transfer from the melt pool to the particles. As they decompose, the gas creates a bubble, that is then frozen in the structure as the melt pool resolidifies. Initial experiments have demonstrated the pore shape, size, and orientation can be manipulated by process parameters [121]. Further refining of process parameters and the gassing agents them-

selves holds the potential to allow for selectively activating the gassing agents. This effect could also be coupled with the ability to manipulate the atmospheric pressure to help control the dynamics of the pore formation. With control of these parameters, it will become possible to spatially vary the density of a part in the powder bed fusion process, unlocking a whole region of the design space.

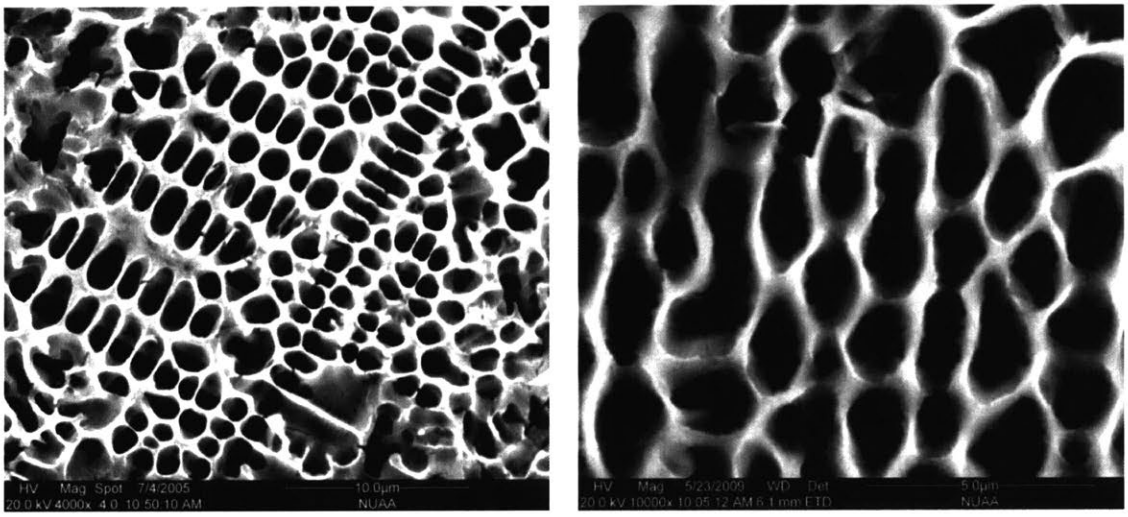

(a) (b)

Figure 2-33: Demonstrations of foamed stainless steel in a powder bed fusion machine showing the micro-sized pores generated from (a)potassium tetrafluoroborate and (b) ammonium carbonate [121][120].

2.5 Current Challenges

Melt Pool Dynamics A wide array of defects and part quality issues can be related to the complex dynamics of the melt pool. One melt pool dynamic of interest is the surface tension driven Marangoni flow that distorts the melt pool's shape. This effect is created by the thermal gradients across the melt pool, and proper control can lead to higher part density, reduced oxidation, and lower surface roughness [63]. Another form of defect attributed to complex hydrodynamic melt pool flow are keyhole voids, seen in figure 2-34. These defects cause lower part densities and can serve as the seed point for part failure. Recent simulations have demonstrated the important role that

recoil pressure plays in generating those keyhole defects [45]. Understanding the melt pool dynamics is the first step in achieve higher quality and more consistent parts.

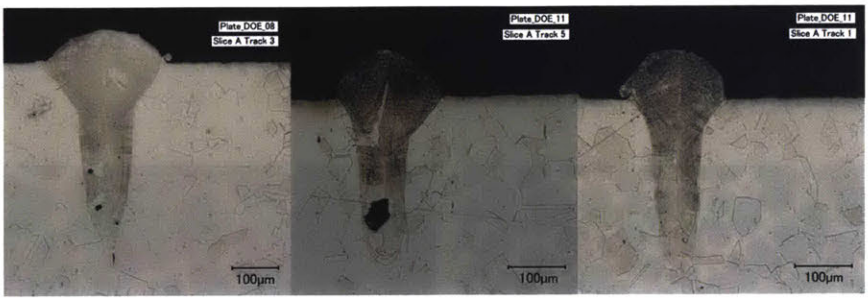

Figure 2-34: Examples of keyhole defects in a melt trace leading to poor part density and potentially acting as failure points. [122].

The challenge with the melt pool dynamics is that they are difficult to observe, model, and control. As discussed in section 2.4, the melt pool behavior is subject to a wide array of complex hydrodynamic forces and incorporates rapid phase changes between solid, liquid, and gas. Tackling this problem will require building the tools to properly measure the melt pool in-situ as well as building models with the level of sophistication needed to act as predictive tools. Beyond those steps, new process techniques needs to be developed that can either control or suppress the undesired melt pool dynamics, including the investigation of pressure control to mitigate recoil forces.

Materials and Processing Despite growing use of powder bed fusion, there is significant room for exploration in materials and material processing. Current fusion processes are limited to steels, both tool and stainless, aerospace and implant grade alloys like titanium and cobalt chrome, and nickel super alloys. While aluminum and magnesium materials are being explored, the previously mentioned issues with oxidation and dealloying pose significant problems. Most new materials are explored through parametric searches of the process parameters, which is a slow and laborious task. The development of new simulation methods will open the door to rapidly identifying new materials and their ideal process parameters.

Furthermore, the post-processing techniques currently employed are not well understood or characterized. Due to the significant thermal gradients in parts, thermal post processing is necessary to relieve residual stress and control grain structure. A challenge in this is that the thermal post-processing behavior of additively manufactured parts varies significantly from traditional, and well understood, processes such as wrought or forged materials. To address this, the post-processing methods such as hot isostatic pressing, heat treatment, and welding need to be well-characterized to fully understand their impact on part performance.

While many new materials can be leveraged through the manipulation of process parameters, modify the process or the machines may be necessary for some materials. As discussed in section 2.4, there is an issue when working with alloy build materials where the alloying elements have significantly different vapor pressures and/or melting points as well as with materials that have close melting and boiling points. The application of pressure control is one potential route for gaining access to these materials. Another system or process level challenge is that materials that are highly oxidation prone, such as aluminum, are challenging to work with as the material is generally handled and loaded in air.

Modeling and Simulation Modeling is critical to the broad application of additive manufacturing. As discussed in section 2.2, the input parameters to the powder bed fusion process is an incredibly high-dimensional search space. A lack of accurate modeling packages requires physical verification of process parameters for each material used. Given the size of the parameter search space, it is cost and time prohibitive to qualify a material. In order to investigate new materials, new design concepts, and new processes, an accurate and efficient modeling system is needed.

The primary challenge with modeling powder bed fusion is that it spans multiple length scales, each of which has its own modeling techniques and goals. Figure 2-35 shows a depiction of the multi-scale modeling problem. At the sub-micron scale, the system must employ phase-field modeling to determine microstructural evolution in the non-equilibrium environment imposed by the high rate of change in thermal gradi-

ents. Moving to the particle or micron scale, the process is centered on beam-powder interactions and powder consolidation processes that inform meso scale simulation. At the meso or millimeter scale, the system must model material phase change dynamics and fluid flows that are dependent on part geometry and beam trajectory. Lastly, at the macro or meter scale, the simulation centers on thermo-mechanical properties of bulk regions such as the powder bed and solidified part to determine residual stress, distortion, and final shape.

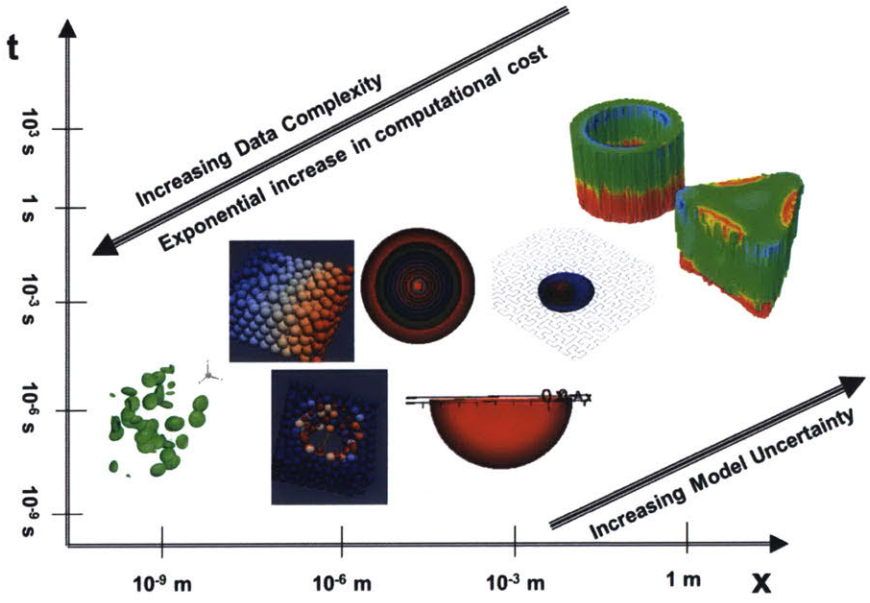

Figure 2-35: The various hierarchies in the modeling process and their relationship with data complexity as well as uncertainty. [82].

The multi-scale problem is compounded by the resolution issue of high thermal gradients and a large build platform. Due to the large thermal gradients within the melt pool, a fine mesh size is needed to accurately capture the material dynamics. However, the total build volume is quite large and working with a mesh on that scale would be intractable. Modeling software is needed that can handle variable mesh sizes, and dynamically reconfigure to match the moving area of interest.

In addition to resolution and mesh sizing, the powder bed process presents another complex challenge in the physics of the process. The melting, flow, and resolidification of the build material presents a complex multi-material, multi-phase system with complicated thermal-structural fluid dynamics. The rapid gas-liquid-solid phase

change seen in the melting, boiling, condensation, and solidification phenomena are compounded by other complex issues such as non-linear surface tension, Marangoni circulation, and recoil pressure. Modeling and simulation tools must be able to accurately capture and represent these complex interactions.

Even with an accurate modeling system available, the lack of process-specific design and manufacturing tools limits their application. In order to incorporate the understanding of microstructure, residual stress, part distortion, and other qualities, the design tools producing the parts need to leverage that information.

Testing and Evaluation A significant challenge to the widespread application of additively manufactured parts in critical roles, such as space and aerospace applications, is a lack of standardized guidelines for qualification and certification of parts. From machine process parameters to material qualities to part performance, there is no unified set of standards for testing and evaluation that allows for common communication of performance and capabilities. What is needed is a centralized set of tests and procedures that can be used for benchmarking machines, materials, and parts so that it is possible to make quantitative comparisons.

Even with a set of standards for part evaluation, the difficulty of this process is exacerbated by the lack of standardized build parameters across different machines. The implication of this is that there is no effective way of replicating a certain build sequence on different machine to build the same test artifact. Furthermore, variation from machine to machine, and the variability that different operators introduce through a lack of standardized training, makes the task of producing the same part in the same manner in different places extraordinarily difficult. What is needed is a standardized application programming interface and file format to allow for uniform process commands across machines and manufacturers. Additionally, there is a need for a calibration process that can compensate for the differences in machines and operators to allow for uniform part production.

Beyond standards and procedures, the lack of measurement methods presents a challenge in properly quantifying the performance of a part. Most commercial

systems lack in-situ measurement methods which are central to monitoring the build process and providing closed-loop control of the process. The challenges imposed by a lack of sensing are amplified by the inability of the end-user to modify the system to incorporate those features due to intellectual property, warranty, and maintenance constraints. In order to track the build quality of a part for characterization, machines need to incorporate sensing and feedback systems that users can access and monitor.

Chapter 3

System Construction

In order to address the lack of process control with closed-architecture commercial selective laser melting machines, we chose to build our own SLM machine from the ground up. The work began with constructing a single-layer, 1-degree of freedom linear test platform for initial testing, and then continued on to create a multi-layer, galvanometer-driven system for full-scale experimentation. From a hardware perspective, we maximized the use of commercial-off-the-shelf components both to leverage as much pre-existing engineering as possible, as well as to make modifying and reproducing the system easy. On the software side, we created an open-source, modular software platform from a combination of readily available and custom software to allow for rapid modification, reconfiguration, and distribution of the control system. Combined together, these systems allow for extensive control of the laser melting process.

3.1 Linear Test Platform

The Linear Test System (LTS) is a 1-dimensional motion platform for exploring the effects of system parameters on the SLM process. The intent of developing the LTS was to provide a low-cost, low-complexity test system to allow for initial research while the more complex galvanometer system was being completed. Similar to any SLM

system, the LTS contains the same fundamental components: laser energy source, electromechanical beam positioning system, build platform, and recoating mechanism.

3.1.1 Mechanical System

The mechanical portion of the LTS is responsible for the precision motion and positioning of the optical objective over the sample. This system contains three major components: a gantry containing the linear motion drive and guide components, a sample holder that positions the sample within the machine, and a safety enclosure to protect the user from errant laser radiation. The components are combined together using a waterjet-cut 6061-T6 aluminum plate that serves as the base. A picture of the system and its CAD model can be seen in figure 3-1.

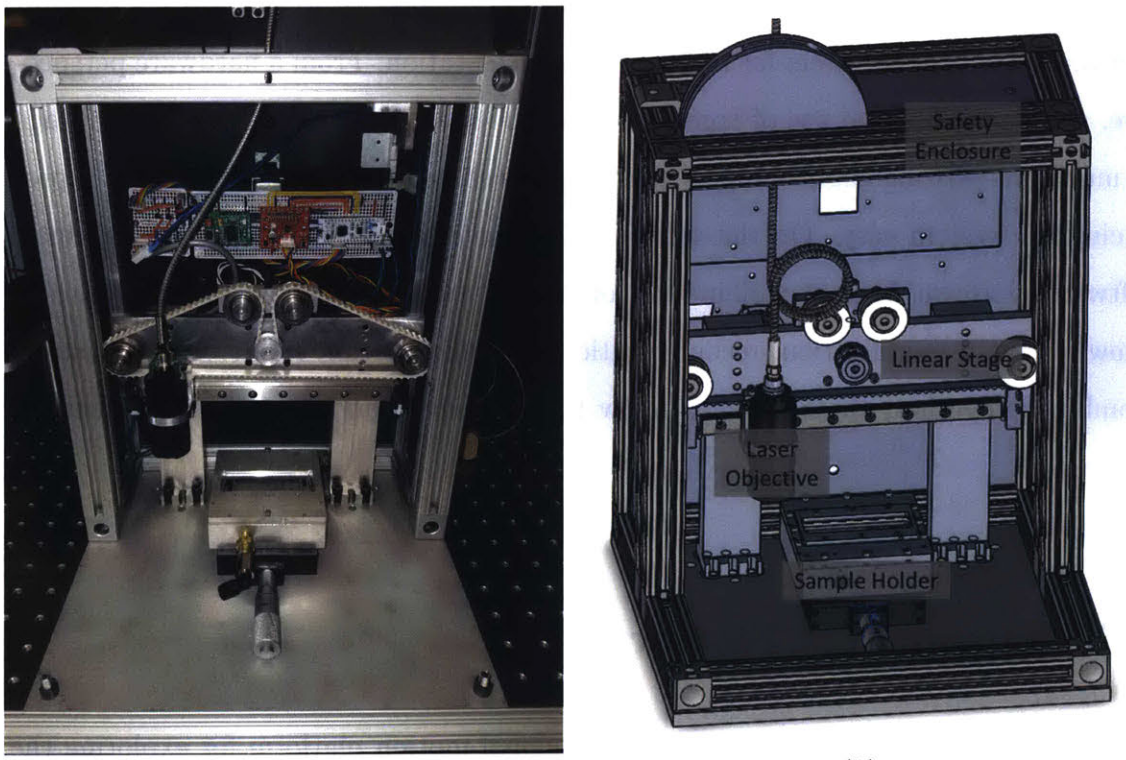

(a) (b)

Figure 3-1: Picture and CAD model of the linear test system.

Linear Gantry

The gantry is the linear motion stage responsible for positioning the optical objective over the sample according to a specified motion profile. The core of the gantry is custom-machine 6061-T6 aluminum structure comprised of two uprights onto which a faceplate is attached via precision dowel pins and socket cap head screws. The faceplate serves as the mounting point for the profile rail linear guide (McMaster part #6725K53) that constrains the carriage (McMaster part #8438K4) to linear movement. Attached to the carriage is a custom-machine 6061-T6 aluminum block that houses serves as a mounting point and integral component of the optical objective. The carriage is positioned along the linear guide via a timing belt driven by a triple-stack NEMA17 motor (Digi-Key part #17PY-Z444-99VS). The belts starts with one end in the belt clamp on the carriage, runs over a pair of idler bearings, around the motor drive pulley, over another pair of idler bearings, and then back to the carriage. To provide the appropriate tension on the belt, the top pair of idler bearings are mounted on a movable plate that can be extended. One additional set of components mounted to the gantry is a pair of microswitches (Omron part D3M-01K3-3 and D3M-01L3-3) located on each end of the profile rail which are used for calibrating the home position of the carriage and ensuring that it cannot be driven off of the end of the rail.

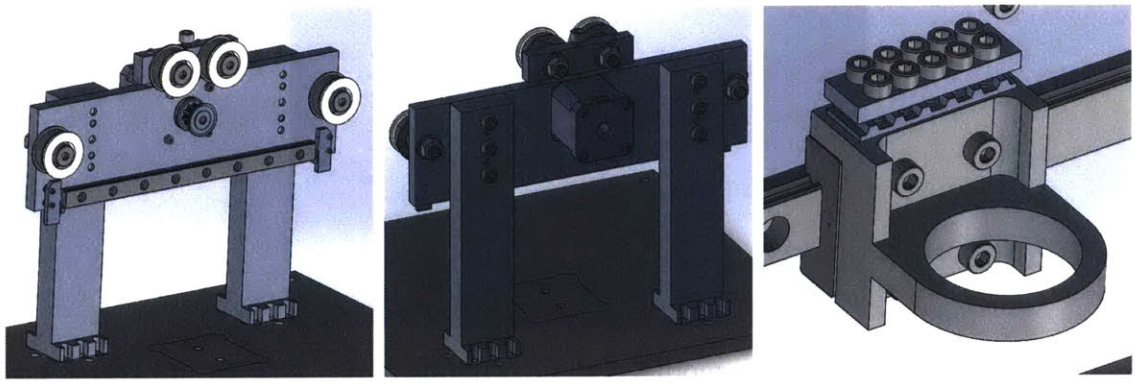

(a) (b) (c)

Figure 3-2: Model of the (a) front and (b) rear of the gantry as well as the the (c) carriage bracket.

Sample Holder

The sample holder is a machined case fitted with an optical window and a pair of gas ports that retains the sample within the experimental setup. This device serves a number of important roles including retaining the sample within the experimental setup, allowing for repeatable removal and insertion of the sample, shielding the sample from ambient gases, containing any emissions from the sample, and allowing for precise and repeatable recoating of the sample. Containing the sample in a sealed, removable vessel not only protects the sample from oxidizing atmospheric gases and the experimental setup from emissions that occur during the SLM process, but also allows for remote sample preparation which provides better access to the sample and reduces the chance of damaging the experimental setup. The construction of the sample holder can be broken down into five major components: body, lid, window, window retainer, and sample retainer. Assembled together, these components are bolted to the top of a micrometer adjustment stage to allow for fine positioning within the experimental setup. A picture of the sample holder and its CAD model can be seen in figure 3-4.

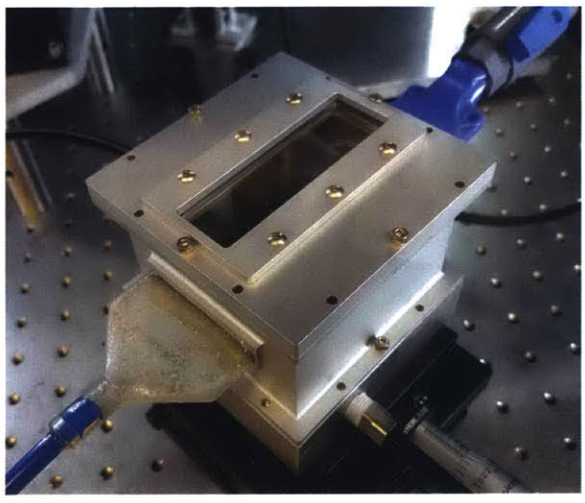

Figure 3-3: LTS sample holder modified to incorporate a rise with an integrated gas knife for more even gas flow.

The central component of the sample holder is the body which was machined from a solid block of 6061-T6 aluminum. To provide a controlled environment, the

(a) (b) (c)

Figure 3-4: CAD model of the (a) assembled sample holder, a view of the (b) internal cavity, and (c) with the recoater assembly in place.

body has a groove along the top surface designed to hold an o-ring as well as a pair of $\frac{1}{8}$ in NPT fittings on either end to allow for the flow of gas. Paired with the body, the lid was designed to retain the optical window and create a sealed chamber for the sample. Clamped to the body using a series of #4-40 cap head screws, the lid seals the sample chamber via the body's o-ring. The lid was waterjet cut from a 6061-T6 aluminum sheet and secondarily machined to create a relief in the top for the optical window. The optical window itself is a standard 75 mm by 25 mm microscope slide made from water white glass. Microscope slides were chosen for initial experimentation because they are inexpensive, easy to acquire, and disposable. The optical window is sealed within the lid using a pair of o-rings, one on either side to prevent any stress-concentrations from contact with the metal lid and window retainer. The two retaining plates, one for the optical window and one for the sample, were waterjet cut from $\frac{1}{8}$ in 6061-T6 aluminum plate.

The recoater for the sample holder is a simple hand-operated single layer recoater. The body of the recoater is a machined block of 6061-T6 aluminum onto which the recoating blade is attached. The original blade for the recoater was machined out of 6061-T6 aluminum, but was later replaced with a precision ground section of hardened tool steel. Once the recoater blade is properly adjusted, the recoater functions by placing the assembly on top of the sample holder body with the lid removed. The

setup uses the machined surfaces on the top of the body and the bottom of the recoater block as a simple planar bearing interface.

Safety Enclosure

The safety enclosure provides a laser-absorbing housing to protect the user from errant laser radiation. It is composed of two halves that create a clamshell around the experimental setup. A model representation of the enclosure can be seen in figure 3-5. The front half of the clamshell was designed to be lifted off when the user needs to access the machine, and the back half of the clamshell contains all of the pass-throughs for the electrical connections and shielding gas. The back half is also fitted with a hinged door that serves as the mounting point for the electronics control board that contains the microcontroller and drive electronics for the setup.

(a) (b)

Figure 3-5: Model of the (a) front half and the (b) rear half of the safety enclosure.

The safety enclosure is constructed of an outer skeleton and a set of disposable panels mouted within that framework. The skeleton is constructed from extruded aluminum profile rails (8020 Inc. part #1010), and within this skeleton of rails,

panels constructed of $\frac{1}{8}$ in waterjet-cut 6061-T6 aluminum plate provide a light-tight housing. Interior surfaces of the safety enclosure were coated with matte black paint to absorb errant laser radiation and any gaps in the enclosure were sealed with aluminum laser tape (ThorLabs part #T205-2.0).

The safety enclosure also includes a series of microswitches that serve as safety interlocks. These microswitches are located to detect when the back panel is opened, when the from half of the enclosure is removed, or when the back half of the enclosure is removed. Connected in series with the interlock line on the laser, they prevent the laser from emitting when any portion of the enclosure is not properly secured in place. This feature is vital to user safety as it prevents inadvertent laser radiation exposure.

3.1.2 Optical System

The optical system encompasses all of the components necessary to generate and control the laser radiation necessary for melting the build material. The optical system can be broken down into two primary components: a fiber-coupled semiconductor diode laser and a modular objective. The laser radiation is coupled into a fiber optic cable which feeds from the laser, through the safety enclosure, and is terminated with a collimating objective. The collimating objective is integrated into a tube that allows for interchangeable focusing lenses, and is mounted to the moving carriage of the linear motion stage.

As mentioned previously, the intent of the LTS was to quickly create a test platform to conduct initial testing while construction of the full system was underway. In light of this, the laser system selected to power the platform was a DILAS Mini Diode Laser System (model 100401413)[123]. The particular unit used is an 808 nm, 50 W, continuous-wave, fiber-coupled semiconductor laser with a 400 µm output fiber. While the vast majority of commercial systems use 1064 nm fiber lasers, many metals have a higher absorbance at 808 nm as seen in figure 3-6, aluminum having significantly higher absorbance. Additionally, having a fiber coupled laser provides an easy means of routing the laser into the experimental setup, previous research has shown

that 50 W provides ample power for laboratory-level experiments [124][91], and, with a second-hand price of $500, the laser is a great low-cost option for researchers looking to fuse metal.

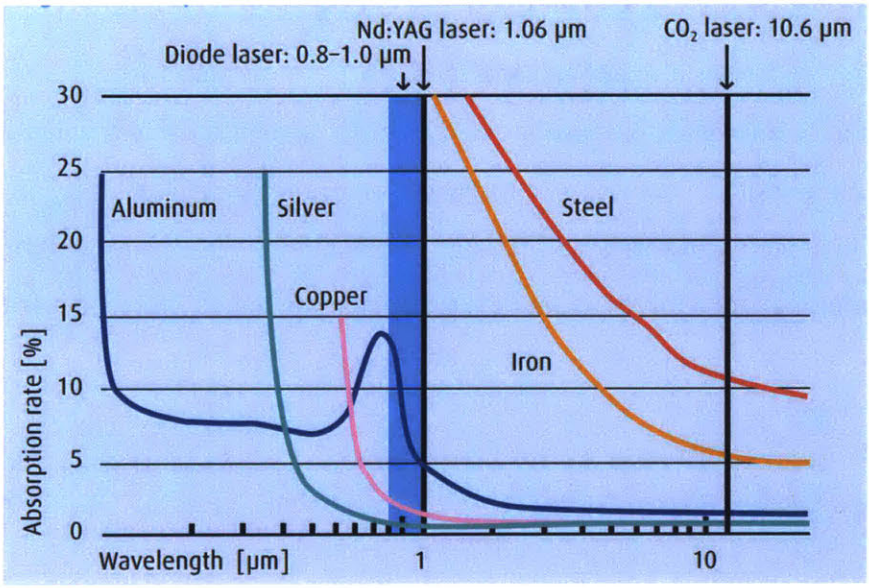

Figure 3-6: Optical absorption of various metals with notations for common laser frequencies showing the higher material absorbance for 808 nm lasers [48].

The one drawback of the laser is that it operates with multi-mode fiber with a 400 µm core and a 0.22 numerical aperture which emits light over a 25.4° window. The impact of this is that the collimated beam has large divergence which means that working distance for a given focused spot size is small. For the LTS, this meant limiting the system to a 250 µm focused spot for the working distances necessary to clear the objective over the sample holder.

To control the laser radiation, the energy is coupled into a fiber optic cable and routed to an objective where it is focused onto the sample. The fiber optic cable is a ThorLabs reinforced multi-mode fiber with a core diameter of 550 µm (part number MHP550L02). The fiber is terminated with a custom-aligned large diameter collimator (ThorLabs part F810SMA-Custom). The collimator is mounted to one end of a 1 in diameter optical tube, and on the other end is a screw-adjustable extension that holds a plano-convex objective lens. The object lens is interchangeable to control the focal length for different experimental requirements, but also sets a lower limit of the

spot size that can be generated. The two lenses used for the object were 1 in plano-convex lenses with focal lengths of 25.6 mm and 50.8 mm which gave minimum spot sized of 250 µm and 500 µm respectively. This entire objective assembly is screwed together with the linear motion carriage serving as the central receiver, as seen in figure 3-7.

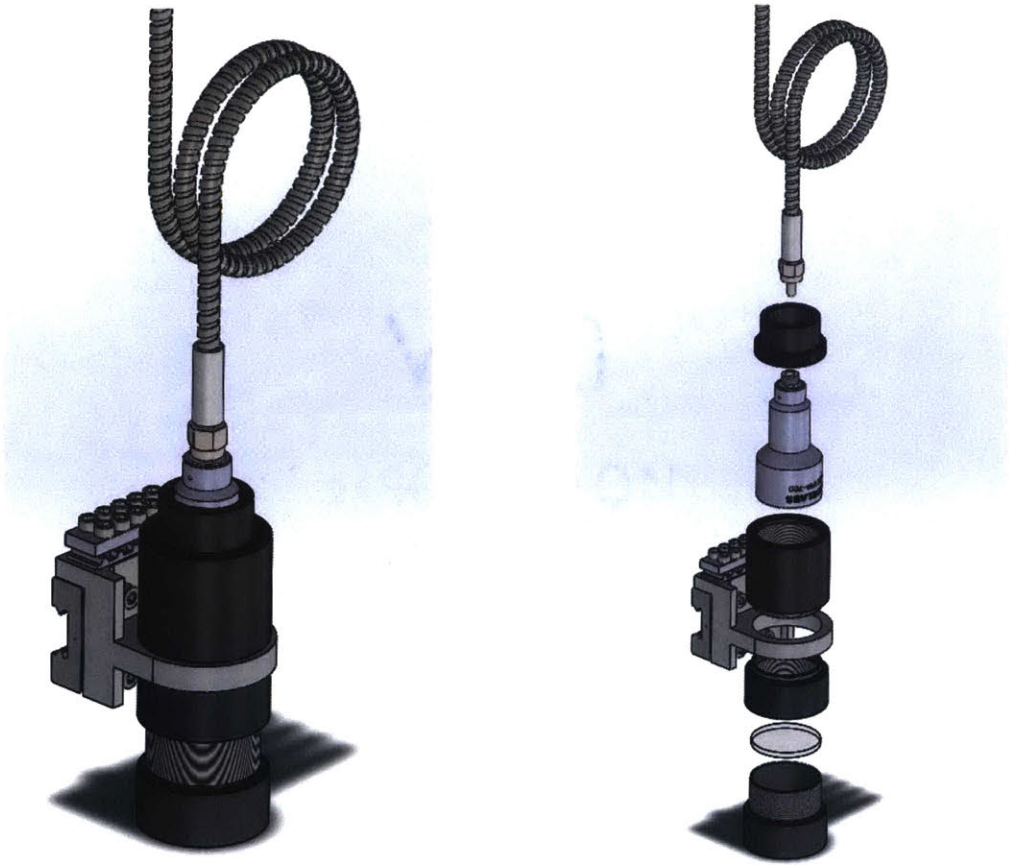

(a) (b)

Figure 3-7: Model of the collimator and focusing elements in the objective.

3.1.3 Electrical System

The electrical system encompasses all of the electrical hardware necessary to drive the stage and communicate with the host computer. The majority of the electrical system is located on the electronics control board mounted in the back of the enclosure. The microcontroller on this board communicates with the user and receives commands via a USB connection to a host computer. With experimental parameters set, it generates

step waveforms for the stepper motor driver and transmits them via discrete digital I/O pins. It can also communicate on the Controller Area Network (CAN) bus through an external CAN transceiver over an SPI connection. There is an additional set of discrete I/O used to control the laser as well as a pulse-width modulated pin fed through a low-pass filter to generate an analog voltage that sets the laser emission power. Additional components off the electronics control board in the form of microswitches serve both as limit switches for stage travel limit sensing as well as safety interlocks on the enclosure.

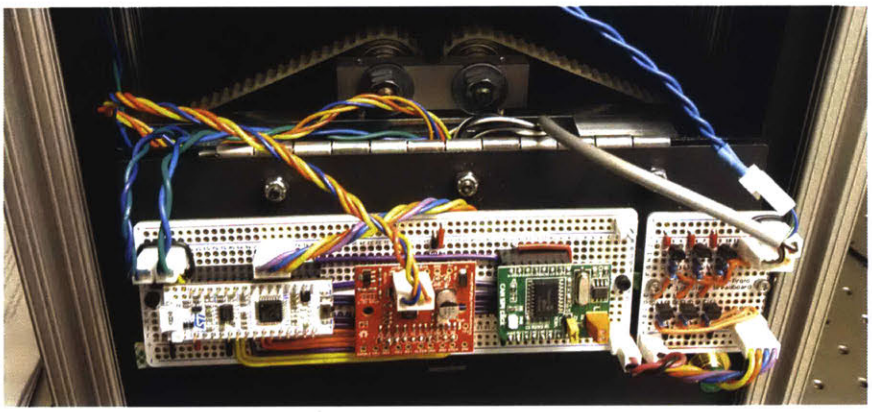

Figure 3-8: Control electronics board attached to the rear door of the LTS safety enclosure.

The electronics control board is comprised of three major components: microcontroller, stepper motor driver, and CAN transceiver module. The microcontroller is responsible for coordinating and controlling all of the systems within the LTS including communicating with the host computer via USB, generating the motor step profiles for the motor driver, and communicating via the CAN transceiver. The microcontroller board used is an ST Nucleo-F303K8 development board equipped with an STM32F303K8T6 microcontroller, powered by an ARM 32-bit Cortex-M4 core operating at 72 MHz [125]. One reason this microcontroller was selected is that it is compatible with the widely-popular Arduino [126] and mbed [127] integrated development environments which allow for fast, efficient coding, programming, and debugging. Interfacing with the microcontroller, the stepper motor driver is responsible for interpreting the step commands produced by the microcontroller and converting them

into motor drive currents to actuate the stepper motor. The driver used is the Sparkfun Electronics EasyDriver module which is equipped with a Allegro MicroSystems A3967 microstepping driver [128]. Alongside the stepper driver, the CAN transceiver board is responsible for connecting to and communication on the CAN bus. The CAN bus was originally designed to allow multiple experimental setups to communicate, but due to time constraints was reserved for future expansion. The board used is the MikroElektronika CAN SPI Click 5V which is built around the Microchip MCP2551 CAN transceiver [129].

3.1.4 Software Interface

The software system of the LTS incorporates all of the programming necessary to operate and control the motion of the carriage. The software system can be broken down into two major components: real-time software and non-real-time software. Real-time software and systems provide known timing within a given section of code, which means that it completes within a specific time frame regardless of system load, ensuring that events happen on a specific schedule. This is important for control of electromechanical systems, such as the stepper motor that drives the linear carriage, as the motor must be actuated at a specific timing interval to function properly. Non-real-time software is everything that falls outside of providing those constraints, such as multitasking operating systems which includes virtually all modern operating systems. The divide between real-time and non-real-time software corresponds with the separate software bundles running on the microcontroller, operating in hard real-time, and the host computer, operating in non-real-time.

Microcontroller Software

The real-time operation of the LTS occurs on the microcontroller which performs four key functions: serial communication, stepper motor control, digital input/output (IØ) control, and analog output control. The primary purpose of the microcontroller is to generate the digital waveforms necessary to control the stepper motor driver and

ultimately the stepper motor. The system uses a timer-based stepper motor control program derived from the AccelStepper library [130] that leverages on-the-fly generation of the stepper motor profiles to allow for smooth, continuous movement without the need for extensive pre-compiled arrays [131]. In order to communicate with the host computer, the microcontroller also uses an interrupt-based serial communication stack that passes basic ASCII text messages to and from the computer. The microcontroller is also responsible for operating the digital I/O lines that control the CAN transceiver and the laser. Along with the necessary digital I/O, the microcontroller also drives an analog output signal to provide the laser with a variable voltage that controls the laser emission power. Unfortunately, the microcontroller used does not poss a true digital-to-analog converter, so the system approximates the effect by using pulse-width modulation to vary the duty cycle of an output pin which is then run through a low-pass filter to remove the high frequency switching noise. All of this software was developed using mbed's cloud-based C/C++ compiler.

User Interface

The user interface for the LTS provides the user access to the control parameters of the system and to run experiments. While the majority of the control computation occurs on the microcontroller, a client running on a host computer allows the user to upload the desired operational parameters. This interface consists of a Python script that calls PyQt to generate a graphical user interface using Qt5 [132] [133] [134]. This interface provides the user with the controls to change the process parameters of the system such as the laser power, scan speed, and laser on-time. These options are bundled together and sent to the microcontroller via the USB connection. The software was developed using Sublime Text 3 [135], a plain-text editor.

3.1.5 Concept of Operation

The high-level operation of the LTS consists of five phases:

1. Prepare the sample

Figure 3-9: Python and Qt graphical user interface for controlling the LTS.

2. Load the sample into the machine
3. Program the experimental plan
4. Execute the experimental plan
5. Unload the sample

The sample is loaded into the sample holder by placing the sample inside of the sample holder and then securing it with the screw-down retaining plates. Once the sample is properly loaded in to the sample holder, the user then adjusts the height of the recoating blade to achieve the desired powder thickness. To adjust the blade, the user loosens the two clamp screws, places the appropriate thickness shim on top of the sample, and then places the blade carrier over the sample. By letting the blade rest on top of the shim, the clearance between the sample and the blade is set to the thickness of the shim. The user can then tighten the clamping screws to lock the blade, and the layer thickness, in place. With the recoater blade adjusted to the right height, the user can coat the build material onto the sample. Laying down the powder consists of pouring a small mound of the material along one edge of the sample, placing the adjusted recoating blade and carrier along that edge, and drawing the blade across the sample. This process spreads the powder across the surface of the sample at the thickness set by the gap between the blade and the sample. The user then removes the recoater assembly and closes the sample holder so that it can be loaded into the machine.

Once the sample is prepared and loaded, the experiment can be programmed and run. Loading the experimental parameters, such as laser power and scan speed, is done

using the GUI running on the host computer. After the user enters values, and the safety enclosure properly secured, the system the executes the experiment. Following the experiment, the user can then unload the sample holder from the machine, and the sample from the sample holder.

3.2 Galvanometer Platform

The Galvanometer Platform, or galvo system for short, is the central structure of the SLM system that houses the laser-steering galvanometer head and other optical elements. The test platform consists of a tower, on top of which is a boom that holds the optical components mounted to its end, a picture and model representation of the system can be seen in figures 3-10 and 3-11. One of the unique properties of this system is that the boom can be rotated in 60 deg intervals to allow the optical objective to cover multiple experimental setups without moving those experiments. The test platform can be divided into three major systems: the mechanical systems, electrical system, and the software system.

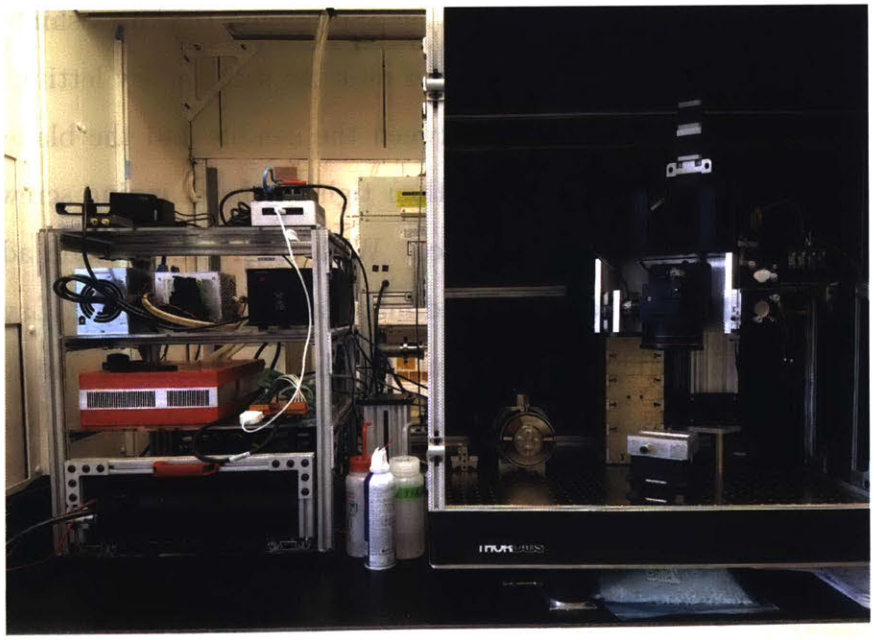

Figure 3-10: Galvanometer Platform in the lab; shelving unit with laser and power drawer on the left, optical tower located over the sample holder on the right.

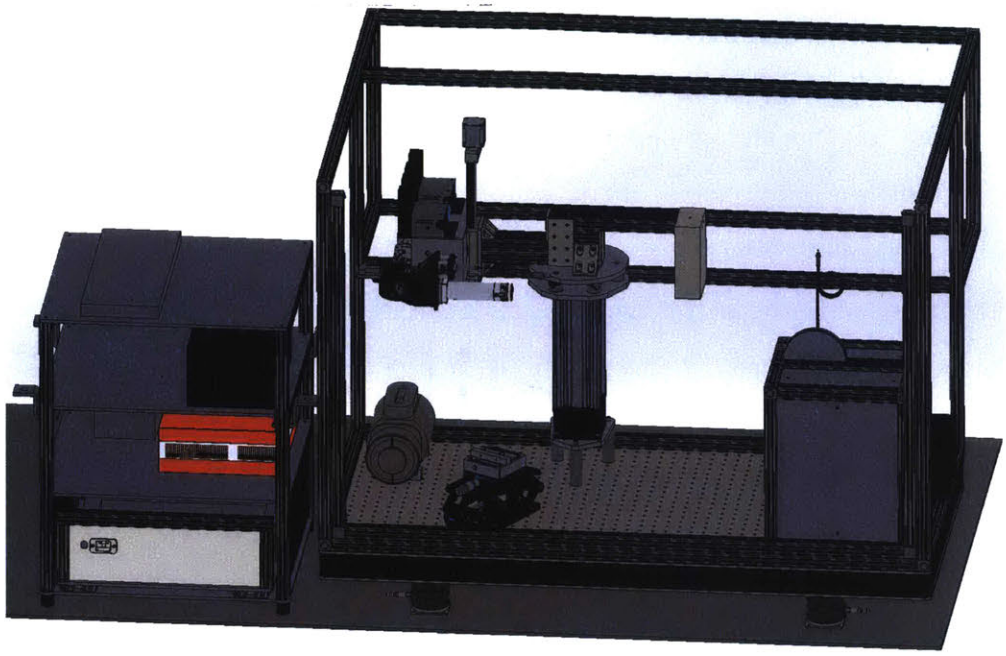

(a)

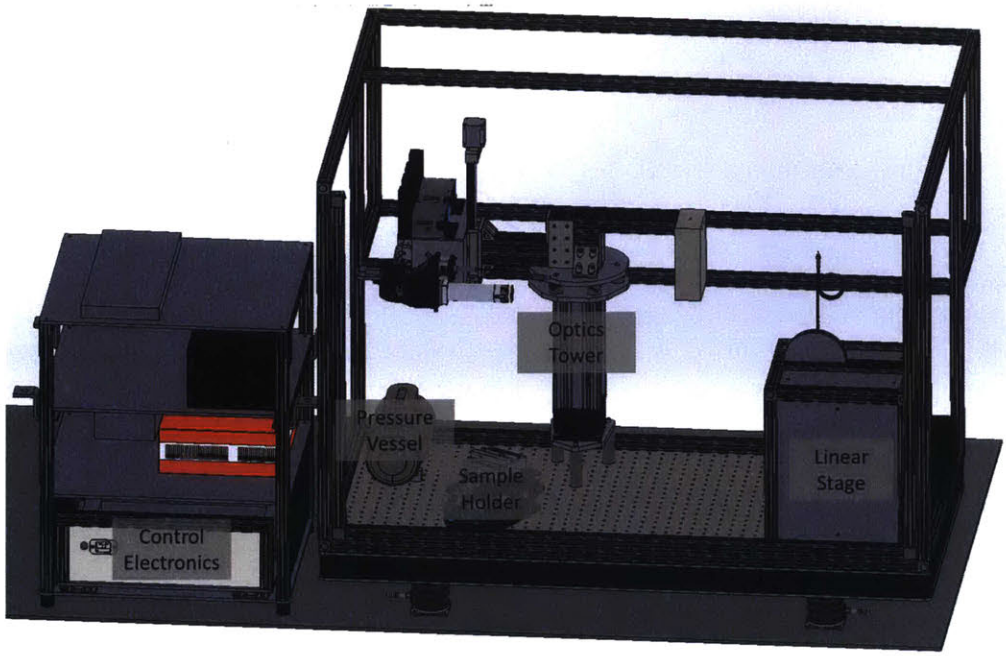

(b)

Figure 3-11: CAD model of (a) the bench top inside of the fume hood and (b) the assembly on top of the breadboard.

3.2.1 Design Considerations

Starting from a clean sheet of paper presented enormous opportunity for creativity. The primary design requirement of the system was to fuse a solid track in a 100 µm layer of 316L stainless steel powder with a 100 µm spot size. This requirement was chosen to to replicate the performance of commercial machines. Given the freedom from starting from the ground up, additional design specifications were imposed to shape the final system. The system should:

- Fit within a six foot wide, four foot deep, and four foot tall region.
- Run off of a standard 120VAC, 15A circuit.
- Be reconfigurable between multiple experimental setup.
- Contain at least two experimental areas.
- Reposition between experiments without the need for recalibration.
- Have at least two optical inputs and a means of selecting between them.
- Use an industry-standard 1064 nm fiber laser.
- Be able to scan at least $500 \frac{\text{mm}}{\text{s}}$.
- Contain a pressure vessel capable of reaching 1000 PSI.
- Have a multi-layer recoating system that fits within the pressure vessel.
- Lay down layers between 50 µm and 200 µm
- Interpret industry standard G-code for trajectories.
- Maximize the use of commercial-off-the-shelf components.

The performance requirement that shaped the final design of the machine the most was the need to reconfigure between multiple experimental setups without the need for recalibration. Repositioning without recalibration imposes a maximum repositioning error on the optical pipeline, but that error depends on the optics themselves.

As the focal range of the optics dictated the majority of the mechanical systems, that was where the design process began. The laser source was already dictated by the system requirements, so the beam steering and beam focusing mechanisms were next. The need to be reconfigurable and cover multiple experiments along with the constraint on scan speed ruled out the vast majority of beam steering systems save

for dual-axis galvanometers and other, more specialized systems. With commercial galvo systems and controllers readily available, that was chosen for the beam steering system. Coupled with that choice was the choice between a dynamic focusing system and an F-theta lens. While a dynamic focusing system presented a number of advantages, including the ability to focus on non-flat surfaces and provide on-the-fly spot size changes, it also came with significant mechanical complexity, increased software overhead, and a high cost. Given the simplicity and ease of implementation of the F-theta lens, it was chosen with provisions to be made in the mechanical design so a dynamic focus could be added at a later date.

One measure for quantifying the impact of optical shift is the areal power density:

$$\delta_{power} = \frac{P_{laser}}{A_{spot}} = \frac{P_{laser}}{\pi R_{spot}^2}$$

To limit the variation in experimental results, the change in areas power density needed to be kept below 5%, a factor based off of the industry standard of 10% deviation for lasers. Reconfiguring the equation above, we can find a relation between our permissible spot sizes and a percentage scaling factor λ, the initial radius $R_{spot,0}$, and the final radius R_{spot}:

$$R_{spot} = \sqrt{\lambda} R_{spot,0}$$

With a 100 µm spot size, this then gives:

$$\begin{aligned} for \quad & 95\%\delta_{power,0} \leq \delta_{power} \leq 105\%\delta_{power,0} \\ then \quad & 94.8\mu m \leq D_{spot} \leq 104.8\mu m \end{aligned}$$

which allows for approximately a $\pm$ 5 µm variation in spot diameter. For a Gaussian beam in free space, the Rayleigh number is [136]:

$$z_R = \frac{\pi w_0^2}{\lambda}$$

where λ is the wavelength and w_0 is the beam waist or focal spot size. With the assumption that the spot size is not too small, $w_0 \geq \frac{2\lambda}{\pi}$, this can be used to calculate the spot size some distance z from the focal point [137]:

$$R = R_0\sqrt{1 + \left(\frac{z}{z_R}\right)^2}$$

which can then be rearranged to

$$z_R = \sqrt{\frac{R}{R_0} - 1}$$

With an F-theta lens that has a 160 mm effective focal length, the depth of focus is then 0.24 mm. From a mechanical design perspective, this means that the optical head positioning must be repeatable to within ± 0.120 mm.

3.2.2 Mechanical System

The mechanical portion of the galvo system encompasses the physical structure that holds all of the relevant components together and allows for repeatable placement of the boom. While the mechanical structure of the galvo system performs all of the same functions as its commercial counterparts, the implementation differs significantly due to the functional requirements.

The four primary subsystems that constitute the mechanical system are the optical tower, the tower boom, the optical head, and the safety enclosure. The optical head, which houses the beam-steering galvanometer mirrors and focusing optics, is affixed to the end of the tower boom. The tower boom serves as an extension to place the optical head away from the optical tower, and as the coupler between the optical head and the optical tower. The optical tower tower supports the optical head and anchors it to the optical breadboard atop of which the entire system is constructed. Wrapped around these components, the safety enclosure functions as a barrier to any stray laser radiation, protecting the researcher and the environment.

One of the functional requirements for the galvo system is that it be flexible and reconfigurable to accommodate changing research needs. Given that the original location for the system was in a large fume hood with ample room, it was clear that the system needed to allow for multiple experimental setups to use all of the space provided. To maximize the use of the area, I chose to design the system as a central support tower with the optics located on the end of a boom that could be repositioned over a number of different experimental setups. To achieve this, the optical tower houses a set of internal actuators designed to lift and rotate the optical head so that it can be repositioned. By allowing the optical head to be repositioned, multiple experimental setups can be accessed by the laser without moving those setups.

Optical Tower

The optical tower serves as the mounting point for the tower boom, anchoring it and the optical head to the optical breadboard, and is composed of the support column and internal bearing cart. In addition to serving as a simple mechanical support, the optical tower also houses the actuators necessary to reposition the optical head over multiple experimental setups. Pictures of the optical tower CAD model can be seen in figure 3-12

I began the design of the optical tower by selecting the the coupling system used to mate the tower boom to the support column. Due to the narrow depth of focus for the focusing optics, and by extension high sensitivity to misalignment, the means by which the column and boom are coupled must have a high level of repeatability so that system does not have to be refocused every time it is moved. In order to make the positioning of the tower boom and optical head repeatable relative to the optical tower, the two are mated together with a kinematic coupling. A kinematic coupling consists of three vee grooves, often spaced at 120° intervals around a circle, and a set of three spheres that mate with the three vee grooves. These couplings follow the principles of exact constraint design in which the number of contact points matches the number of degrees of freedom that are to be constrained. In the case of a kinematic mount, there are six degrees of freedom: translation in x, y, and z as well

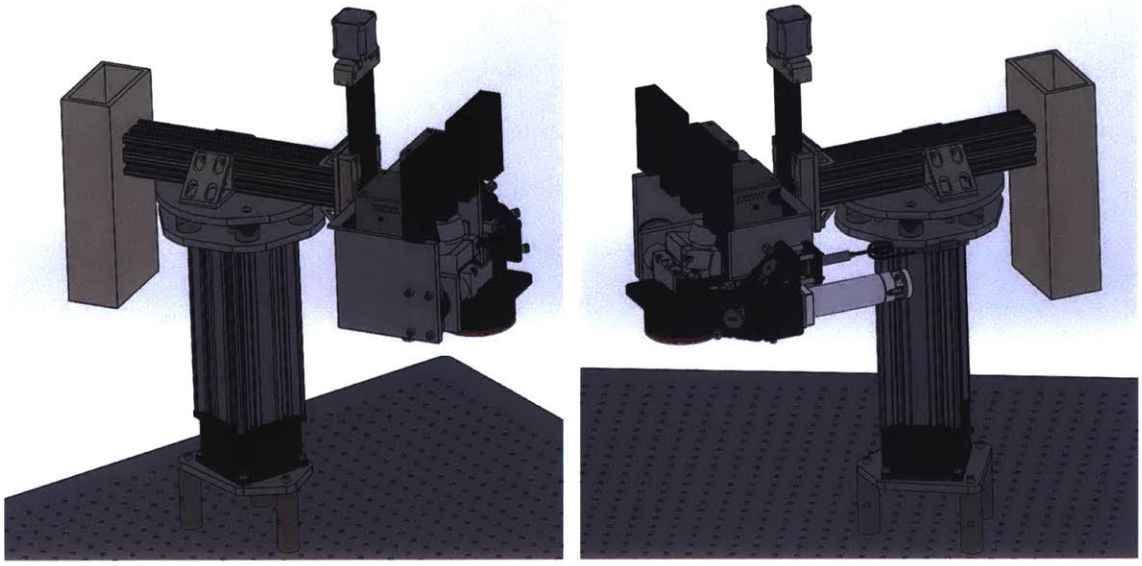

(a) (b)

Figure 3-12: Model view of the optical tower.

as rotation about each one of those axes, and six contact points, two for each ball-vee interface.

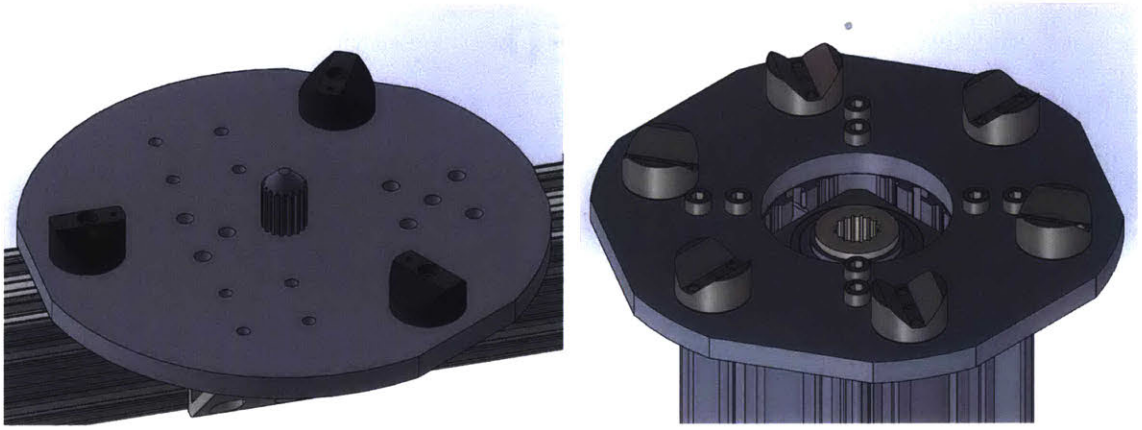

(a) (b)

Figure 3-13: Top and bottom views of the optical tower model.

The next item to address in designing the system is how the boom engages/disengages from the kinematic mount and how it rotates. One complicating factor in the actuation is that, in order to access the largest workspace, the tower boom needs to rotate 360 deg. To achieve complete rotation, the tower boom had to be mounted on the end of an extension-style linear actuator. This brought its own complications in

that, with a bottom-supported boom, the coupling system and linear actuator would either need a significant amount of torsional rigidity and preload to support the cantilevered weight, or a counterweight would have to be added to balance the boom at the linear actuator/coupling connection point. In comparing these approaches, the counterweight provides two major benefits in that it not only reduces the torques generated at the mounting interface, but also provides balance and additional weight for preloading the kinematic mount. Given the trade offs of each approach, the counterweight system was selected, particularly because it eliminated the torques and the coupling.

While there are commercial-off-the-shelf linear actuators available that could lift the tower boom and optical head, the optical tower actuation was implemented using a custom linear rotatory actuator. The motivator for this was the fact that even with a COTS linear actuator, the tower would still need structural support, some form of linear bearing, and a means of rotating the tower boom on top of the linear actuator. Combined with the large size of most commercial solutions, it was more practical and space-efficient to implement a custom solution. This decision drove the selection of the large-diameter extruded aluminum profile rail as it serves as both the mechanical structure of the tower and the housing/bearing surface for the custom linear actuator. With the external dimensions constrained, it was then a matter of selecting the necessary motors and designing a cart to house the components and slide within the profile rail.

Support Column The support column portion of the optical tower includes all of the static components necessary to support the tower boom and optical head. This structure, seen in figure 3-14, provides the mechanical rigidity and repeatability necessary to accurately reposition the optics over the various experimental setups.

From the bottom up, the support column construction starts with a set of three stainless steel posts used to set the height of the top of the tower (ThorLabs part P3). On top of these posts, an adapter waterjet cut from a $\frac{3}{8}$ in 6061-T6 aluminum plate interfaces them to a mounting box adapter (ThorLabs part XT95B50) for large-profile

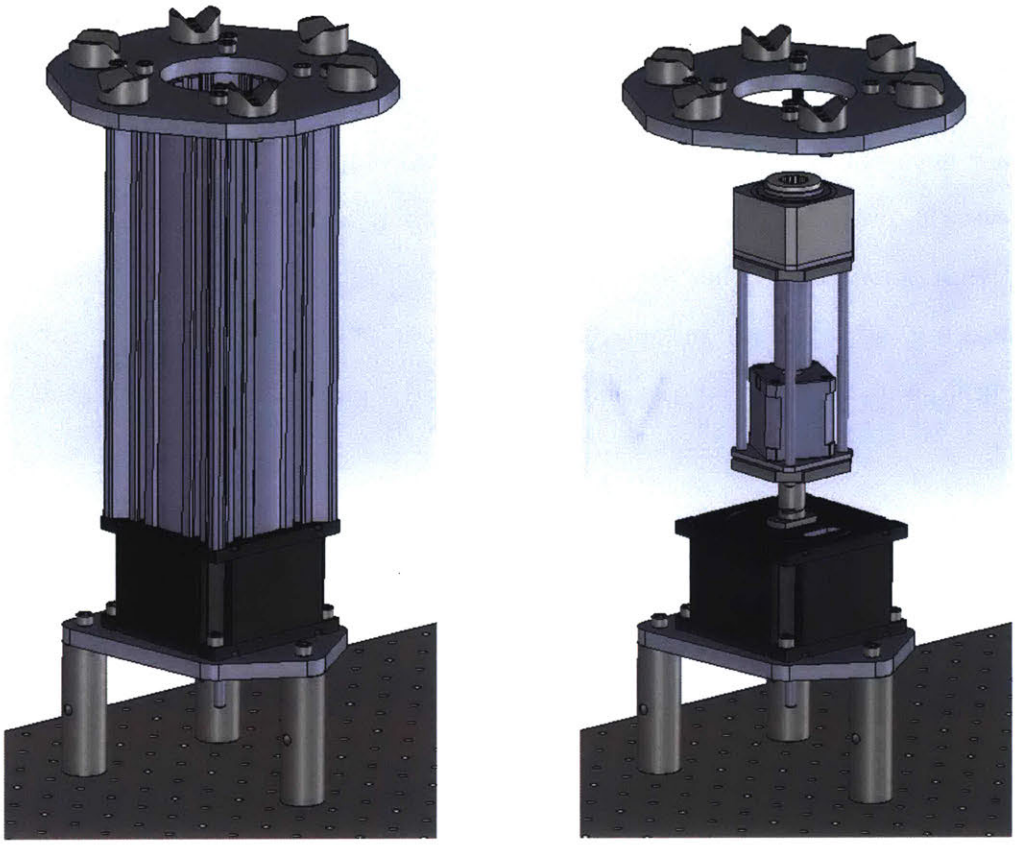

(a) (b)

Figure 3-14: Model view of the optical tower (a) with and (b) without the central extrusion to show the location of the bearing cart.

aluminum extrusions (ThorLabs 95 mm series). This adapter box then connects to a 250 mm long section of ThorLab's 95 mm aluminum profile extrusion (ThorLabs part XT95-250). Mounted on the other end of the aluminum extrusion is another waterjet cut $\frac{3}{8}$ in 6061-T6 aluminum adapter plate. The top adapter plate serves as a mounting point for a set of six hardened, stainless steel vee blocks (Bal-Tec part VB-75-SM) that constitute half of the kinematic mount that affixes the optical head and boom to the support column.

Bearing Cart Inside of the aluminum profile extrusion sits the bearing cart assembly that actuates the tower boom. The bearing cart is an assembly consisting of two motors bundled together with a structure that serves as both a mounting system and the bearing surface. The purpose of the bearing cart is to provide controlled lift and

rotation of the tower boom and attached optics head so that it can be repositioned over various experimental setups. Figure 3-15 shows the fabricated system.

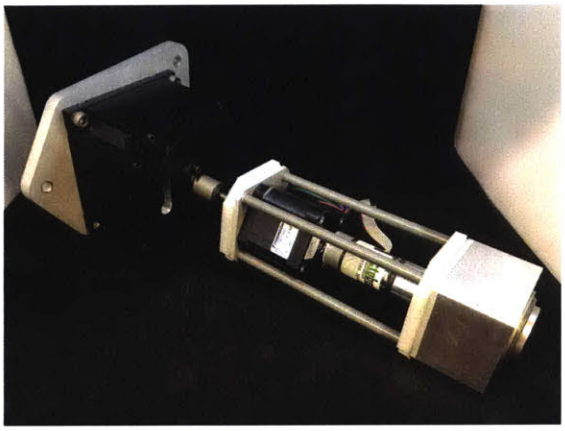

(a)

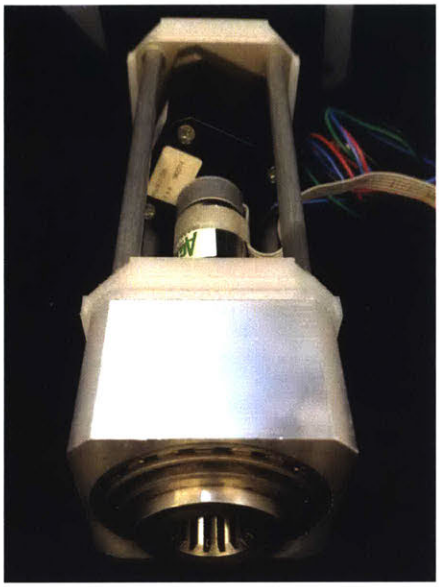

(b)

Figure 3-15: Fabricated bearing cart system with a close-up of the bearing block.

At one end of the bearing cart a machined block of 6061-T6 aluminum serves as the chassis that houses and connects all of the components. Located within this block, an angular contact roller bearing (McMaster Carr part #5709K18) carries the load from lifting the tower boom and allows it to rotate. The tower boom is coupled to the bearing cart using a section of splined shaft (SDP-SI part A-1Y25-62502) which slides into a splined collar (SDP-SI part A-1C26-62510) machined to fit within the angular contact bearing. To retain the bearing assembly and splined collar, a wave spring (McMaster Carr part #9714K116) is used to provide preload between a snap-ring (McMaster Carr part #97633A300) and a needle roller thrust bearing (McMaster Carr part #5909K36) resting against a hardened steel washer (McMaster Carr part #5909K49). Extending out from the chassis block is a set of four precision aluminum shafts (McMaster Carr part #5911K41) that function as attachment points for the motors.

Two motors provide the actuating power for driving the cart along the profile rail as well as rotating the tower boom once it is lifted off of the kinematic mount. Both

motors are attached to the bearing cart using waterjet cut $\frac{1}{8}$ in 6061-T6 aluminum plates. Sandwiched between these plates at are a pair of waterjet cut $\frac{1}{4}$ in ultra high molecular weight polyethylene pieces are used as the bearing surfaces between the bearing cart and the aluminum extrusion. The solid model of bearing cart and a cutaway views of the internals can be seen in figure 3-16.

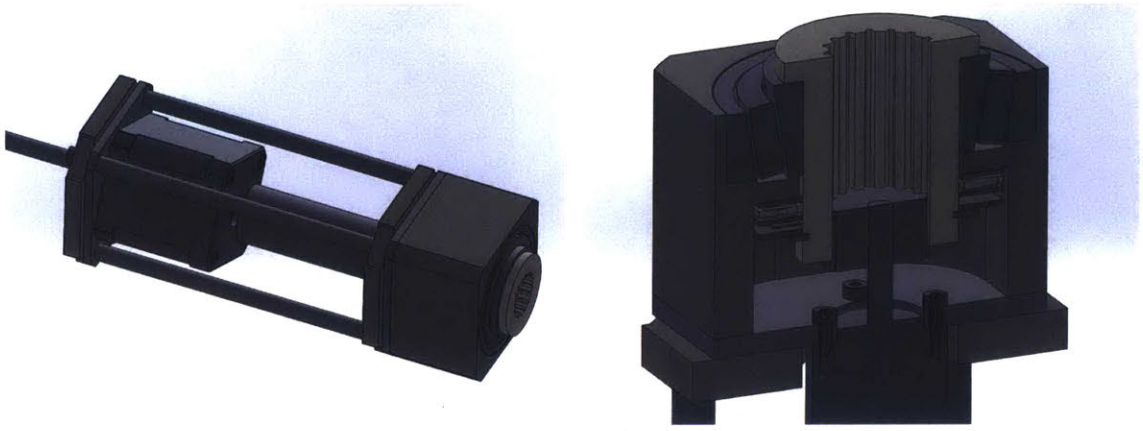

(a) (b)

Figure 3-16: Model of (a) the bearing cart and (b) a cutaway of the bearing block showing the internal construction.

The lift actuator consists of a Thompson Linear integrated leadscrew stepper motor (Thompson part ML17B150S). This motor is triple-stack a NEMA 17 stepper motor with a 0.250 in pitch ACME leadscrew integrated into the rotor. The corresponding ACME nut is fixed to the top panel of the box adapter located at the bottom of the aluminum extrusion. By rotating this motor, the leadscrew applies a force against the fixed ACME nut and can either raise or lower the bearing cart, as well as the tower boom, relative to the support column. The incremental motion of the stepper motor means that the tower does not use feedback when raising/lower the boom. However, the system does require an initial homing sequence when it is started from a power-off state.

Rotation of the tower boom is provided by planetary gearhead motor with an integrated encoder (Pololu part #638288). The rotation motor is coupled to the tower boom through the splined nut mentioned above by a section of splined shaft connected to the output shaft of the motor. Once the kinematic mount has been

lifted apart by the lift motor, the rotation motor can be used to spin the tower boom to a new position of the kinematic mount. Integrated into the rotation motor is a quadrature encoder that provides incremental motion feedback. Like the lift stage, the rotation stage must be homed on power-on in order to properly track its location.

Tower Boom

The tower boom is the mounting structure that extends outwards from the support column onto which the optical head is mounted. More specifically, the tower boom serves as the mechanical support structure that connects the optical head and corresponding counterweight to the kinematic mount as well as the bearing cart that is used to actuate the assembly.

As described in section 3.2.2, the kinematic mounting system is used to accurately and repeatably move the tower boom and optical head between mounting locations. To mate with the vee blocks located in the optical tower, the bottom of the tower boom interface plate is fitted with a set of three canoespheres (Bal-Tec part CS-1125-CPM). A canoesphere is a pair of sections from a large diameter sphere carved into a mounting surface, in this case the canoespheres used have surfaces with a 1 meter diameter curvature. Part of the motivation for using the canoespheres in combination with the vee blocks is that the large radius of curvature, far larger than any traditional ball could provide, increases the surface contact area of the Hertzian force, and therefore increases the load capacity of the coupling. Additionally, the repeatability of these canoesphere has been show to be 60 µm or better [138], which exceeds the repeatability requirements mentions in section 3.2.1.

The core of the tower boom is a waterjet cut $\frac{3}{8}$ in 6061-T6 aluminum plate onto which the canoesphere are mounted. This plate also serves as the mounting point for the section of splined shaft used to rotated the tower boom as well as the section of 2 in square aluminum extrusion (8020 Inc. part #2020) onto which the optical head and counterweight are attached. At one end of the tower boom, a set of waterjet cut $\frac{3}{8}$ in 6061-T6 aluminum plates form a box that is used to hold lead weights to act as the counterweight for the optical head. At the other end of the tower boom

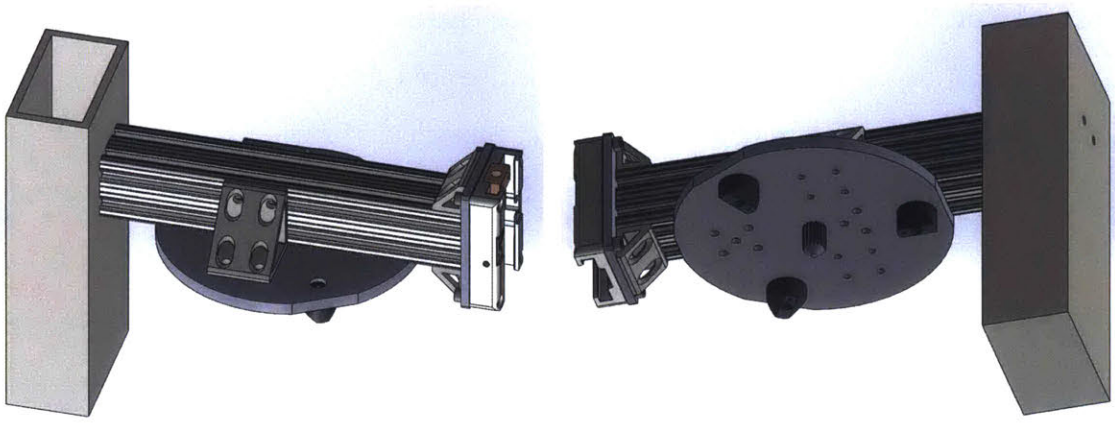

(a) (b)

Figure 3-17: Model of the assembled tower boom.

the carriage portion of a linear actuator (PBC Linear part UGA040D-A10) is bolted on using a waterjet cut adapter plate. This linear actuator serves as the connection point between the tower boom and the optical head, and allows the optical head to be adjusted vertically to allow for focusing. The reason the carriage is attached to the tower boom, instead of the rail which is normally the stationary component, is that by attaching the carriage, the rail travels with the optical head and does not extend past the head regardless of where it is positioned.

Optical Head

The optical head is a three-axis adjustable mechanical housing attached to the end of the boom arm. The purpose of the optical head is to provide the mechanical structure necessary to support the laser fiber-optic cable and other optical pipeline components as well as allow for the adjustment. To provide the ability to level and focus the objective's focal plane, the galvanometer and objective can be adjusted in roll, pitch, and height. The structure of the optical head consists of a pair of large extruded 6061-T6 aluminum angle sections fastened to the rail-portion of the focus linear actuator mentioned in section 3.2.2. A model representation of the optical head can be seen in figure 3-18.

Attached to one of angle profiles is a manual rotation stage with an intermediate, smaller section of angle profile extrusion. This smaller section also has its own man-

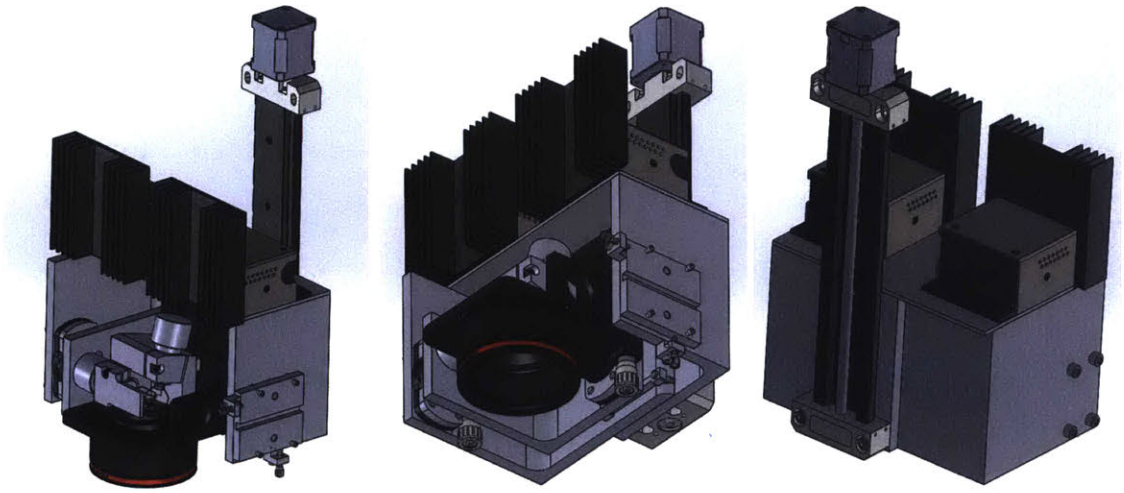

(a) (b) (c)

Figure 3-18: Model of optical head assembly, optical pipeline removed for clarity.

ual rotation stage positioned with the axis orthogonal to the first. Coupled together these two rotation stages provide roll and pitch adjustment to the beam-steering galvanometer assembly attached to the intermediate angle profile's rotation stage. Attached to the outer, larger angle profile is the beam selection assembly, discussed further in section 3.2.5. This assembly is built on a custom machined 6061-T6 aluminum block and sub-plate that allows for the planar adjustment of the subassembly's exit aperture relative to the input aperture of the primary galvanometer mirror.

Safety Enclosure

The safety enclosure is a housing containing the entire system designed to prevent any laser radiation from escaping the experimental setup. Due to the high-power laser radiation involved in SLM processing, it is vitally important to shield the researcher from inadvertent exposure. The level of power used in this setup is more than capable of rapidly burning flesh and blinding someone should they be exposed to specular reflections, let alone the beam itself.

The enclosure is constructed using 1 in square extruded aluminum T-slot profile rails (8020 Inc. part #1010) and $\frac{1}{8}$ in 6061-T6 aluminum panels. The interior of the enclosure was painted matte black to increase the absorbance of stray laser radiation.

To provide access, the front of the enclosure is fitted with a bi-fold door, and there are a number of ports punched through the side to allow cables to pass through. To ensure stray laser radiation cannot escape through gaps in the panels or through the bulkhead passthroughs, all openings are patched with adhesive-backed, matte black aluminum foil (ThorLabs part T205-2.0).

In operation, the system functions by either absorbing or reflecting the incident laser radiation. When low-power laser radiation strikes the panels or frame, the matte black coating absorbs the energy and converts it to thermal energy which is then dissipated through radiative, convective, and conductive heat transfer to the surroundings. As the incident power increases, the coating will heat up, and eventually ablate off of the enclosure surface. When this happens, the aluminum substrate is exposed, and the laser radiation is reflected to another portion of the enclosure due to the much lower absorption of aluminum. While the enclosure is not capable of handling sustained, direct exposure to the focused laser beam, the focal plane of the laser is constrained to the optical breadboard to prevent that from occurring.

The original design for the safety enclosure included, like the enclosure for the linear test platform, safety interlocks to disable the laser output while the enclosure is open. However, due to the necessity of being able to activate the laser for focusing and alignment, the safety interlocks were removed. In order to address the safety concerns of having the enclosure open while the laser is active, we implemented rigorous administrative safety controls and proper personal protective equipment to mitigate accidental operator exposure.

3.2.3 Optical System

Operating on top of the mechanical system, the optical system is responsible for generating and controlling the laser energy necessary to sinter or melt the powdered build material. Precise control and positioning of the laser beam is essential to the selective laser sintering/melting process. The optical system consists of three major components: the source of the laser energy, the optical components needed to guide it to the experimental setup, and a system to properly level and focus the system.

3.2.4 Laser Source

The laser source is the component responsible for generating the laser radiation necessary to sinter/melt the powdered build material. The module at the heart of this setup is a 1064 nm Nd:YAG fiber laser produced by SPI Lasers (G4-series 70W EP-Z). This model is the air-cooled version, and can produce 70 W in continuous-wave (CW) mode, but can also operate in pulsed mode and will generate up to 15 kW peak power. The laser radiation is coupled into the experimental setup via an 8 mm collimator (SPI part BEC F75) attached to the end of the single-mode fiber. The laser is controlled via a series of digital, analog, and serial interfaces, which are discussed further in section 3.2.8. A picture of the laser can be seen in figure 3-19.

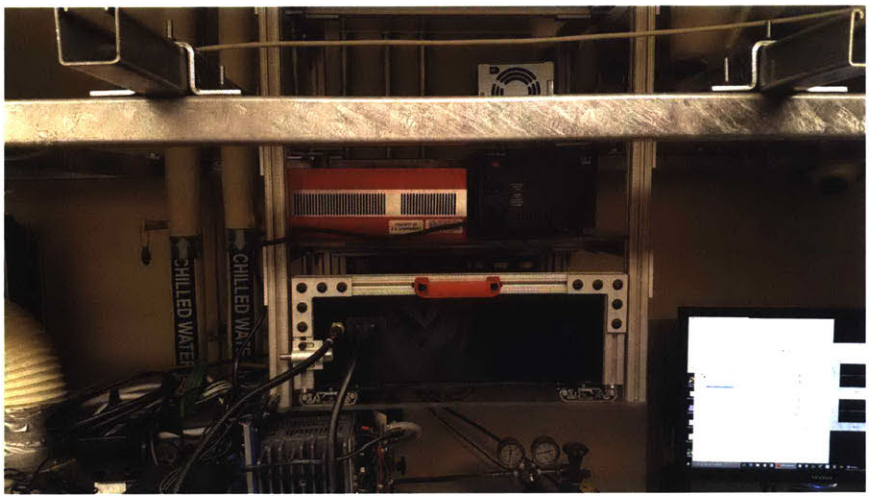

Figure 3-19: Electronics rack showing the red SPI Lasers Nd:YAG fiber laser used in the experimental setup next to one of the power supplies.

3.2.5 Optical Pipeline

The optical pipeline consists of all of the components that the laser radiation passes through or reflects off in the process of reaching the desired experimental setup. The only portion of the optical pipeline not integrated with the optical head is the laser itself. The laser used, discussed in section 3.2.4, is a fiber-coupled unit which transmits the laser radiation produced via a fiber-optic cable to the optical head. The optics portion of the optical head consists of the beam-steering galvanometer

mirrors and objective lens as well as an assembly used to select the laser source for the experiment. A model representation of this setup can been seen in figure 3-20.

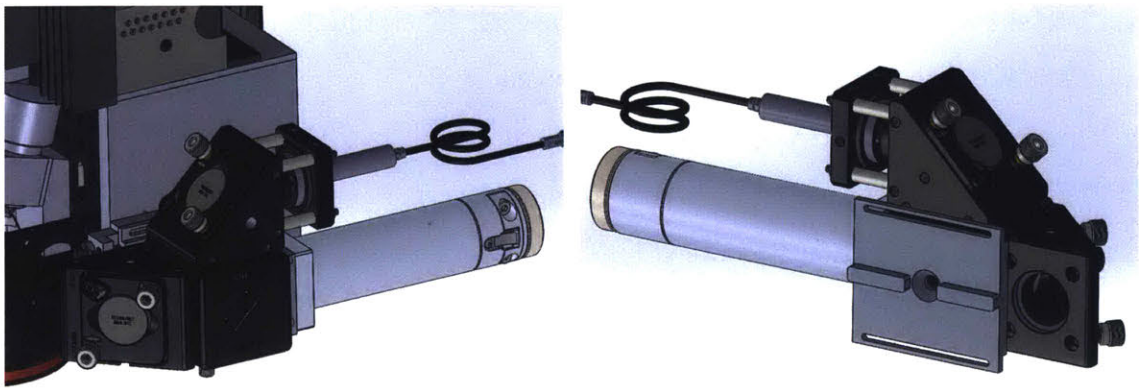

(a) (b)

Figure 3-20: Model of optical head assembly, emphasizing the optical pipeline components.

Exiting from the laser fiber, the beam first passes through a collimator and beam-selection assembly. The collimator, described above, converts the diverging laser radiation exiting the end of the fiber into a collimated beam. The collimated beam is then passed through a prism holder and reflects off a mirror into the aperture of the galvanometer head assembly. The prism holder is empty in normal use (when the integrated laser is used), but a mirrored prism can be inserted into the holder to direct the secondary input port above the collimator to the galvanometer aperture. This allows for other light sources to be integrated into the system, such as a UV laser for polymer curing, which offers greater experimental flexibility.

At the core of the optical pipeline is a beam-steering galvanometer system used to point the focused laser spot. This integrated system (Thorlabs part GVS012) contains a pair of orthogonal galvanometer actuators with mirrors attached to the end of their shafts. Once the beam has passed through the laser selection block, it reflects off an angled mirror and strikes the first galvanometer mirror, is then reflected onto the second galvanometer mirror, and finally passes through the objective lens. By controlling the angle of the mirrors, the focal point of the beam can be steered around the working surface. From an implementation perspective, these actuators

transform an analog voltage signal into an angular displacement of each mirror. This approach has an advantage over other methods of positioning the focal point, such as an xy-gantry, in that the mirrors are small and light, allowing for rapid acceleration, fast scan speeds, and short step response times.

Once reflected off of the galvanometer mirrors, the beam then passes through an F-theta objective lens (ThorLabs part FTH160-1064), which is an integrated stack of three separate lenses. Entering the lens, the beam is collimated, so it must first be focused to a point. However, due to the rotation of the galvanometer mirrors, the focal surface for a standard lens would be a spherical shell, so the focal surface must be flattened to a planar surface. Lastly, due to the movement of the galvanometer mirrors, scan surface is shaped like an hourglass, and must be barrel-distorted to transform that into a square region. All three of these functions are performed via the F-theta objective lens.

3.2.6 Focusing Camera

One challenge in using the system with multiple experimental setups is that the laser must be leveled and focused for each setup. While the repeatability of the kinematic mount means that the system returns to position well within the focus requirements, it still must be performed at least once for every experimental setup. To focus the camera, we chose to use a high-resolution, IR sensitive CMOS camera. The focusing camera assembly consists of the focusing camera itself as well as a precisely machined stand that provides a know standoff distance between the CMOS sensor of the camera and the surface on top of which the assembly rests. A picture of the focusing camera assembly can be seen in figure 3-21.

To focus the laser, the camera assembly is positioned under the objective of the F-theta lens, and the optical head is moved into roughly the correct position based off the manufacturer's provided working distance. With the safety enclosure closed, the laser is powered on and the control gate is opened with the output power set to 0%. Even with the output power set to 0%, there is enough pump diode leakage to illuminate a spot on the camera's sensor. Using the manufacturers camera software

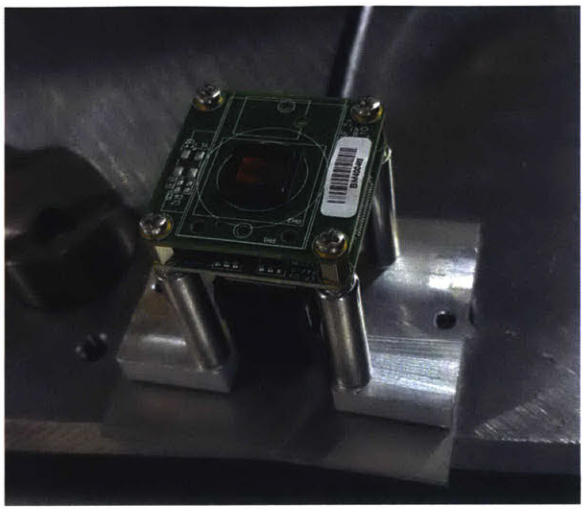

Figure 3-21: Focusing camera assembly.

to inspect the size of the spot, the optical head can then be adjusted up and down to achieve the desired spot size. Once the desired spot size is reached, the focusing camera assembly is removed, and the optical head is lowered by the height of the focusing camera.

3.2.7 Electrical System

The electrical system encompasses all of the major components responsible for providing power and control signals for the system. The two primary section are power regulation and distribution to drive the setup, and control signal generation for operation, both analog and digital.

Power Distribution

The power distribution system provides the appropriate voltages to power the various subsystems, and consists of a series of power supplies coupled with a routing and distribution drawer. In addition to AC power, the system includes three separate AC to DC power supplies. The first discrete power supply is the AC to DC module that SPI Lasers provided to power the laser. This module is only used to power the laser due to the high power demands of the laser. The second discrete power supply is a Delta Electronics CliQ II DIN rail power supply (part DRP024V480W1BN) that

puts out 24 V and is rated at 480 W. This power supply is used to drive all of the miscellaneous devices as well as power the actuators for the tower and focus system. Lastly, to drive the galvanometer head, a ThorLabs GPS011 power supply provides twin-rail ultra-low-noise DC voltage. The discrete nature of the galvanometer power supply is important as the galvanometers are sensitive to power rail noise and suffer decreased accuracy when a significant amount of noise is present.

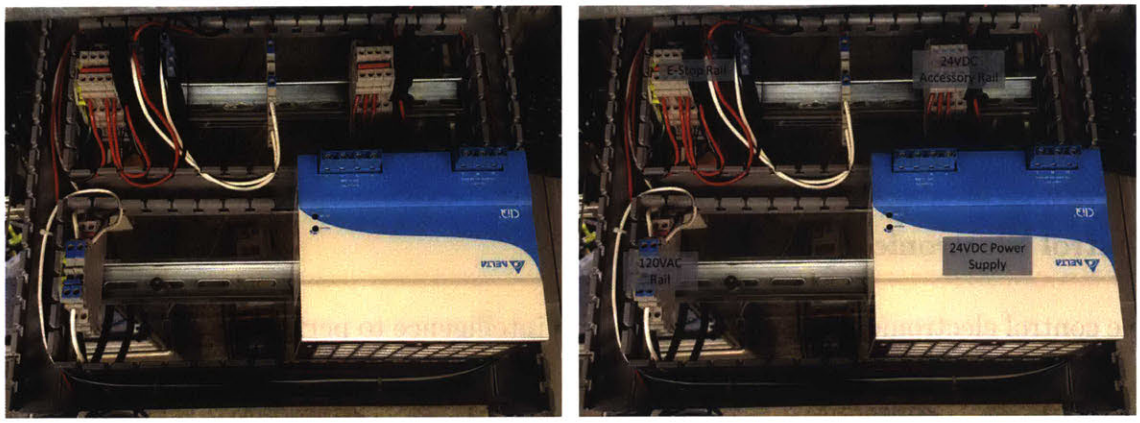

(a) (b)

Figure 3-22: Picture of the power electronics drawer with an annotated diagram.

Power enters the system through the power control pendant. The pendant contains the system power disconnect switch, an emergency stop (e-stop) button, and a pair of IEC-320-C15 AC connectors. The AC connectors are used to route power in from the wall, through the power disconnect switch, and out to the power drawer. The power disconnect switch is a high-current rated contactor (McMaster part #7277K51) used to connect or disconnect power from the system. On a separate line, the e-stop (Omron part A22E-M) is linked to the power drawer to allow for rapid disabling of the laser and other systems that need to quickly be shut down in the event of an emergency.

In order to organize and route all of the necessary power connections, the shelving unit has a power draw integrated into it. The power drawer is a slide-mounted box that contains DIN rails that allow for modular system construction and ease of reconfiguration and expansion. Inside there are four main power rails that drive the system. The AC power rail is a 120 V bus that provides AC power to the other power

supplies and is fed from the power control pendant. The accessory power rail is a 24 V DC bus that is fed off of Delta Electronics power supply. This power rail is used to power the majority of the DC-powered components in the system including the e-stop on the pendant, and is fed through fuse blocks to protect the system. There is an additional DC power rail fed off the laser power supply. The input line for this power rail is passed through a relay connected to the e-stop so that the user can quickly de-energize the laser if needed. The last rail is formed by the e-stop input, which allows for the addition of other relays besides the one for the laser should they be needed.

Control Electronics

The control electronics provide the embedded intelligence to perform real-time control on the system's hardware. There are three primary control subsystems: waveform control, focus head control, and tower control.

At the core of the experimental setup is the waveform control system. This subsystem is responsible for producing the analog voltage waveforms that control both axes of the galvanometer head as well as the laser output power. In order to create complex, precise patterns for the SLM process, the waveform control system must produce high-precision and high-frequency analog waveforms. To meet this need, the experimental setup is outfitted with a National Instruments CompactRIO (cRIO) model 9076. The cRIO provides an embedded computer, field programmable gate array (FPGA), and modular interface system for attaching different sensor modules. This combinations of elements provides the necessary bridge to convert the discrete digital values of the synthesized control waveform into continuous analog waveforms in real-time.

The cRIO used was outfitted with the short chassis that allowed four cRIO modules to be connected. The first bay contains a National Instruments 9205 digital-to-analog (DAC) converter module. The DAC module is what converts the discrete digital waveform values into analog signals to drive the galvanometer head and laser. The second bay contains a National Instruments 9263 analog-to-digital (ADC) con-

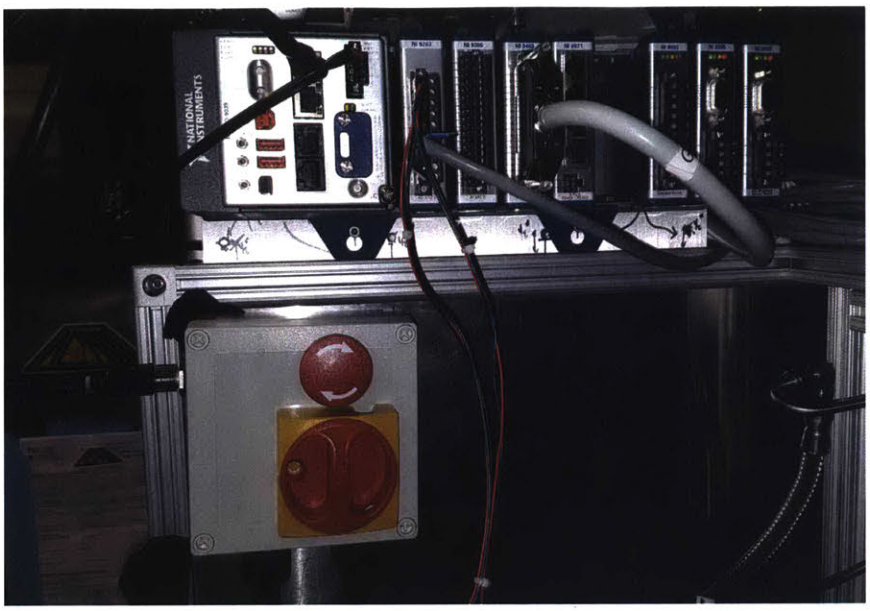

Figure 3-23: cRIO mounted to the side of the laser safety enclosure with the power pendant mounted below it.

verter module. This module is responsible for converting analog inputs into digital values for monitoring and control of the system. The Third bay contains a National Instruments 9403 general purpose input/output (GPIO) module. The GPIO provides the necessary digital control signals to engage the laser as well as control other peripheral components. The last module in the fourth bay is a National Instruments 9871 serial interface module that allows serial control from within LabVIEW. All of these components, and the chassis itself, were powered off of the 24 V accessory rail.

To drive the focus motor and the actuators in the tower, two additional control boards were added to the system. The focus motor controller is nearly identical to the control electronics board developed for the Linear Translation Stage described in section 3.1.3. The tower control board is identical to the LTS control electronics board as well, but has the addition of a brushed DC motor driver module (Pololu part 1213). This board uses the stepper motor driver board to control the lift of the tower, and then uses the brushed DC motor board to control the rotation of the tower. Tracking the rotational orientation of the tower is done through a rotary encoder coupled to the rotation axis. To house the control boards, an enclosure was laser-cut from acrylic. This enclosure also contains an LCD display and numeric touchpad for control of the

focus system as well as a 4-way button set for control of the tower position. Both boards can be controlled from the host computer via a USB connection as well.

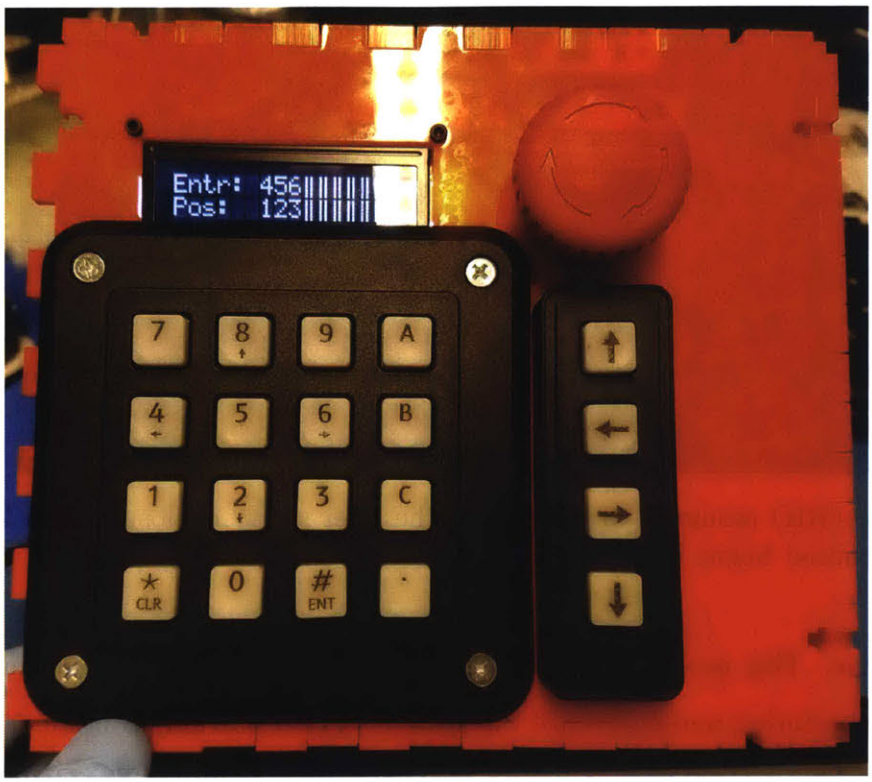

Figure 3-24: Front panel of the focus and tower control box.

Communications for the control electronics systems is provided through several different means, shown below in figure 3-25. The laser and cRIO chassis are linked to the host computer via Ethernet through a NETGEAR ProSAFE GS105 gigabit Ethernet switch. Ethernet is particularly suited to communicate with these devices as it allows for high-speed transfer of files and streaming of data. In contrast to the high-speed Ethernet communication, The focus control module and tower control module both interface with the host computer via USB serial ports. Additionally, the laser has a secondary serial interface that is connected to the host computer for control. The host computer communicates with the laser through multiple channels as some features can only be accessed by specific means.

The system has a secondary communication medium in the form of a Controller Area Network (CAN) bus. CAN bus is a multi-master, message passing serial bus used in the automotive industry to connect the wide range of sensors and computers in a

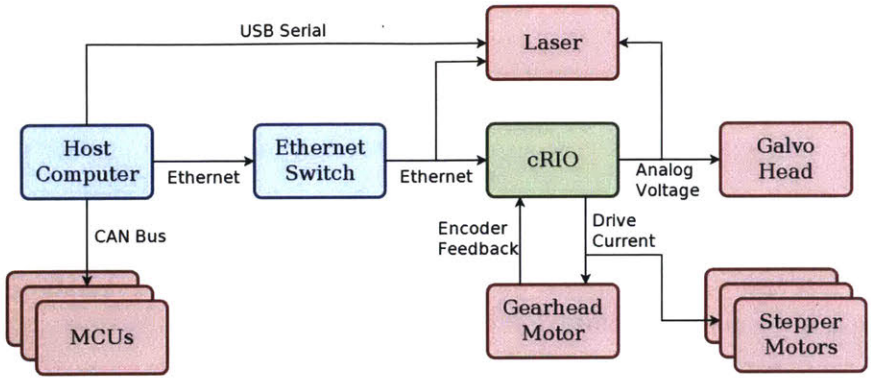

Figure 3-25: Schematic illustrating the communications interconnects in the galvanometer system.

car. In this system, the CAN bus runs between all of the control boards, the cRIO, and the host computer. It is used to replace a large number of individual USB connections with a single CAN transceiver for the computer, and simplifies adding additional controllers. However, as the system was completed and prepared for transition to the end users, a significant skill gap in programming and troubleshooting microcontrollers was identified. In order to smooth the transition to the new users and leverage their existing skill set, LabVIEW was chosen to drive everything centrally. The system was then retrofitted with a larger National Instrument cRIO chassis (part #9039) to allow for more modules. The control boards were replaced with stepper and DC motor control modules (NI part 9503 and 9501 respectively) installed in the cRIO which allowed the centralization of all embedded system control within LabVIEW.

3.2.8 Software System

The software system is responsible for all levels of system operation from the high-level processing of the user's solid model all the way down to the real-time control of the system's actuators. As with the mechanical design of the system, the software design focused on leveraging as many commercial-off-the-shelf items as possible as well as designing the software architecture in a modular, reconfigurable manner. The software pipeline for converting a solid model into a constructed part consists of three distinct stages: model parsing, waveform generation, and hardware control. Model parsing

converts a 3D solid model into the machine code that represent scan trajectories for building that part. Those generic machine commands are then converted into the signals necessary to drive the hardware through waveform generation. Once the waveforms have been synthesized, those signals are then passed to the hardware controller to drive the machine. The software pipeline is separated into these distinct phases as each one has well defined inputs and outputs, allowing each block to be interchanged as the system changes over time.

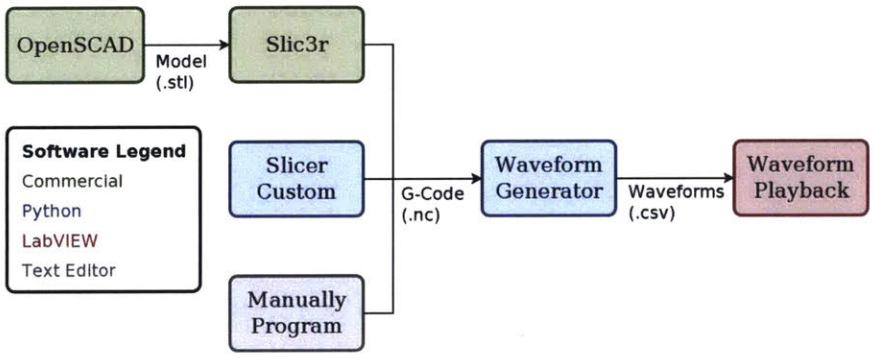

Figure 3-26: Schematic illustrating the software pipeline illustrating multiple means of generating the necessary G-Code.

Model Parsing

The model parsing phase is used to convert a solid model representation of an object into machine-readable NC code. This process is also referred to as slicing as that is the first step in the process. The input to this stage of the software pipeline is one of several 3D solid model representations: STL, AMF and OBJ. The output of this phase is machine-readable G-code, a numerical control programming language also known as RS-274.

The process of converting the model into the desired code is a three phase process consisting of slicing, infill generation, and code synthesis. The model first is sliced at a predetermined layer height, converting the 3D model into a set of 2D shapes. Each one of these shapes represents the area that must be fused in that layer. The shape is then passed through an infill generator that converts the 2D shape into a set of trajectories based on the infill pattern and processing parameters. These trajectories

are then converted into machine-readable G-code and packaged into a single ASCII file. One way of achieving this is to use a commercial-off-the-shelf software package to generate complex sets of trajectories. The slicer tested with the system, called Slic3r [139], is designed to generate code for fused deposition modeling 3D printers. By adjusting the slicing parameters, such as extrusion size, the software can be used to generate patterns that work with the SLM process. One issue that arises is that infill strategies for FDM printing are different from those used for SLM printing. However, the standard rectilinear crosshatching is the same in both processes, so the slicer can still be used if that infill pattern is acceptable. More complicated infill patterns geared towards SLM processing can be added in the future using the modular infill generator integrated in to Slic3r.

When full slicing package is not needed, the use can also use hand-writing or a custom vector slicer. The first approach is to simply hand write the G-code necessary to perform the operations required. This is often done when the shapes are simple, such as running a parametric search of process parameters with a series of lines. The second approach is to use an in-house trajectory generator that converts 2-dimensional vector maps image into G-code. Given an infill primitive, this Python script uses the geometry library to replicate the primitive over the area of the shape to create the infill pattern. The outline of the shape is then duplicated and reduced by a fixed amount to provide an inner border. By creating vertices at the intersection of the infill pattern and the inner border, a graph is created where the edges of the graph are the trajectories and the vertices of the graph are the intersections. The script then iteratively looks for Hamiltonian paths, the shortest path that visits a vertex only once, to create print trajectories.

Waveform Generation

The waveform generation phase is used to convert the machine code developed in the model parsing phase into a set of continuous signals that can drive the system. The input to this stage of the software pipeline is industry-standard G-code, generated by either one of the means discussed above, or any other system capable of creating

G-code trajectories. The output of this phase is a comma separated variable (CSV) file that contains the values for the analog voltage outputs as a function of a specified time interval.

One issue with the code generated in the model parsing stage is that it does not contain the right parameters for the hardware control system. Specifically, the process parameters for FDM printing, those included by default with commercial software, are parameters such as filament feed rate while SLM parameters include scan speed and laser power. To correct for this, the waveform generator strips out the FDM process parameters, if they are present, and adds in the SLM parameters per the user's specifications. In order for this process to occur, the user must specify the desired scan speed, laser power, and time step for the pattern.

The software for this portion of the pipeline consists of a Python script that takes in a G-code file and generates a CSV file from it. The output CSV is a discrete-time representation of the output waveforms with a fixed time step between each of the values. To generate this file, the script starts with an empty matrix that represents the output vector with one column for every output variable. As the script steps through the G-code commands, it creates a section of those waveforms by interpolating between the beginning and end states according to the time step and the specific command, which it appends to the output matrix. Once the script cycles through all of the G-code commands, it converts this matrix into a CSV and saves it for the user to transfer.

Hardware Control

The last phase in the software pipeline, hardware control, is responsible for making the machine run according to the waveform file. The input to this stage is the desired waveform CSV file, and the output is the operation of the experimental setup. Once generated, the user sends the generated waveform over the Ethernet network to the cRIO controller. Once transfered, the embedded computer in the cRIO loads chunks of the waveform into memory and streams them to the FPGA via direct memory

access (DMA). The FPGA then controls the analog and digital output according to the values passed and the time step specified.

3.3 Pressure Vessel Build System

The primary target environment for the SLM system is a pressure vessel with an internal multilayer recoater build platform. The purpose of this system is to investigate the impact of the content, pressure, and flow of the environmental gas on the SLM process. This subsystem has two primary components: the pressure vessel and the build system inside of it.

3.3.1 Pressure Vessel

The pressure vessel, as the name implies, serves to contain the atmosphere around the build environment and allows for greater-than-atmospheric conditions. The intent of this experimental endeavor is to explore the impact of pressure over the largest range possible. To source this component, we borrowed from the chemical processing community and modified the designs for a pressurized reaction vessel to fit our needs. The unit used in this setup is a Parr Instrument model #4762, constructed out of 316L stainless steel and equipped with a 3.88 in by 1.0 in oblong sapphire window. It has an internal working volume in the shape of a cylinder that is 2 in [50.8 mm] in diameter and 6 in [152.4 mm] long. The vessel is quipped with four $\frac{1}{4}$ inch NPT fittings on the top of the vessel and an additional one on the bottom of the vessel. In order to easily access the window on the vessel, as well as the ports, we constructed a stand to hold the vessel in a horizontal orientation beneath the objective of the F-Theta lens. A model representation of the pressure vessel on its stand can be seen below in figure 3-27.

Not pictured in the model representation of the pressure vessel are the high-pressure passthroughs used to route electrical signals into and out of the pressure vessel. Multiple types of passthroughs were purchased from Conax Technologies, the

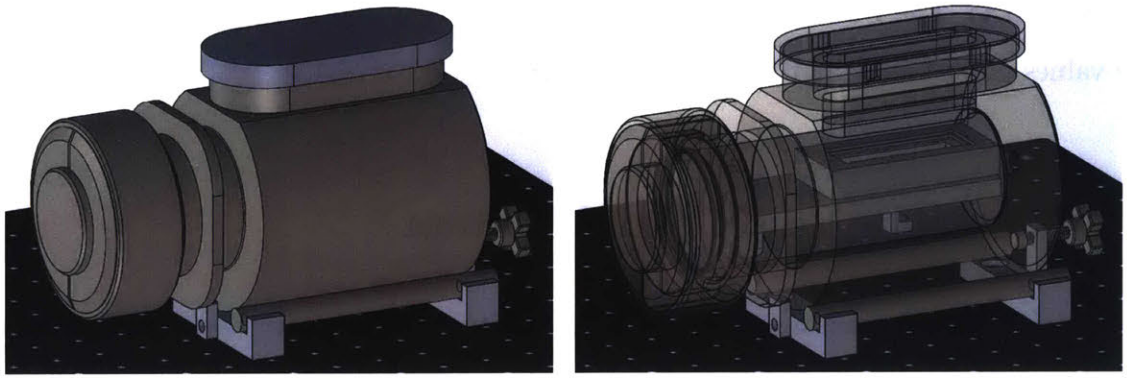

(a) (b)

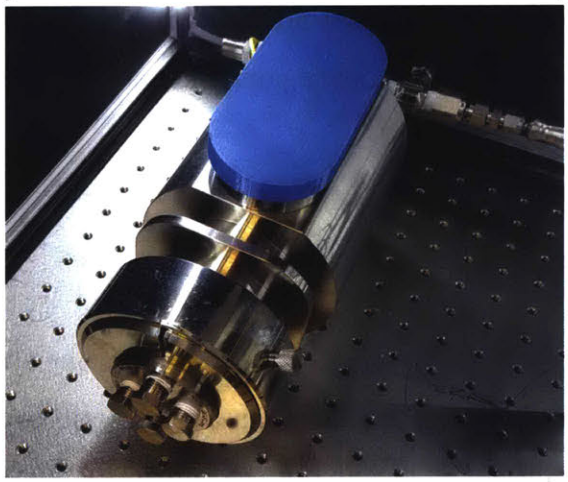

(c)

Figure 3-27: The pressure vessel as seen in (a) model representation its stand and (b) showing the single-layer build stage inside as well as (c) a picture of the vessel mounted on the optical breadboard with a safety cover fitted over the sapphire window.

most often used are the PL(PTM2/)-16-A4-T fitted with 4 16 gauge wires passthroughs, and the PL(PTM2/)-20(K)-A4-T fitted with 4 k-type thermocouple passthroughs.

3.3.2 Single-Layer Build Platforms

In order to test the pressure vessel and associated systems without the added complexity of the multilayer build system, we designed a single-layer build platform. The single-layer build platform takes similar sample tokens to the multilayer build system, but relies on the user to manually deposit a layer of build material much in the same way as for the LTS sample holder described in section 3.1.1.

Standard Single-Layer Build Platform

The standard single-layer build platform is a simple, non-actuated structure for testing single-layer SLM processing. It is constructed of a main build platform made of 6061-T6 aluminum, an upright and balance leg used to locate it inside the pressure vessel, the sample itself as well as a layer thickness shim and retaining plate, and a cover with an inset microscope slide. A model representation of the standard single-layer build platform can be seen in figure 3-28.

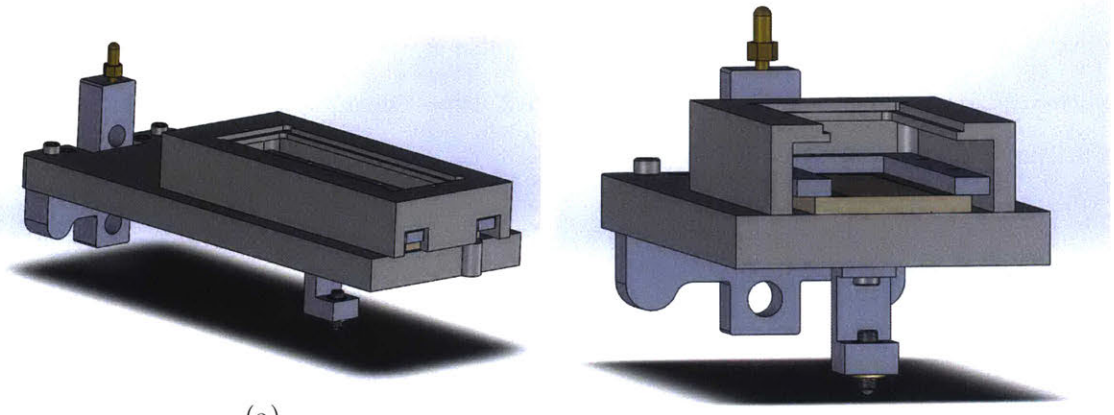

(a) (b)

Figure 3-28: Standard single-layer build plate.

To load the sample, the layer thickness shim is placed on top of the sample, and then both parts are clamped down using the retaining plate and a set of #2 machine screws. The operator the places a small amount of powder on top of the sample and spreads it using a doctoring blade that adjusted to contact the thickness shim. The cover is then placed over the prepared sample to protect the sapphire pressure vessel window from the melt plume, and the entire assembly is inserted into the pressure vessel. To ensure that the build plate is flat a vertical, a reference block is inserted into the two reamed holes in the platform upright and checked with a dial indicator.

Heated Single-Layer Build Platform

A modified version of the single-layer stage was designed to allow for heating of the test sample. As discussed in the previous chapter, heating the build plate can improve

process performance for some materials. To achieve a heated build plate, a relief was made in the original platform design to allow for a heating element and insulation. A model representation of the single-layer build plate can be seen in figure 3-29. The stack of material from the bottom to the top consists of an alumina-bisque ceramic insulating plate, 101 copper heat spreading plate, 6061-T6 aluminum build plate, test sample, second alumina-bisque ceramic insulating plate, and a 6061-T6 aluminum clamping plate. The stack of parts is held together via a set of #2 machine screws. To heat the copper heat spreader, a silicone encapsulated resistive heating element (McMaster Carr #35475K334) is attached to it via thermally conductive adhesive (McMaster Carr #7595A33). Additionally, a K-type thermocouple (McMaster Carr #9251T93) is attached to the the heat spreader to monitor the build plate temperature.

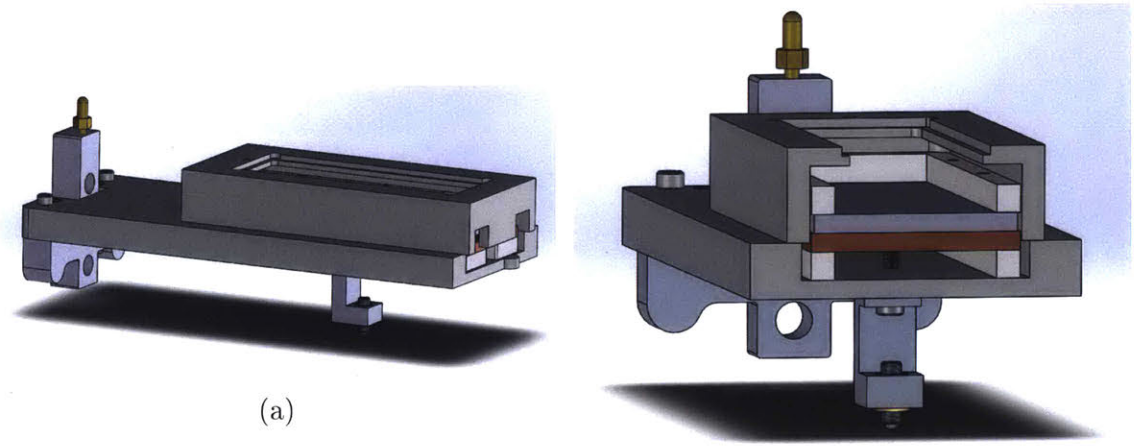

(a)

(b)

Figure 3-29: Model of the single-layer build plate, and cross-section showing, in order, the base plate, bottom insulator, heat plate, sample, insulator, and microscope slide holder.

3.3.3 Recoater System

The recoater system is design to provide multi-layer reocating capability inside of the pressure vessel. Designing the pressure vessel recoater system presented a unique challenge in that the entire system had to fit within the internal volume of the pressure

vessel. The internal space of the pressure vessel is a cylinder with a diameter of 2 in and a height of 6 in, easily an order of magnitude smaller than the machine space for commercial systems.

A large number of commercial systems use the three-column approach wherein the built system is composed of three chambers located next to each other. The first chamber holds the build material in preparation for use, the second chamber serves as the build volume, and the final chamber acts as an excess powder dump. In operation the build platform lowers by the layer height, the powder feed plate extends upwards to expose powder above the recoater plane, and the powder dump plate (if present) lowers down. The recoater then pushes the freshly exposed powder from the top of the feed chamber, across the build chamber filling in the empty space, with any excess being deposited in the powder dump chamber. A depiction of this system can be seen in figure 3-30.

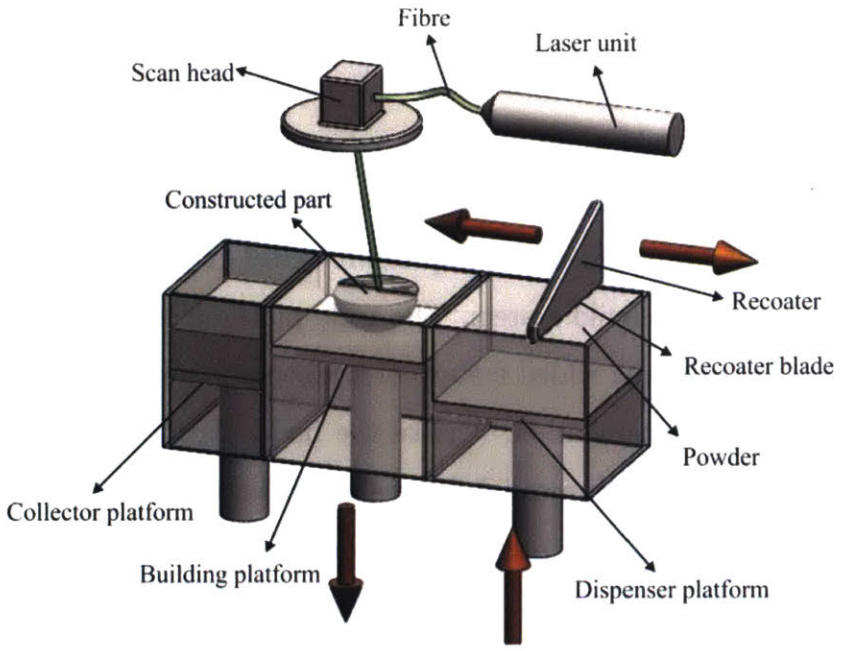

Figure 3-30: Representation of a common 3-chamber recoater system [43].

One of the side effects of using the 3-chamber system is that the machines tend to be large due to the amount of space required for each hopper. While this is not a significant issue for most commercial machines as they are generally not space constrained, implementing this inside of the pressure vessel would be challenging. In

order to achieve a multilayer recoater with recoating capabilities comparable to commercial machines, layer thicknesses from 10 µm to 100 µm, the traditional practices must be exchanged for a novel approach. A depiction of the system designed to fit within the pressure vessel chamber can be seen in figure 3-31.

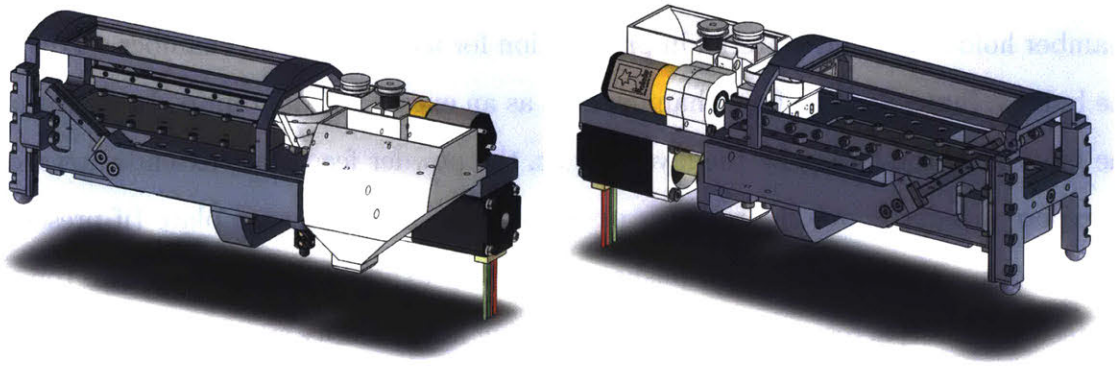

(a) (b)

Figure 3-31: Multi-layer recoater assembly for the pressure vessel

The multilayer build system includes all of the standard components of most commercial build systems: build platform, linear actuator, and recoater. The difference lies in that those components had to be miniaturized and folded on top of each other in order to fit within the confines of the pressure vessel. Figure 3-32 highlights the various components of the build system. The build platform is similar to traditional commercial systems with the added feature of a kinematic mount to allow for high-precision removal and reinstallation. Unlike the build platform, the vertical stage deviates dramatically from commercial designs and is implemented using a modified wedge-style actuation drive. The recoating system also deviates many from commercial designs as the powder is stored in a hopper and fed to a recoating cart in small amount to cover the build surface.

Build Platform

The build platform serves as a mounting point for the test sample. This portion of the build system is most similar to commercial in that it consists of a large baseplate with a series of mounting holes used to anchor the sample token on top of it, but it

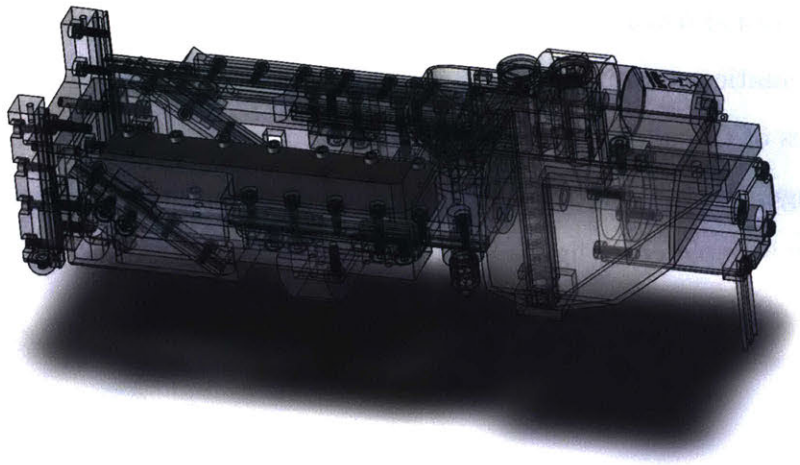

(a) The build platform portion of the build system.

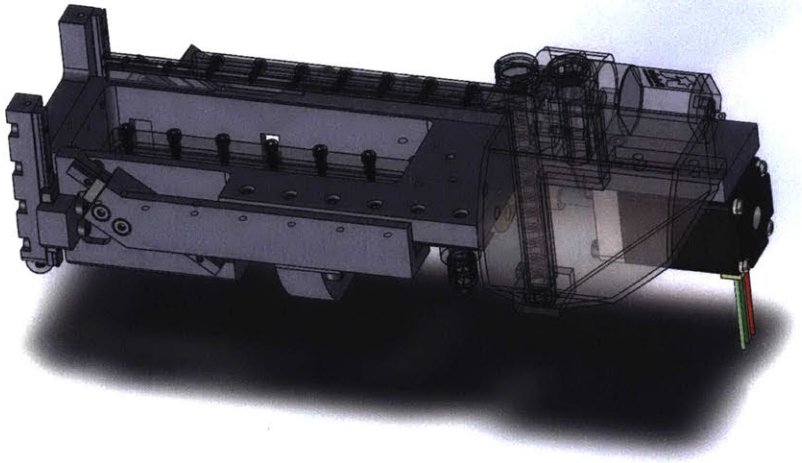

(b) The vertical actuation portion of the build system.

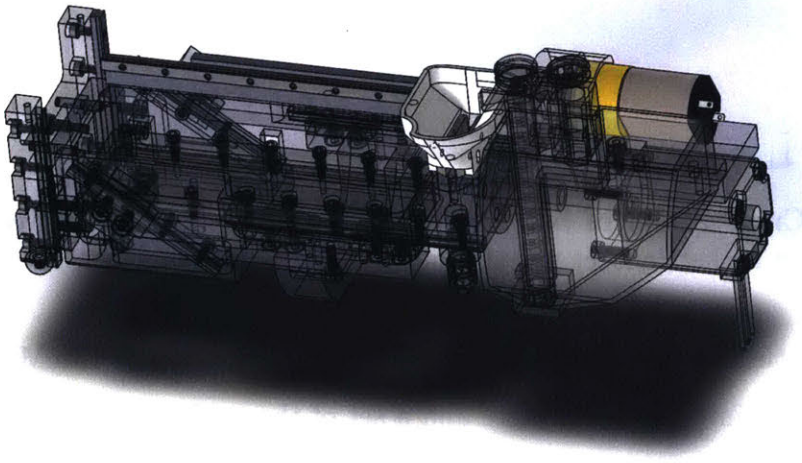

(c) The recoating portion of the build system.

Figure 3-32: The three primary subsections of the build system.

includes an additional feature. The build platform consists of the build plate, sample token, and kinematic mounting system. The build plate is a machine 6061-T6 plate that has a series of threaded holes to retain the sample. To retain the build plate on the vertical stage, the bottom of the build plate has an integrated kinematic mount. The build plate is depicted in figure 3-33.

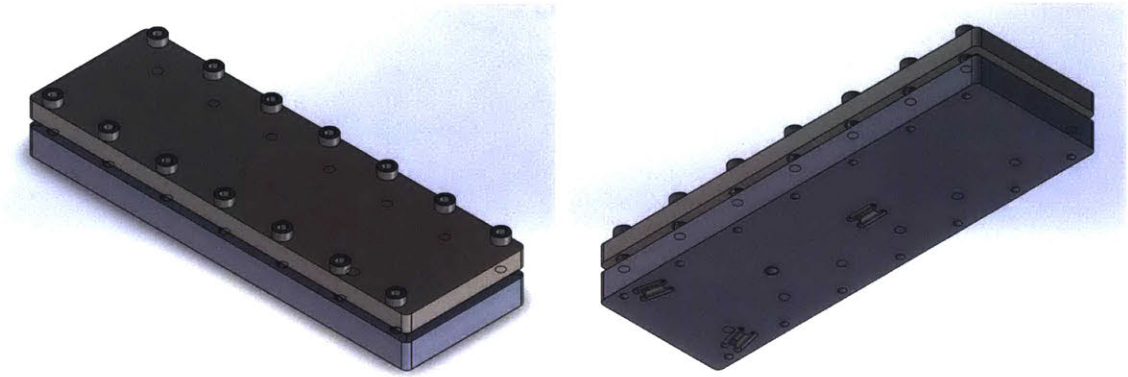

(a) (b)

Figure 3-33: Model of the build plate saddle.

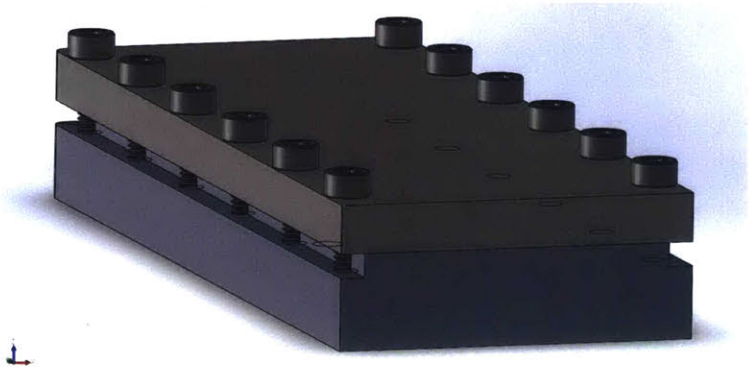

Figure 3-34: Cross-section of build platform assembly showing the recess for the neoprene sealing gasket (gasket not shown for clarity).

The kinematic mount consists of 3 pairs of 1 mm dowel pins (McMaster part # 93600A030) glued into the build plate and a set of three adjustable spheres attached to the vertical stage saddle. To apply clamping force to the build plate, a screw is inserted through a hole in the vertical stage saddle and threaded into the bottom of the build plate. A series of belleville compression springs are placed between the head of the screw and the bottom of the saddle so that is can rotate out of perpendicular

with the saddle's bottom surface while still exerting a retention force. This mounting systems allows for ease of remove and reinstallation of the build plate with a high degree of repeatability due to the exact constraint nature of the mounting system.

Vertical Stage

The vertical stage portion of the build system is responsible for positioning the build platform in relation to the recoating assembly. In commercial machines, the vertical state is commonly a large plate attached to one or more linear actuators which directly move that plate. In this case, the vertical actuator is more akin to a pair of wedge-shape blocks placed on top of each: as the lower wedge is pushed or pulled, the upper wedge slides on the lower wedge and is raised or lowered respectively. A depiction of this operating principle can be seen in figure 3-35. This style of vertical actuator is common in high-precision vertical stages where incremental movements are measured in nanometers.

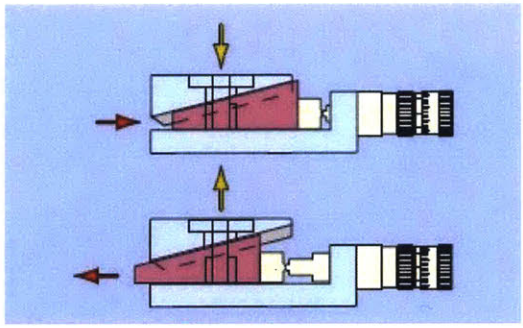

Figure 3-35: Simplified representation of a wedge stage showing how it operates [140].

However, unlike those stages, this implementation is considerably more complex because it must wrap around the build volume. The issue is that the build volume occupies the center of the space within the pressure vessel, and the stage cannot interfere with the recoater or laser window. A model of the vertical actuator can be seen in figure 3-36. The actuator is composed of three primary components: drive motor and leadscrew, crossplate and drive arms, and the build plate saddle.

The drive motor converts electrical pulses into controlled angular rotation, and the leadscrew converts that rotary motion into linear displacement. The drive motor

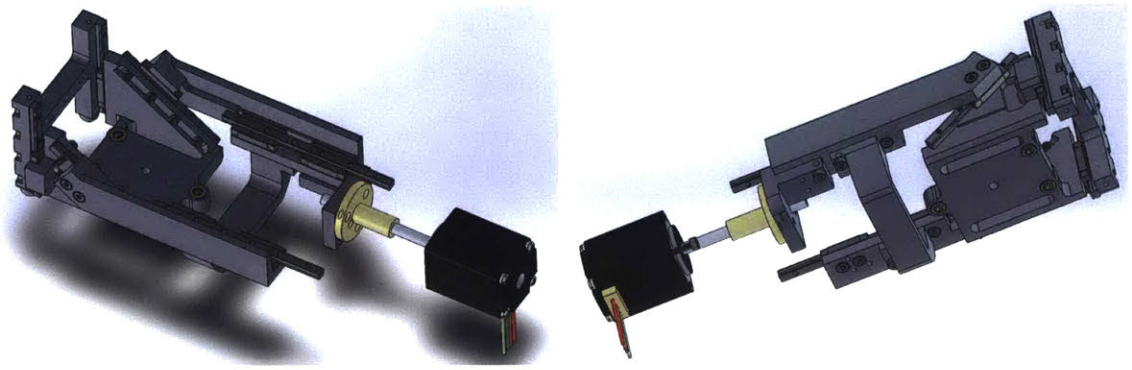

(a) (b)

Figure 3-36: Model of the build plate saddle.

is a NEMA 8 stepper motor with an integrated ACME threaded leadscrew and nut (Haydon Kerk #E21H4U-2.5-900). The leadscrew nut is fixed to a mounting plate machined form 6061-T6 aluminum that is attached to one of the drive arms using a pair of 1.5 mm dowel pins and a M2x0.4 screw. A model of the drive motor and leadscrew is shown in figure 3-37.

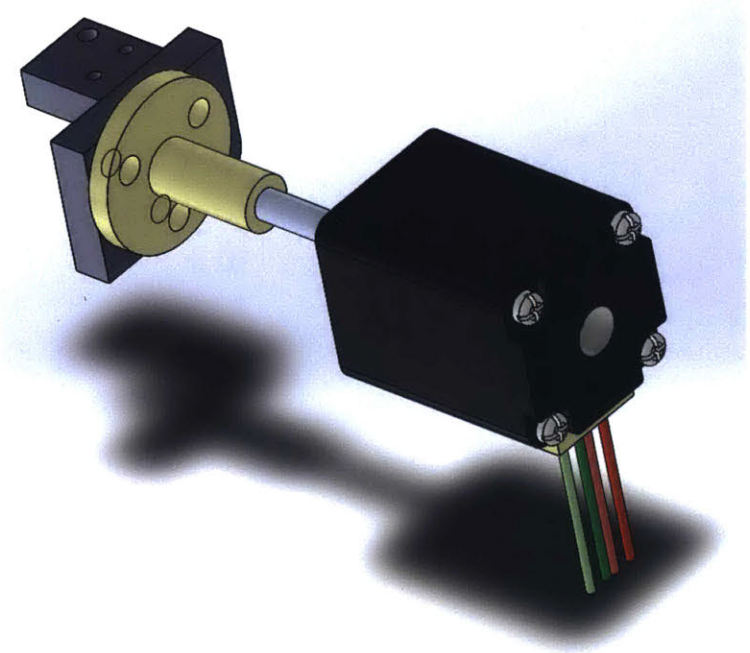

Figure 3-37: Model of the drive motor and leadscrew.

The crossmember and drive arms transfer that linear motion from the leadscrew nut and convert it to vertical displacement in conjunction with the build plate saddle.

The crossmember, constructed from 6061-T6 aluminum, connects the two drive arms together using 1.5 mm dowel pins and M2x0.4 screw. Each drive arm is machined from 6061-T6 aluminum and serves as the mounting point for two different linear bearings. One linear bearing constrains the motion of the drive arm while the second linear bearing is coupled to the build plate saddle. Models of the parts can be seen below in figure 3-38.

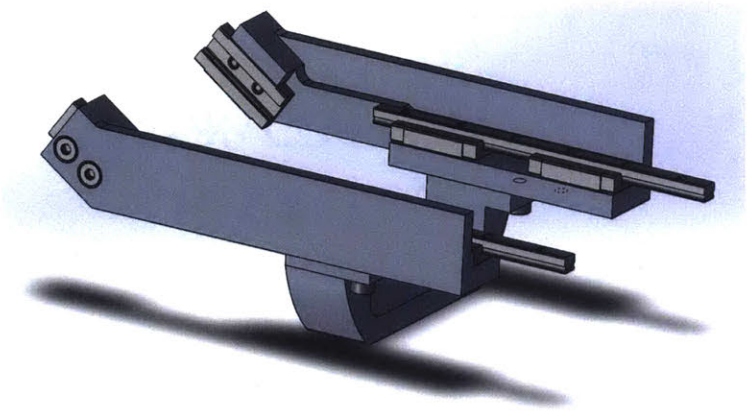

Figure 3-38: Model of the drive arms and crossmember.

The build plate saddle acts as a mounting point for the build plate assembly, mentioned in section 3.3.3, and precisely constrains the motion so that it is vertical. The build plate saddle serves to both act as a mounting point for the kinematic build plate mount as well as a translation mechanism for converting the horizontal driving force from the drive arms into vertical motion. The saddle is constructed of a U-shaped piece of 6061-T6 aluminum with three precision adjustment screws and two pairs of linear bearings. The M3x0.2 precision adjustment screws (ThorLabs part #F3ES8) constitute half of the kinematic mounting system that locates the build plate assembly. For the linear bearings, one pair of linear rails (McMaster Carr part #8381K390) is located on the back of the saddle and ensures that it can only travel vertically, while the second set of linear rails is attached at an angle, the carriage of which is connected to the drive arms. Combined together, the linear bearings translate the horizontal force from the drive motor into a vertical motion. The angle of the linear bearing rail controls the conversion ration between horizontal movement and vertical displacement, and is dictated by the competing needs of vertical positioning

resolution and space require throughout the travel. Figure 3-39 shows the build plate saddle.

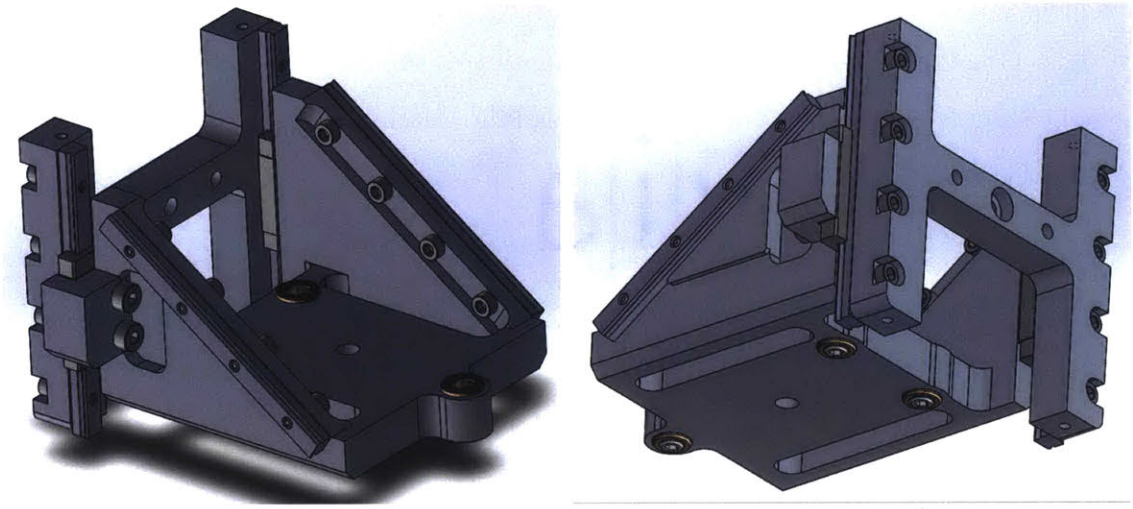

(a) (b)

Figure 3-39: Model of the build plate saddle.

Lowering the stage requires that the motor rotate in the clockwise direction (as seen from the back or non-leadscrew side of the motor). As the motor rotates, the leadscrew nut is driven away from the motor, pushing the crossplate and drive arms away as well. This motion applies a downward force on the build plate saddle due to the angled linear guides, and this causes it to travel downwards. Raising the stage is the opposite process: the motor spins in the counter-clockwise direction, pulling the leasdcrew nut and drive arms towards the motor, applying an upward force to the build plate saddle.

Recoater

The recoating portion of the build system is responsible for dispensing the build material into a uniform layer on top of the build platform. In commercial machines, the recoater is often a fixed blade or rotating cylinder attached to a linear stage that is swept across the build surface. While this systems borrow heavily from traditional fixed-blade recoaters, there is insufficient space to house the powder near the build platform, and implements a different approach by integraing a hopper into the recoat-

ing blade. The recoater assembly consists of three main subcomponents: recoating cart, cable drive system, and powder feed hopper.

The recoating cart serves the traditional function of spreading powdered build material over the build surface, but has the additional feature of storing a small amount of powder used to recoat the build surface. The recoating cart assembly consists of body of the cart, a pair of machined 6061-T6 recoating blades, and a linear bearing. The original cart body was prototyped using a stereolithography 3D printer, but was later replaced with a machined 6061-T6 aluminum body. A picture of the recoating cart model can be seen in figure 3-40.

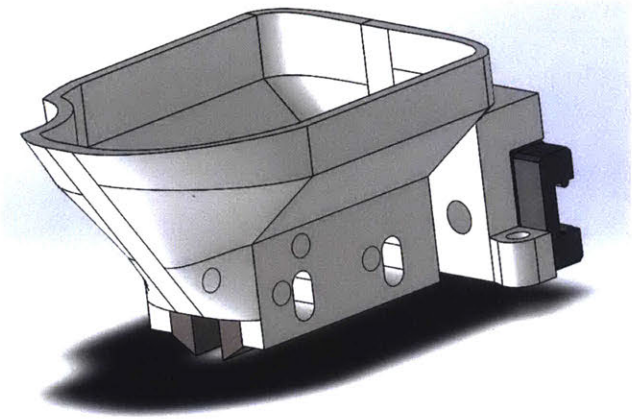

Figure 3-40: Model of the recoating cart.

The cable drive subsystem serves as the actuation mechanism for the recoating cart. Traditional SLM systems use a leadscrew or belt drive system for moving the recoater, but space constraints prevents the use of these techniques inside of the pressure vessel. To overcome the space limitations, the recoating cart is actuated using a Kevlar thread driven by a 3D printed capstan system coupled to a DC gearmotor (Pololu part #1597). The thread is attached at one end to the recoater cart, wrapped around the drive screw in capstan, run down to the opposite end of the stage, wrapped around a bearing surface, and is then attached to the cart at a second location. To assist in maintaining tension, small springs are located at each end of the Kevlar thread. A model of the capstan drive system can be seen in figure 3-41.

While the recoating cart holds a small amount of powder, the system requires a powder feed hopper to refill the cart for large print volumes. The space constrains

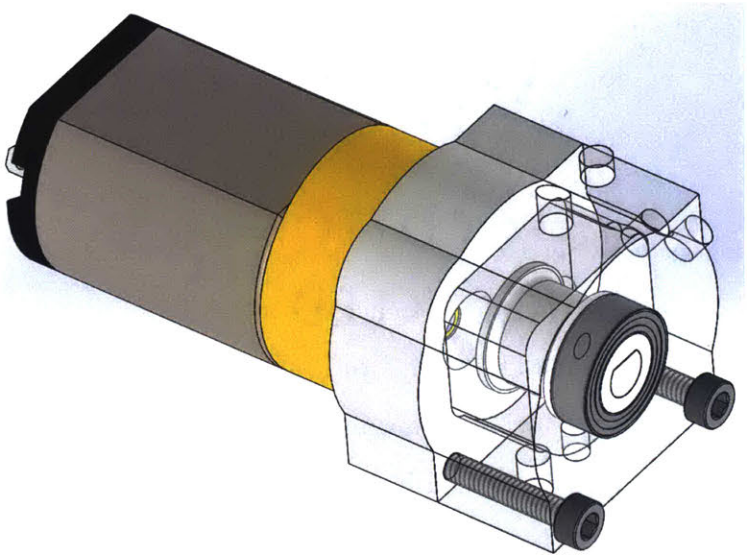

Figure 3-41: Model of the capstan drive system for the cable drive.

within the pressure vessel limit the size of the recoating cart and the amount of powdered build material it can carry. To overcome this limitation, the build system includes a powder hopper to store additional build material as well as a screw feeder to transfer the powder into the recoating cart. The parts for the hopper and feed screw were fabricated on a photolithographic 3D printer and are held together using light interference fits. The powder feed screw is driven by a micro DC gearmotor (Polulu part #2359) via an o-ring drive belt. When the recoating cart is docked fully to the rear of the stage, the motor activates to dispense additional build material into the cart. Models of the powder hopper assembly can be seen in figure 3-42.

An issue with the lift screw was discovered during initial testing. While the original hopper design functioned with nylon powder, it proved to be less effective when used with stainless steel powder due to the smaller powder size and higher weight. In order to overcome this issue, the lift screw was tilted at an angle to mimic an Archimedes' screw. The slanted screw developed a better seal on the bottom edge, allowing it to better lift the smaller and heavier stainless steel powder. Models of the modified powder hopper assembly can be seen in figure 3-43.

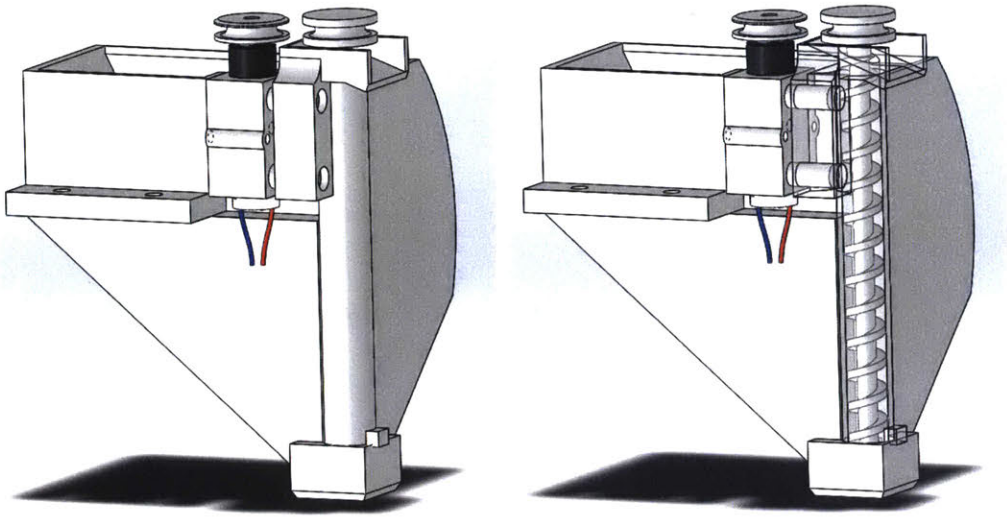

(a) (b)

Figure 3-42: Model of the powder hopper subassembly with a wireframe view showing the details of the powder feed screw (drive o-ring not shown).

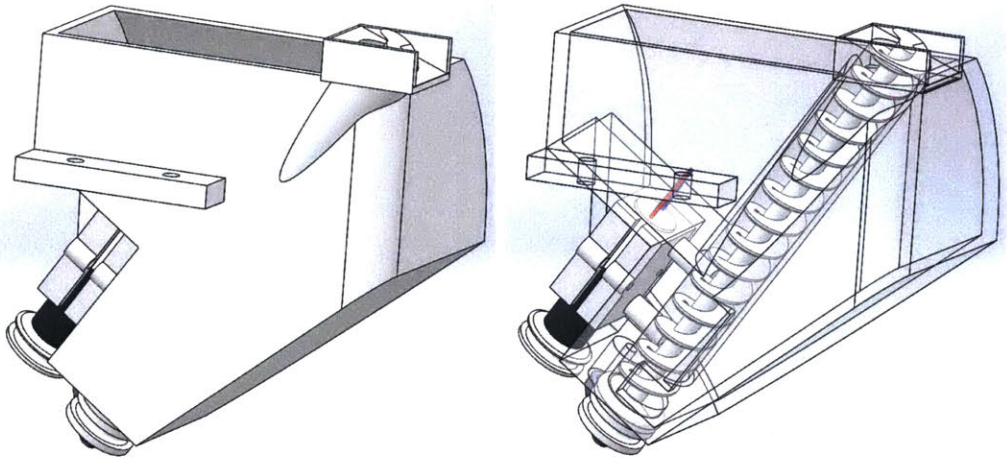

(a) (b)

Figure 3-43: Model of the updated powder hopper subassembly with a wireframe view showing the details of the powder feed screw (drive o-ring not shown).

THIS PAGE INTENTIONALLY LEFT BLANK

Chapter 4

System Testing

The goal of initial testing and evaluation was to determine if the system could meet the basic set of requirements for beginning experimentation in selectively fusing metals. The requirements for this were:

1. Interpret a G-code file and generate the correct waveforms to run the system according to the commands.
2. Drive the system according to the waveforms synthesized.
3. Fuse a 100 µm layer of 316L stainless steel powder into a solid weld bead.

While the system has many features and capabilities beyond this, by meeting those requirements, other researchers can begin to use the system for research as the rest of the components are brought online.

4.1 Galvanometer Control Test

The initial test for the integrated system was to verify that the galvanometer system could properly steer the laser beam to the desired location. To perform this test, a test pattern was synthesized and run on the system to compare the actual beam trajectory to the specified trajectory. The goal of this experiment was to verify the system could convert a set of G-code commands into the correct waveforms, and then play them back on the hardware to position the beam in the correct location.

4.1.1 Methodology

The first stage in testing the laser platform was compiling a test sequence to run. The system has three core G-code commands that are necessary to perform experiments: G0, G1, and G2/G3. The G0 command is used to jump the laser from one position to another, necessary when moving between unconnected features. The G1 command is used to sweep the laser in a straight line from one position to another, or hold the laser in one location for a period of time. The G2/G3 commands are used for sweeping the laser in a clockwise or counter-clockwise circular curve. Figure 4-1 shows the representation of a series of G-code commands used to test the system.

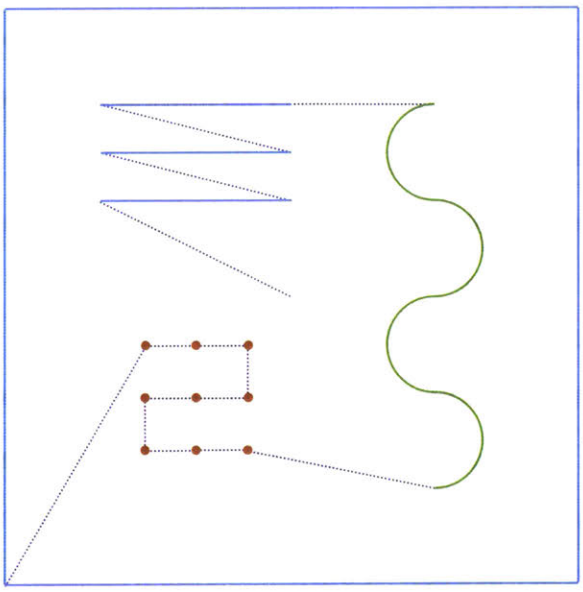

Figure 4-1: Test pattern showing the various commands including jump-to (dashed purple), linear move (blue), dwell (orange), and circular curves (green).

The compiled G-code file was then fed into the waveform generator to synthesize the control waveforms. Those waveforms were uploaded to the machine over the Ethernet connection and played back in a continuous loop to allow for observation. With the system continuously running the pattern, a printout of the pattern was placed beneath the objective to verify operation.

In order to allow for the enclosure to be open, the primary laser was not used to perform the testing. To provide an eye-safe laser source, a secondary 4.5 mW 532 nm

laser was fitted to the auxiliary input port and directed into the galvo using the removable prism.

4.1.2 Results and Discussion

The first round of testing did not generate the designed test pattern. A problem was identified with a sign error in synthesizing the curved (G2/G3) trajectories of the pattern. The sign error resulted in the clockwise and counterclockwise patterns being reversed. After correcting the error, the trajectory generated by the laser matched the designed test pattern.

The beam steering test verified the system's ability to synthesize waveforms according to a provided set of G-code and then drive the system according to those waveforms.

4.2 Laser Focus Test

With the laser steering system operating as designed, the next step was to evaluate the focus of the laser spot generated by the F-theta lens. To test the F-theta lens focus, the laser was fired at the focus camera, and the resulting images inspected for the beam spot size. The goal of this test was to determine the minimum spot size the system could generate as well as quantify the effective focal range.

4.2.1 Methodology

The test and evaluation methodology of the laser focus testing can the broken into two categories: data acquisition and data analysis. In the data acquisition phase, the system was run with minimal laser output projected at the focus camera to inspect the beam. Following the data acquisition, the grayscale images of the beam profile were mapped to a Gaussian beam profile and the spot size was extracted from that information.

Data Acquisition The system was set up with the focus camera located in the enclosure directly underneath the laser objective. The galvanometer mirrors were then set to project the beam directly downwards, both mirrors set to 0° displacement, to illuminate the camera's CMOS image sensor. The focus head was then moved into approximately the correct position for focusing the beam onto the camera's CMOS sensor.

With the safety enclosure closed for operator safety, the laser was set the laser to the lowest possible power setting and engaged. The focus camera was then triggered to capture the beam profile. Once the image was captured, the laser was shut off so that the enclosure could be opened and the focusing stage moved. Due to ongoing equipment modifications, the stage was manually moved by spinning the leadscrew, and the translation measured with a set of calipers. The process was then repeated 3 mm in both directions from the start location.

Data Analysis To make use of the beam images, the spot size had to be extracted from them. The first step was importing the grayscale images into MATLAB and converting them to a set of matrices. The image matrices were then each normalized between the brightest and darkest pixels to increase the dynamic range of the image, and the brightest pixel found. Using MATLAB's fit function, a Gaussian surface was fit to the pixel intensity information. With the Gaussian fit, the 4σ beam diameter was pulled out of the returned Gaussian surface parameters and plotted together with the other spot sizes.

4.2.2 Results

18 different measurements were taken over the length of 6 mm. An example beam profile picture and the fitted Gaussian surface can be seen below in figure 4-2.

The 4σ spot sizes were collected together and plotted to determine the focus spot size behavior. Figure 4-3 shows a plot of the laser spot size as a function of the stage position. The smallest measured spot size was 77.4 µm.

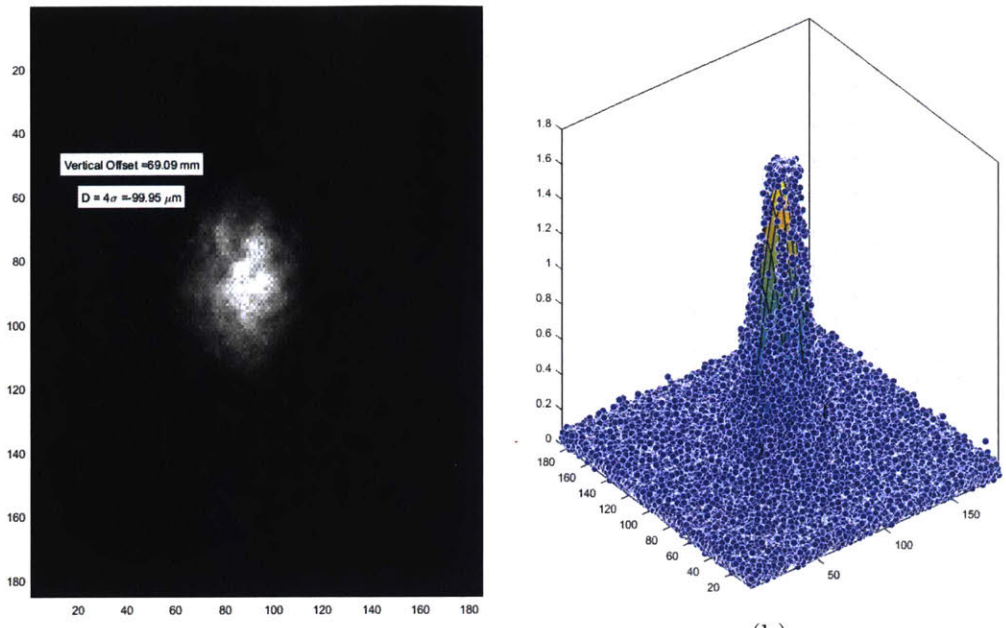

(a) (b)

Figure 4-2: One data capture from the focus camera showing (a) the grayscale image captured and (b) the Gaussian fit to the intensity data.

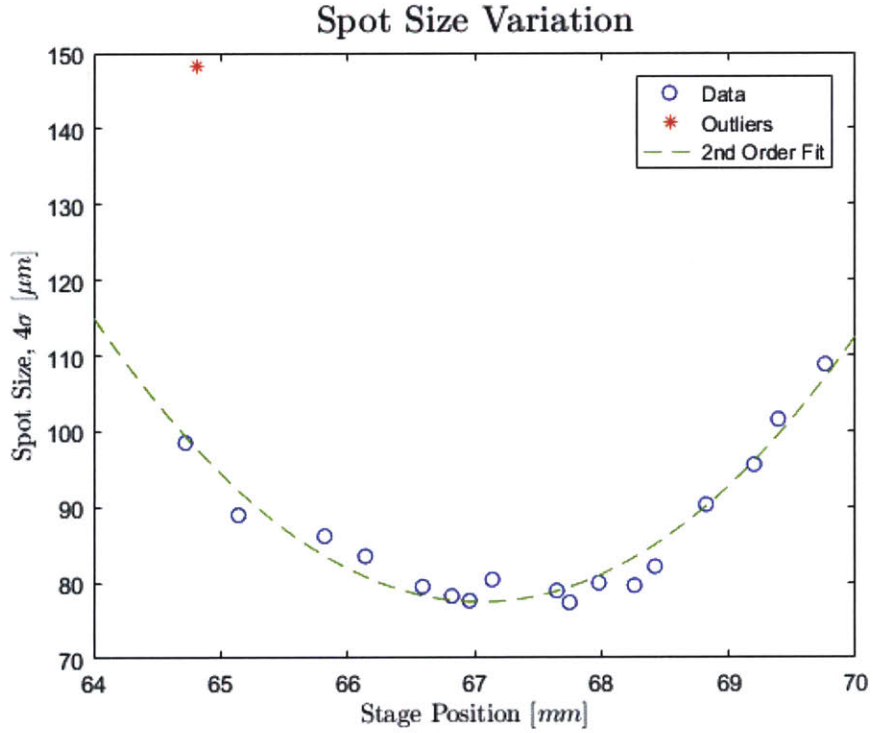

Figure 4-3: Plot of the measured beam spot sizes as a function of the focus head position.

4.2.3 Discussion

Of the 18 measurements taken, 17 were used in fitting a second order polynomial. One measurement deviated by almost 50% and was discarded as an outlier due to experimental error. The focus size exhibited the standard "bathtub" style beam waist that occurs near the focal point of a Gaussian beam.

Given that the F-theta lens is designed to produce a diffraction-limited spot size of 26 µm, the system was not generating a spot size as small as possible [55]. While the lens may be capable of achieving a spot size of 26 µm, that is dependent on a multitude of factors, including the input beam diameter. The smallest focus spot size is achieved when the input beam is as large as the design allows, 12 mm in this case, but the collimator used in this system only projects an 8 mm beam. The Zemax OpticStudio was used to calculate the enclosed energy using the manufacturer's optical models paired with an 8 mm beam, seen below in figure 4-4, and the minimum focus spot size increased to 37.9 µm. While this is still significantly smaller thant he measures minimum spot size, the remainder of the increase is likely due to misalignment of the optical elements, exaggerating the effects of beam divergence.

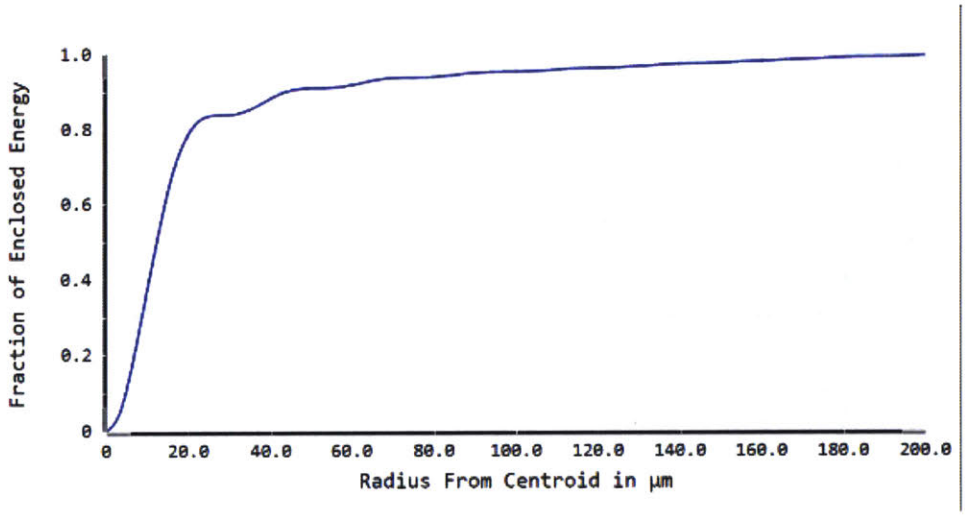

Figure 4-4: Enclosed energy plot from a Zemax OpticStudio simulation of the ideal F-theta lens with a smaller 8 mm input beam.

The focus test demonstrated the system's ability to generate a focus spot on the focusing camera. While the spot was not as small as the equipment is capable of

achieving, matching that performance is a matter of realigning the optical pipeline. Even with the lower-than-specified performance, the focused spot size was still smaller than the 100 µm spot sized used by commercial systems, as discussed in section 2.3.2. This means that the system can be defocused to match industry operating conditions if desired.

4.3 Spot-wise Laser Test

With the steering system functioning as designed and the focus of the laser verified, the next step was to integrate the laser. To test the activation of the laser through the real-time controller, a pattern that consisted of a series of point dwell exposures was used. The goal of this test was to verify that the laser could be engaged for varying amounts of time at varying power levels.

4.3.1 Methodology

To test the control of the laser, a test pattern was needed to vary the laser with. The simplest pattern to achieve this was an array of point exposures. This had the advantage of eliminating any potential motion-based issues, and allowed for an initial study into the effect of both beam power and beam exposure time. To further reduce variables, the laser was tested on a bare piece of $\frac{1}{8}$ in 316L stainless steel plate. To protect against oxidation, the sample was mounted in the single-layer sample holder purged with argon gas.

The focus was adjusted to achieve a 100 µm spot size on the sample.The system was then programmed to generate an array of 15 × 15 exposures ranging from 10 ms to 100 ms and 10% to 100% power. Following the experiment, the sample was inspected with optical microscopy, stylus profilometry, and scanning electron microscopy (SEM).

4.3.2 Results and Discussion

The first method of inspection following the experiment was an optical microscope. A grid of images for the range of powers and dwell times can be seen in figure 4-5. The grid shows an increasing crater size with increasing power and exposure time as expected. However, at the highest dwell times, the craters appear to shrink back down.

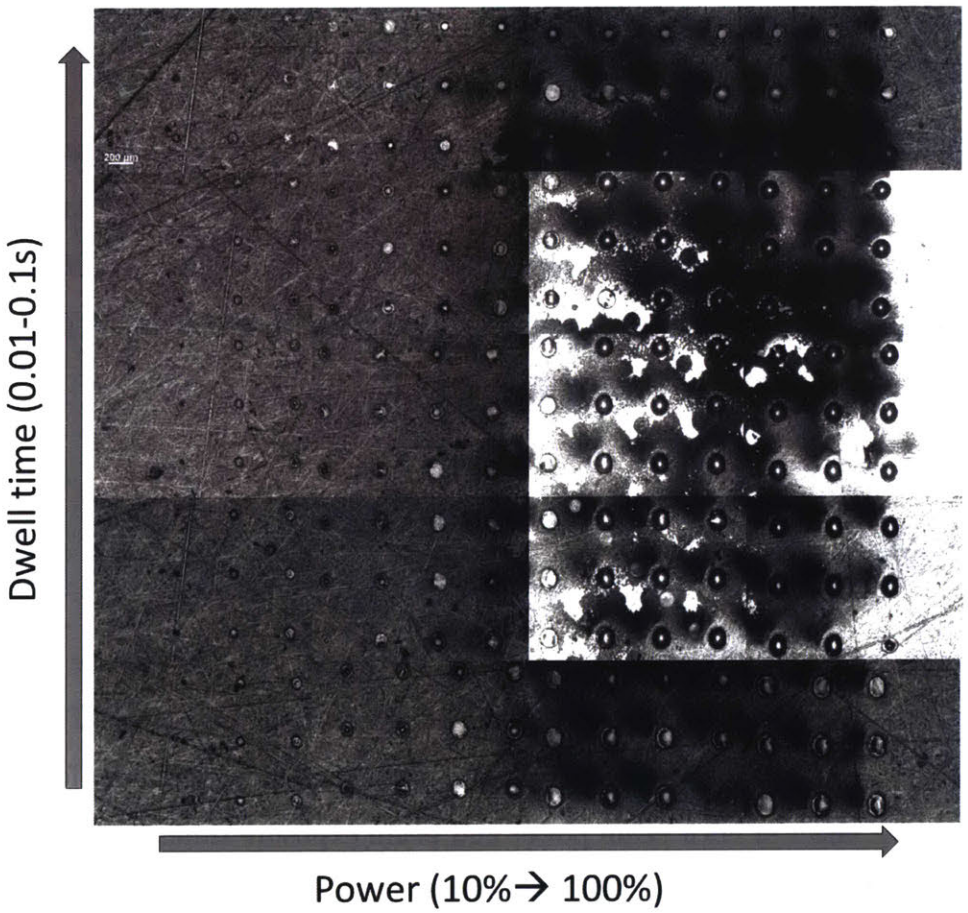

Figure 4-5: Grid of point exposures ranging in time from 10 ms to 100 ms and 10% to 100% power.

Following optical microscopy, the samples were inspected with a stylus profilometer, seen below in figure 4-6. The stylus profilometer captured the surface height map, showing the depressions the laser generated. As was seen in the optical microscopy, the crater sizes do not continuously increase with dwell time.

One interesting takeaway from the stylus profilometer measurements is the relationship between dwell time and hole depth. The depth of the pocket increases with dwell time, as expected, but only to a point. After increasing, the hole depth then begins to decrease with increased time, against what one would expect. One potential cause could be recoil pressure driving the metal out of the hole during the short time periods, but as the dwell time increases the melt pool is drawn back into the hole due to surface tension.

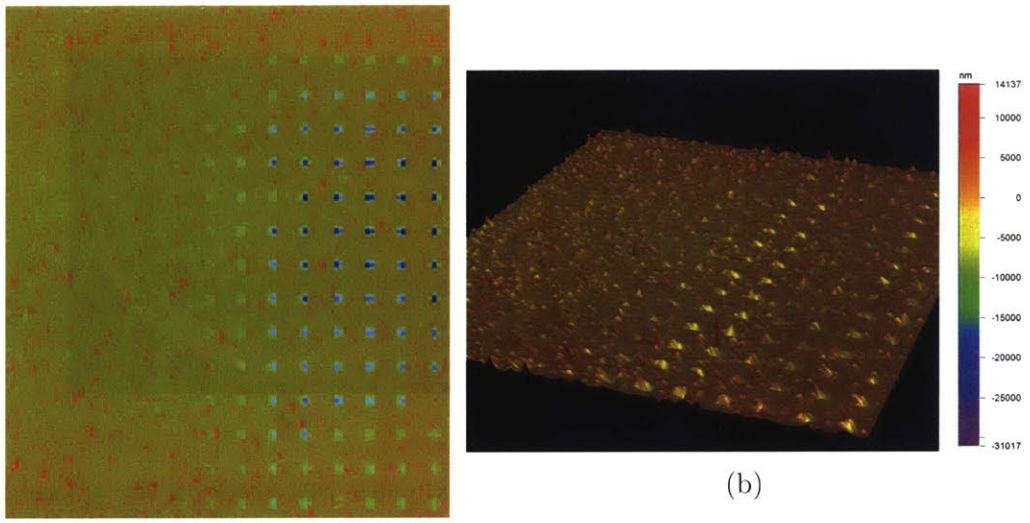

(a) (b)

Figure 4-6: Stylus profilometer measurements of the sample from a (a) top and (b) side view.

The final inspection technique used was scanning electron microscopy, seen below in figure 4-7. SEM imaging provided high-resolution imaging of the crater left by the laser. Of particular interest in these images is a series of concentric rings that occurs in the craters.

An interesting observation is the rippling pattern seen in the SEM images. The center of the melt spots exhibit an odd series of concentric circles that look similar to an optical interference pattern. As these rings look similar to Newton's rings, which are generated when a spherical surface and a planar surface come into contact, it is possible there is some form of destructive interference occurring in the optical pipeline. An alternative explanation could be a decaying oscillation in the laser's

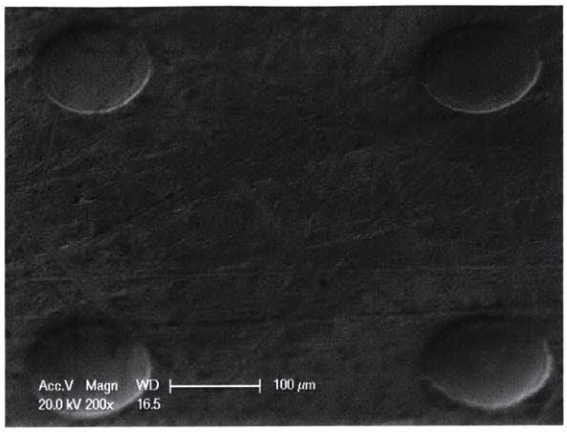

(a)

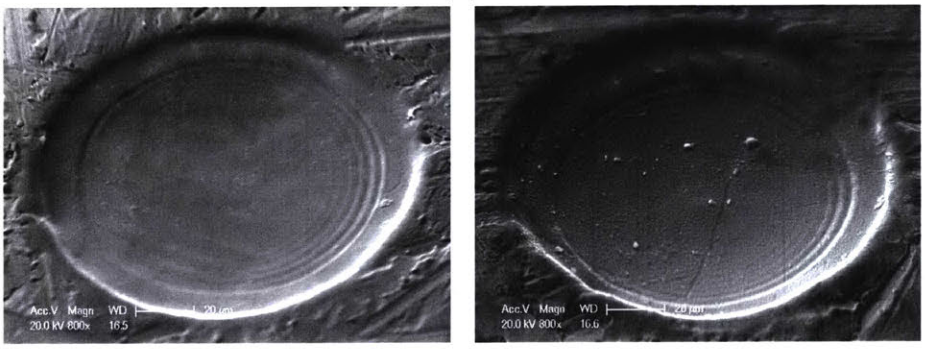

(b) (c)

Figure 4-7: SEM images of the point-wise laser exposure test showing the appearance of concentric rings in the exposure site.

output power when it is shut off, leading to a series of successively smaller power pulses to the melt pool.

While the spot-wise testing yield a number of interesting results that warrant further investigation, the test was a success. Generating the field of melted pockets verified the system's ability to position the beam and trigger the laser in a synchronized manner.

4.4 Line Fusion Test

With controlled steering of the beam and modulation of the laser demonstrated separately, the next element to test was fusing powder. To test fusing powder, a series of line segments was programmed to combine the variables of scan power and scan

speed. The goal of this test was to verify the system could fuse linear tracks of powder into solid features, the atomic operation in powder bed fusion.

4.4.1 Methodology

Before mounting the sample in the samples holder, the working surface was cleaned with isopropyl alcohol and acetone to remove surface conamination. The next step in preparing the sample was to apply a layer of powder to the substrate. The sample was covered with a 100 µm layer of 25 µm 316L stainless steel powder. Before loading the sample, the focus was adjusted to achieve a 100 µm spot size on the sample. Enclosed in the sample holder and back-filled with argon, the samples was loaded into the machine.

The test consisted of running a series of parallel lines with varying speed and power. The speed was varied from 20 $\frac{\text{mm}}{\text{s}}$ to 80 $\frac{\text{mm}}{\text{s}}$ and the laser power was modulated from 30% to 100%. A representation of the test pattern can be seen below in figure 4-8.

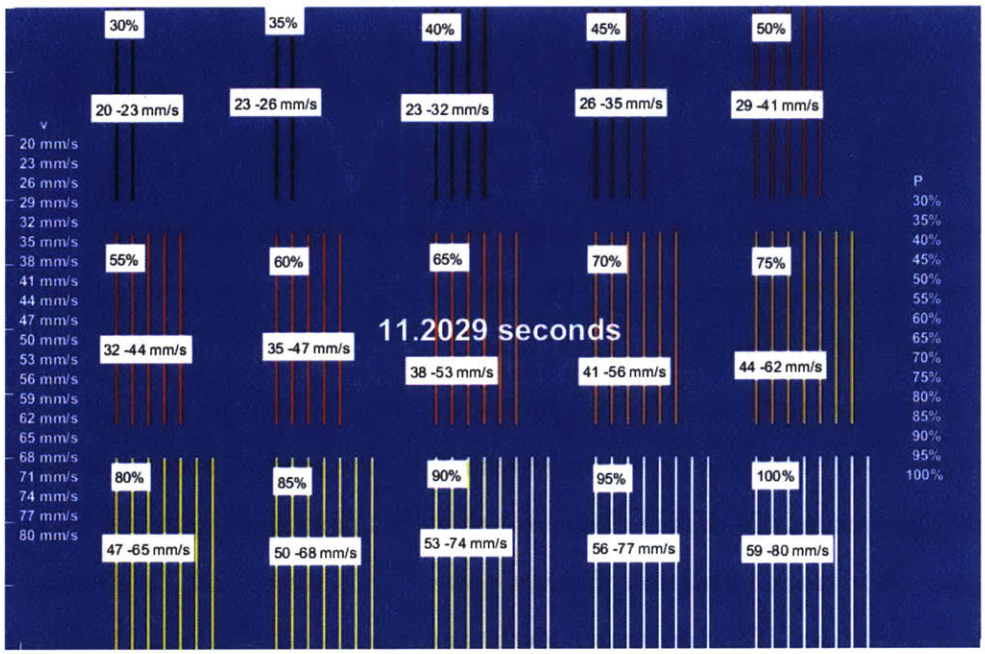

Figure 4-8: Grid of line exposures ranging in speed from 20 $\frac{\text{mm}}{\text{s}}$ to 80 $\frac{\text{mm}}{\text{s}}$ and 30% to 100% power.

4.4.2 Results and Discussion

Before testing the line pattern, the powder was inspected using an optical microscope. Figure 4-9 shows a pair of images of the 25 µm 316L stainless steel powder used both before and after the experiment. The virgin powder appeared highly spherical and exhibited little to no satellite adhesion which is desired for flowability and apparent density. After processing however, the powder particles showed a significant level of degradation including the adhesion of satellite particles.

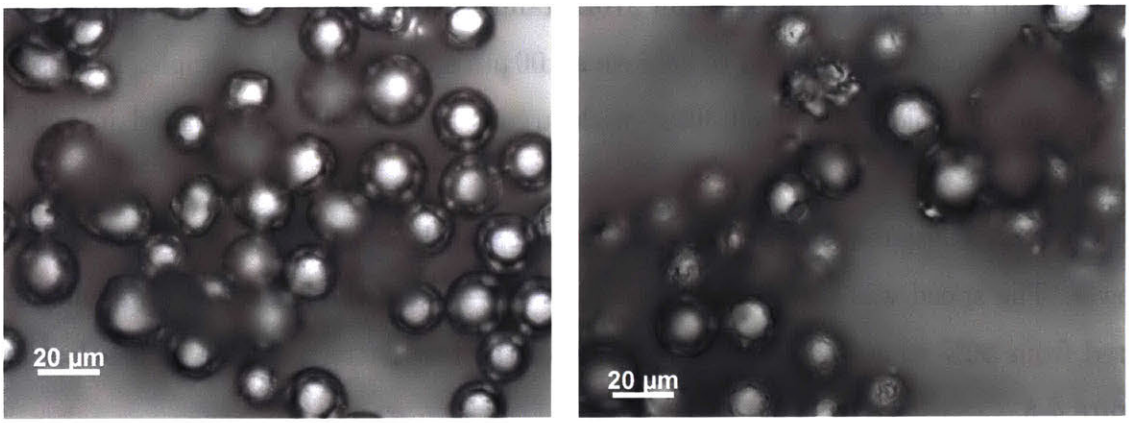

(a) (b)

Figure 4-9: Optical microscope images of the 316L stainless steel powder (a) before and (b) after it was used in the experiment showing the reduced surface quality and increase in satellites.

Once the powder was verified to meet the product requirements, the sample was coated and the test pattern run. The final fused pattern can be seen on the test coupon below in figure 4-10.

On closer inspection, the results from the line test varied considerably. As can be seen in figure 4-11, with the speed range tested, power settings around 40% achieved good track formation. Deviating above or below this power setting quick led to either balling and poor track formation if lower power levels were used, or ablation of the power and melt track if higher power levels were used.

While extensive work needs to be performed in exploring the parameter space for this material, this test was a success. The system demonstrated the ability to generate a continuous line of fused powder, the key operation for powder bed fusion.

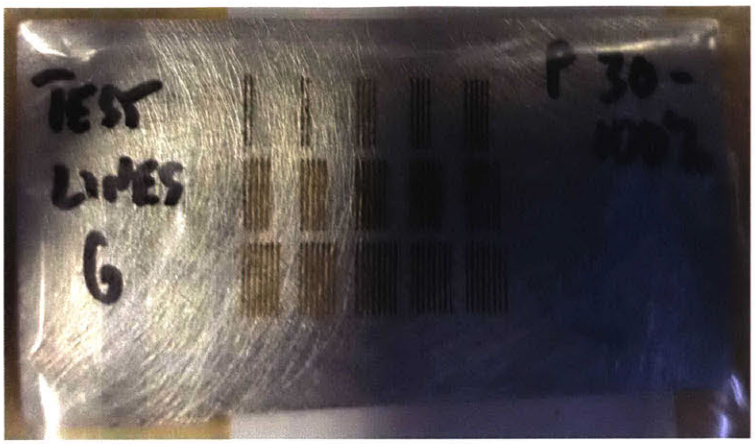

Figure 4-10: Test coupon after running the test pattern.

(a) (b) (c)

Figure 4-11: Optical images of tracks at (a) 30% power showing balling due to low energy input, (b) 40% power showing good track formation, and (c) 50% power showing ablation of the powder and sample surface due to high energy input.

4.5 Infill Rastering Test

Having demonstrated single-line feature generation, the final test was to replicate infilling a feature. To demonstrate the ability to infill a region, a series of rectangular raster regions were programmed. The goal of this test was to generate a solid, 2-dimensional feature.

4.5.1 Methodology

The methodology for the raster test was identical to the linear fusion testing save for the program executed and the surface preparation. Discussed further below, the samples surface was roughened with 80-grit sand paper before being cleaned. For the pattern, instead of running a series of lines, the system was programmed to linearly

raster-fill a series of rectangular patches. The test program used can be seen below in figure 4-12.

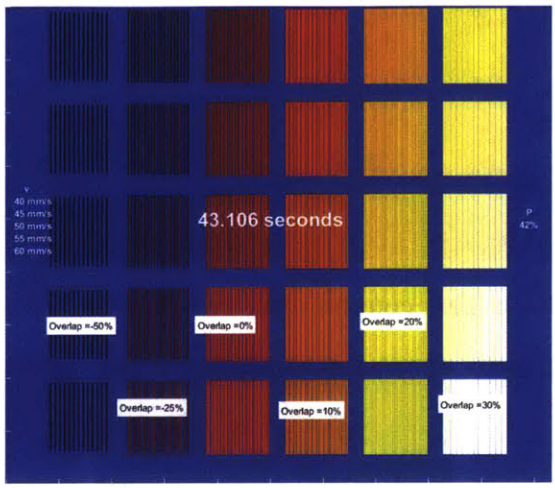

Figure 4-12: Raster test plan showing the variation in overlap spacing and scan speeds, but operating at a fixed power.

One complicating factor for this test sequence was that it had an additional degree of freedom when compared to the line test. In addition to varying the scan power and scan speed, the overlap of sequential passes comes into play. Since only two variable can be varied across the 2-dimensional grid of the test sample, the power was held constant at 42%, a value found to be reasonably effective in the line testing, and the scan speed and hatch spacing was varied. The overlap between lines was varied from -50%, meaning a 50% gap between lines, to 30% overlap while the scan speed was varied from $40\,\frac{\text{mm}}{\text{s}}$ to $60\,\frac{\text{mm}}{\text{s}}$ in $5\,\frac{\text{mm}}{\text{s}}$ increments.

4.5.2 Results and Discussion

Figures 4-13 through 4-15 show the optical microscope, stylus profilometer, and scanning electron microscope images of section of the raster test coupon.

The system performed as programmed and generated the rastering trajectory on the test sample. However, as can be seen from the images, the results were less a contiguous feature and more a series of partially fused lines and balled material.

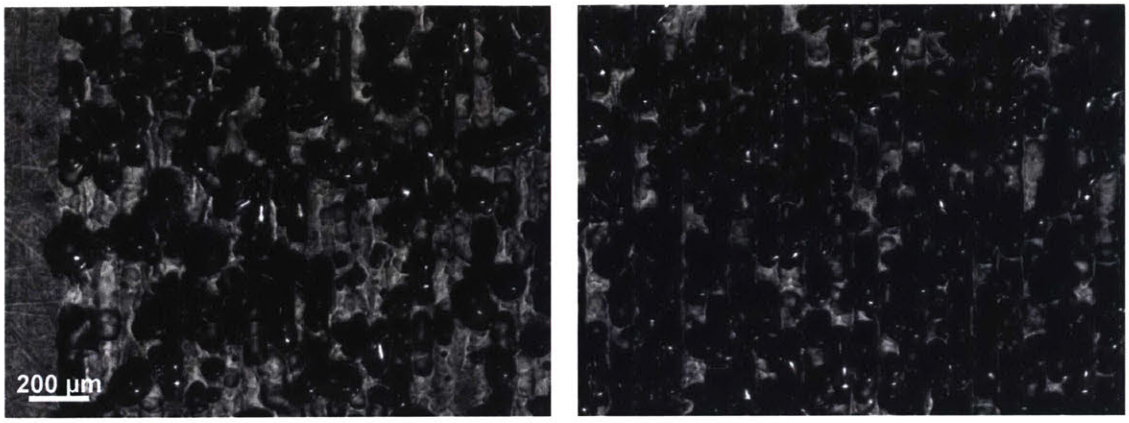

(a) (b)

Figure 4-13: Optical microscope images of two sections of the raster sample with (a) 50% overlap between lines and (b) 0% overlap.

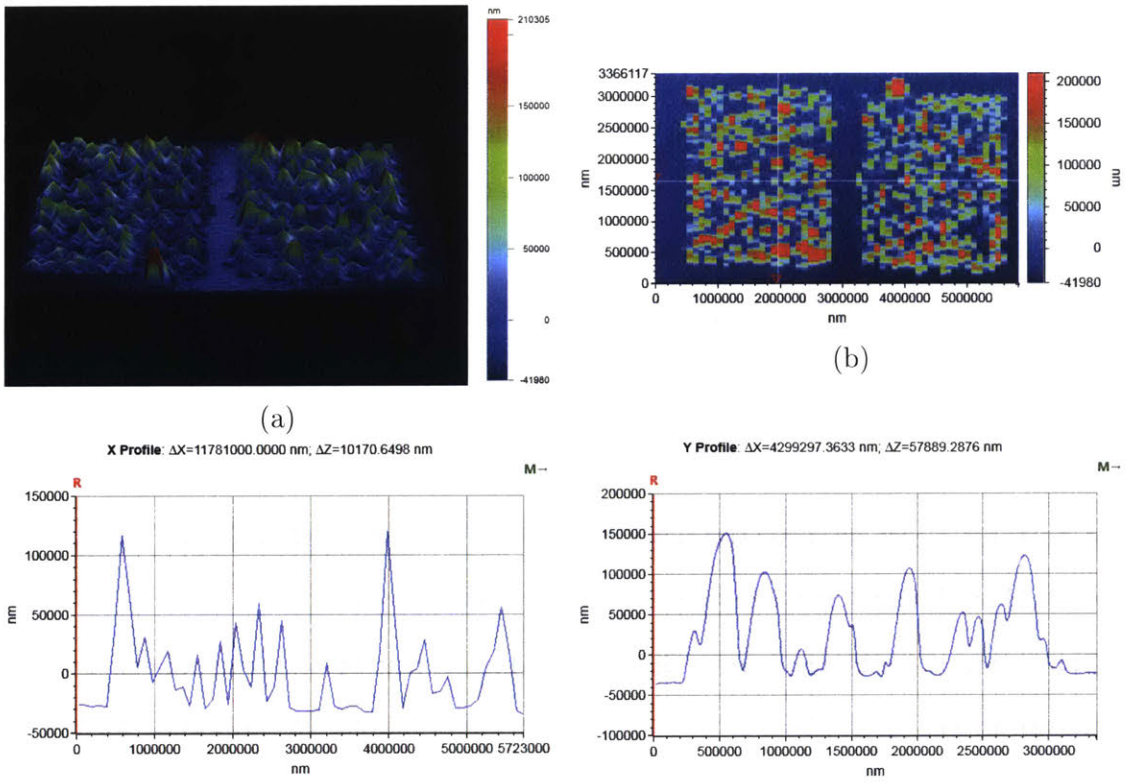

(a) (b)

(c) (d)

Figure 4-14: Stylus profilometer measurements of a section of the raster sample showing (a) two small patches from the sample, (b) a top-down view with two bisection lines, and (c-d) the height profiles along those bisections.

Given that the system executed the trajectories as programmed, the problem with developing a solidly fused infill region comes down to processing parameters.

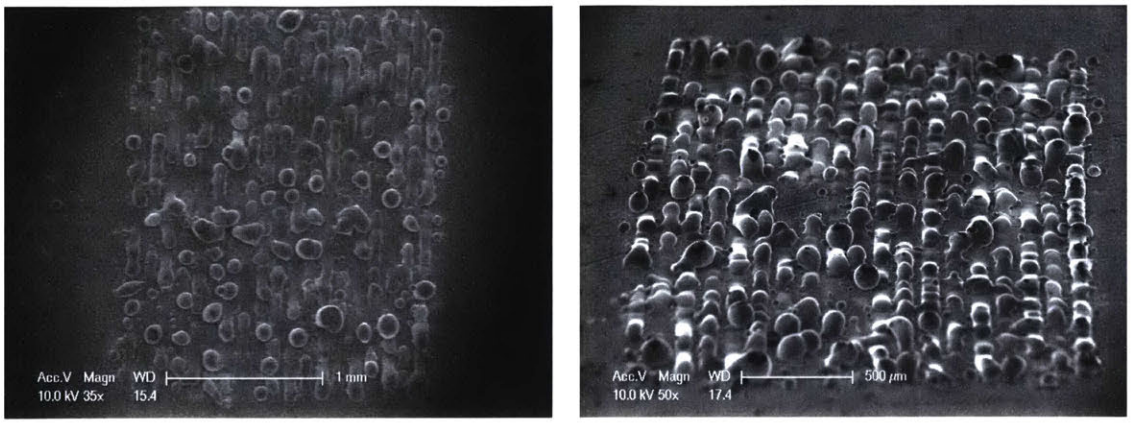

(a) (b)

Figure 4-15: SEM images of two sections of the raster sample with a 10% gap between lines, showing the irregular weld formation.

As discussed in section 2.3.1, the temperature of the environment plays an important role in the consistent fusion of the powder. Given that this experiment took place at ambient temperature, the lack of a heated substrate would impede the fusing of the material by retarding the wetting of the melt pool onto the substrate. Another contributing factor is that the powder was being fused directly on to the substrate. Fusing directly onto the substrate is the most difficult portion of the build process as the substrate acts as a large thermal sink which also impedes wetting of the melt pool onto the surface and to other melt tracks. A solution to these problems would be to perform a test on a heated powder bed that is considerably deeper, 500 µm or more, so that the melt track does not encounter the substrate.

One relevant build parameter discovered during testing was the role of surface roughness in the melt track adhering to the build plate. In exploring means to achieve better wetting of the melt track onto the substrate, one item considered was the buildup of surface contaminants not removed with the original cleaning sequence of isopropyl alcohol and acetone. In an effort to remove any surface oxidation, the sample was roughened with 80-grit sand paper. Figure 4-16 shows a pair of test coupons where one was as-delivered and the other was abraded with 80-grit sand paper before running a test pattern with a 100 µm layer of 316L stainless steel powder. While these results are largely anecdotal, there is a non-trivial decrease in balling

from the as-recieved surface to the roughened surface. This improvement in adhesion demonstrates the impact of surface preparation and warrants additional study.

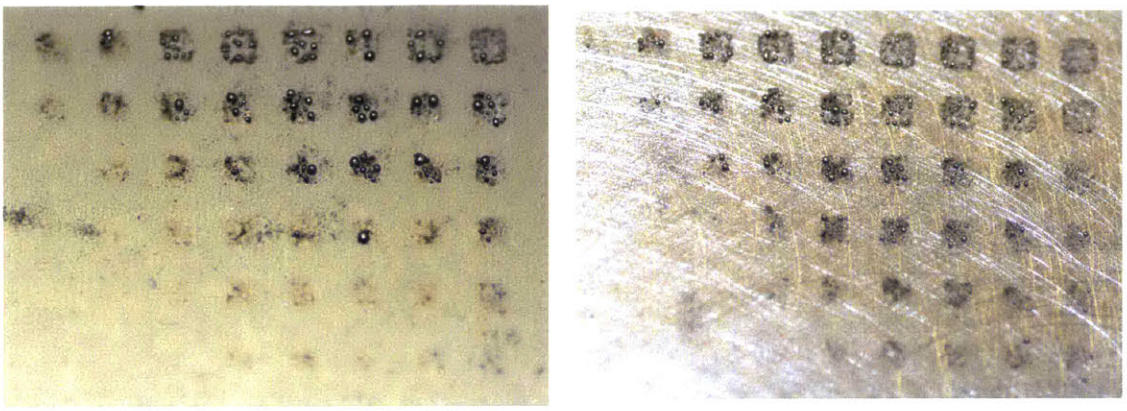

(a) (b)

Figure 4-16: Two test samples with their surfaces (a) as-delivered and (b) roughened with 80-grit sandpaper.

Despite the irregular features, the rastering test was a success. The intent of the test was to demonstrate that the system can infill a region by rastering across it, which was demonstrated. Further refinement of the process to create uniform, solid features is a matter of properly tuning the process parameters to achieve uniform track formation.

THIS PAGE INTENTIONALLY LEFT BLANK

Chapter 5

Conclusion and Future Work

5.1 Conclusion

Additive manufacturing is seeing widespread interest as a means to create freeform geometries and optimized structures impractical or impossible to make with traditional manufacturing practices. Powder bed fusion systems, one of the technologies capable of producing solid metal parts, is of particular interest as it can be used to create visual aids, manufacture customized and optimized tooling, and directly fabricate complex parts. One challenge in widespread research within powder bed fusion is the significant cost of commercial machines, and the closed-system nature of their implementation. The goal of this endeavor was to address this challenge by developing a low-cost and open-architecture laser powder bed fusion metal printer.

Captured within this work is a progression from a broad overview of manufacturing down to an experimental evaluation of an open-architecture powder bed fusion system. This work began with a broad overview of the various forms of additive manufacturing and their application within the manufacturing landscape. The powder bed fusion process was then closely examined along with the construction of the machines that perform it, and the parts that are produced by it. Given the understanding of how those systems operate, a laser powder bed fusion system was design from the ground up maximizing the use of commercial components and low-cost solutions. This system was augmented with a specially designed multi-layer recoating system capable of

being fitted within the tight confines of a pressure vessel. The work concludes by documenting experimental evaluation of the system demonstrating the ability to form solid weld beads.

5.2 Future Work

5.2.1 Exploration of Pressure in Powder Bed Fusion

Control of atmospheric pressure holds the potential for significant process improvement in powder bed fusion. The three primary routes this improvement can take are improved alloy materials, increase material envelope, and controllable melt pool dynamics. With alloyed materials, one challenge that crops up is that alloying elements with significantly different boiling points or vapor pressure have a tendency to dealloy during the powder bed fusion process and lose some of their properties. By increasing the process pressure, it may be possible to control the vaporization of the alloying components such that the alloy content can be maintained by elevating the boiling point. The increase in boiling point may also help with materials where the melting and boiling point are in close proximity, which leads to high material vaporization and poor part quality at atmospheric pressure. By separating those two temperature, an increase in pressure reduces the likelihood of material vaporization which contributes to better melt pool dynamics. Beyond materials with low boiling temperatures, that improvement in melt pool dynamics may also be seen in all materials, leading to higher part quality through higher density and lower defect rates.

5.2.2 Generation of Variable Density Parts

In the opposite direction of minimizing pores, controlling the density of a printed part through deliberate void creation opens the door to new structural functions. By generating a large number of voids within a region, essentially blowing bubbles, it can be converted into a foam-like structure. Given the high stiffness to strength ratio in metal foams, they are commonly used in weight-constrained environments such as

high performance automotive and aerospace applications. Additionally, low density combined with high stiffness means that metal and plastic foams make for excellent energy absorbers. Combine with 3D printing, these elements could be custom made into complex shapes and formed continuously with higher density structural members to seamlessly integrate shock absorption. Applied to the biomedical world through combination with biocompatible and biodegradable materials, these variable density structures could also be leveraged within medical implants to more closely model the stochastic open-cell structures generated by the body. By controllably generating what is often considered a defect, voids could allow for the creation of a new class of structures in powder bed fusion.

THIS PAGE INTENTIONALLY LEFT BLANK

Bibliography

[1] "Standard terminology for additive manufacturing - general principles - terminology," no. ISO / ASTM52900-15, 2015.

[2] A. Ambrosi and M. Pumera, "3d-printing technologies for electrochemical applications," *Chem. Soc. Rev.*, vol. 45, no. 10, pp. 2740–2755, 2016. DOI: 10.1039/c5cs00714c. [Online]. Available: http://dx.doi.org/10.1039/C5CS00714C.

[3] M. Cao and H. Frais. (Nov. 2015). Fused deposition modeling (fdm) and its main limitations. IC3Dprinters.com, Ed., [Online]. Available: https://consumables.ic3dprinters.com/fused-deposition-modeling-fdm-and-its-main-limitations/.

[4] replikat3d.com, Ed. (May 2013). Building bytes: 3d printed ceramic bricks, [Online]. Available: http://www.replikat3d.com/208/building-bytes-3d-printed-ceramic-bricks/.

[5] *What are the different technologies used in 3d printing?* http://www.dimension3.in/blog/?p=23, Blog, Jan. 2016.

[6] (2016). Polyjet materials, [Online]. Available: http://www.stratasys.com/materials/polyjet.

[7] E. Krassenstein. (2015). Virginia tech creates a binder jetting 3d printer that fabricates complex copper parts, [Online]. Available: https://3dprint.com/86321/3d-print-copper-virginia-tech/.

[8] M. Norfolk. (Jan. 2015). Hybrid 3d printing. Fabrisonic.com, Ed., [Online]. Available: http://fabrisonic.com/hybrid-3d-printing/.

[9] Sculpteo.com, Ed. Lom (laminated object manufacturing): 3d printing with layers of paper, [Online]. Available: https://www.sculpteo.com/en/glossary/lom-definition/.

[10] Carbon3D.com, Ed. Our process, [Online]. Available: http://carbon3d.com/clip-process.

[11] L. Pandell. (Oct. 2015). With this 3d printer, parts emerge from a plastic soup. Wired.com, Ed., [Online]. Available: https://www.wired.com/2015/10/carbon3d/.

[12] Zare-Prototyping.eu, Ed. Stereolithography (sla) - a reliable technology with an high level of detail, [Online]. Available: http://www.zare-prototyping.eu/en/stereolithography-sla.

[13] Simon. (Jun. 2015). Northwestern university study confirms 3d printed metal parts help reduce aircraft weight by 7%. 3ders.org, Ed., [Online]. Available: http://www.3ders.org/articles/20150606-northwestern-university-study-confirms-3d-printed-metal-parts-help-reduce-aircraft-weight.html.

[14] fraunhofer.de, Ed. (2013). EuroMold 2013 thread: Selective laser melting slm, [Online]. Available: http://www.ilt.fraunhofer.de/de/messen-und-veranstaltungen/messen/euromold-2013.html.

[15] DMGMori.com, Ed. All in 1: Laser deposition welding & milling -additive manufacturing in milling quality, [Online]. Available: http://us.dmgmori.com/products/lasertec/lasertec-additivemanufacturing/lasertec-65-3d.

[16] S. Grunewald. (Aug. 2015). Optomec brings metal 3d printing to latin america with new viwa partnership. 3dprint.com, Ed., [Online]. Available: https://3dprint.com/90240/optomec-viwa-partnership/.

[17] Sciaky.com, Ed. Make metal parts faster & cheaper than ever with electron beam additive manufacturing (ebam) systems or services, [Online]. Available: http://www.sciaky.com/additive-manufacturing/electron-beam-additive-manufacturing-technology.

[18] "Wohlers report 2015," Wohlers Associates, Inc., Tech. Rep., 2015, p. 315.

[19] T. Halterman. (Dec. 2014). Not your grandfather's trepanning - 3d printing makes complex facial and skull surgeries more effective. 3DPrint.com, Ed., [Online]. Available: https://3dprint.com/32191/3d-printing-for-skull-surgery/.

[20] K. Grens. (Jul. 2012). Is printing out your own lab equipment, molecular models, and drug compounds the wave of the future? The-Scientist.com, Ed., [Online]. Available: http://www.the-scientist.com/?articles.view/articleNo/32285/title/3-D-Printing/.

[21] E. Krassenstein. (Oct. 2014). Japanese company 3d prints a large working jet engine replica. 3DPrint.com, Ed., [Online]. Available: https://3dprint.com/17716/3d-printed-jet-engine/.

[22] L. Frick. (Jun. 2014). The difference between machined and 3d printed metal injection molds. MachineDesign.com, Ed., [Online]. Available: http://machinedesign.com/3d-printing/difference-between-machined-and-3d-printed-metal-injection-molds.

[23] J. Lewis. (Jun. 2015). 3d printing with jigs and fixtures. CADimensions.com, Ed., [Online]. Available: http://www.cadimensions.com/blog/item/119-3d-printing-with-jigs-and-fixtures.

[24] 3. P. M. for Casting. (May 2012). KiwiMill.com, Ed., [Online]. Available: https://www.kiwimill.com/blog/2012/05/04/3d-printed-mold-for-casting/.

[25] 3DSystems, Ed. Direct metal printing (dmp) enables ceee to manufacture lean and green heat exchanger, [Online]. Available: http://www.3dsystems.com/nb/node/9179.

[26] GEGlobalResearch.com, Ed. 3d printing creates new parts for aircraft engines, [Online]. Available: http://www.geglobalresearch.com/innovation/3d-printing-creates-new-parts-aircraft-engines.

[27] GEAviation.com, Ed. Our stories - additive manufacturing, [Online]. Available: http://www.geaviation.com/stories/.

[28] J. Reiss. (Jul. 2015). Vortech continues innovating products with new v-7 jt-b supercharger. EngienLabs.com, Ed., [Online]. Available: http://www.enginelabs.com/engine-tech/power-adders/vortech-continues-innovating-products-with-new-v-7-jt-b-supercharger/.

[29] J. Hagel, J. S. Brown, D. Kulasooriya, C. A. Giffi, and M. Chen. (Mar. 2015). The future of manufacturing - making things in a changing world, [Online]. Available: https://dupress.deloitte.com/dup-us-en/industry/manufacturing/future-of-manufacturing-industry.html.

[30] InsideMetalAdditiveManufacturing.com, Ed. (Mar. 2015). Design for slm - topology optimization of metallic structural nodes in architecture applications, [Online]. Available: http://www.insidemetaladditivemanufacturing.com/blog/design-for-slm-topology-optimisation-of-metallic-structural-nodes-in-architecture-applications.

[31] FossBytes.com, Ed. (Oct. 2015). Boeingś microlattice is worldś lightest metal made of 99.99% air, [Online]. Available: https://fossbytes.com/boeings-microlattice-worlds-lightest-metal-made-99-99-air/.

[32] S. Fish, S. Kubiak, W. Wroe, J. Booth, A. Bryant, and J. Beaman, "A high temperature polymer selective laser sintering testbed for controls research," in *Proc. 2015 Annual International Solid Freeform Fabrication Symposium (Austin, Texas, August 2015)*, vol. 26, Austin, Texas: The University of Texas at Austin, 2015.

[33] A. Bastian. (2016). OpenSLS, [Online]. Available: http://reprap.org/wiki/OpenSLS (visited on 05/13/2016).

[34] L. Hoppe. (2016). You-SLS, [Online]. Available: http://you-sls.com/ (visited on 05/13/2016).

[35] (2016). Norge systems, [Online]. Available: http://www.norgesystems.com/.

[36] (2016). Aurora labs 3D, [Online]. Available: http://auroralabs3d.com/.

[37] (2016). Sharebot, [Online]. Available: https://www.sharebot.it/.

[38] (2016). Sintratec, [Online]. Available: http://sintratec.com/.

[39] University of Texas at Austin, Ed. (Dec. 2012). Selective laser sintering, birth of an industry, [Online]. Available: http://www.me.utexas.edu/news/news/selective-laser-sintering-birth-of-an-industry.

[40] R. Housholder, *Molding process*, US Patent 4,247,508, Jan. 1981. [Online]. Available: https://www.google.com/patents/US4247508.

[41] J. Manriquez-Frayre and D. Bourell, "Proc. 1st international solid freeform fabrication symposium," 2009. [Online]. Available: https://sffsymposium.engr.utexas.edu/Manuscripts/1990/1990-09-Frayre.pdf.

[42] TU Clausthal, Ed. (2017). Institute of mechanical engineering research equipment, [Online]. Available: https://www.imw.tu-clausthal.de/en/research/equipment/.

[43] A. R. R. Bineli, A. P. G. Peres, A. L. Jardini, and R. Maciel Filho, "Direct metal laser sintering (dmls): Technology for design and construction of microreactors," in *6th Congress Obrasileiro de Engenharia de Fabrica ÇÃO*, vol. 11, 2011.

[44] A. V. Gusarov, I. Yadroitsev, P. Bertrand, and I. Smurov, "Model of radiation and heat transfer in laser-powder interaction zone at selective laser melting," *Journal of Heat Transfer*, vol. 131, 7 May 2009. DOI: 10.1115/1.3109245.

[45] S. A. Khairallah, A. T. Anderson, A. Rubenchik, and W. E. King, "Laser powder-bed fusion additive manufacturing: Physics of complex melt flow and formation mechanisms of pores, spatter, and denudation zones," *Acta Materialia*, vol. 108, pp. 36–45, Apr. 2016. DOI: 10.1016/j.actamat.2016.02.014. [Online]. Available: https://doi.org/10.1016%5C%2Fj.actamat.2016.02.014.

[46] F. Klocke, C. Wagner, and C. Ader, "Development of an integrated model for selective metal laser sintering," in *International Seminar on Manufacturing Systems, Progress in Virtual Manufacturing Systems*, Proceedings of the 36th CIRP (University des Saarlandes, Jun. 3–5, 2003), H. Bley, Ed., Saarbrucken, Germany: Schriftenreihe Produktionstechnik, 2003, pp. 387–392. [Online]. Available: http://publica.fraunhofer.de/dokumente/B-85578.html.

[47] R. Klein, *Laser welding of plastics*. Weinheim: Wiley-VCH, 2012, ISBN: 978-3-527-40972-3. [Online]. Available: https://application.wiley-vch.de/books/sample/3527409726_c01.pdf.

[48] J. Berkmanns and M. Faerber. Laser basics - facts about laser technology. Linde Group, Ed., [Online]. Available: http://www.laserdeal.com/techInfoFiles/_FactsAbout_LasertBasics..pdf.

[49] Laser Diode Selection, Ed. (Jun. 2014). Chapter 5: Application of Laser Diode, [Online]. Available: http://ldselection.com/tutorial/tag/laser-diode/.

[50] "Just add arcam," Arcam AB, Kroksltts Fabriker 27A, SE-431 37 Molndal, Sweden, Tech. Rep. [Online]. Available: http://www.arcam.com/wp-content/uploads/justaddbrochure-web.pdf.

[51] J. H. Wittke. (2015). Electron microanalysis core facility instrumentation, [Online]. Available: http://nau.edu/cefns/labs/electron-microprobe/glg-510-class-notes/instrumentation/.

[52] *redENERGY G4 Pulsed Fiber Laser Product Data Sheet*, 2016. [Online]. Available: http://www.spilasers.com/wp-content/uploads/2015/03/SM-S00219-Rev-G-G4-Datasheet_02_2016.pdf.

[53] The University of the Arts, Ed. (Mar. 2016). ID UArts Shop: Laser Cutter Documentation, [Online]. Available: https://docs.google.com/document/d/1DCowe7BTQTlNdeivvRR1eluac4GJLtsqKOGZ1HT-3xI/edit.

[54] *Large Beam Diameter Scanning Galvo Systems User Guide*, May 2016. [Online]. Available: https://www.thorlabs.com/drawings/ceb0de2a77eb8894-3BD50EFF-5056-0103-796D3ADDAB875B55/GVS012-Manual.pdf.

[55] ThorLabs, Ed. F-Theta Lens Tutorial, [Online]. Available: https://www.thorlabs.com/NewGroupPage9.cfm?objectgroup_id=6430.

[56] Newport Corporation, Ed. (2013). Using Newport XPS Universal Controller for Control of Galvo Scanner Head, [Online]. Available: https://www.newport.com/medias/sys_master/images/images/hba/he1/8797213491230/Motion-Tech-Note-XPS-Control-of-Galvo-Scanner.pdf.

[57] Farinia Group, Ed. Industrial production systems for metal additive manufacturing, [Online]. Available: http://www.farinia.com/additive-manufacturing/3d-technique/metal-additive-manufacturing-production-systems.

[58] The Shapeways Blog, Ed. (Oct. 2014). How much does it cost when you 3d print a thousand different parts all at once? [Online]. Available: https://www.shapeways.com/blog/archives/18174-how-much-does-it-cost-when-you-3d-print-a-thousand-different-parts-all-at-once.html.

[59] Physik Instrumente, Ed. M-413 high-load precision stage, [Online]. Available: https://www.physikinstrumente.com/en/products/linear-stages-and-actuators/stages-with-motor-screw-drives/m-413-high-load-precision-stage-701754/.

[60] B. Cox, *Selective laser sintering powder recycle system*, US Patent 7,887,316, Feb. 2011. [Online]. Available: https://www.google.com/patents/US7887316.

[61] D. Graf and M. Lindemann, *Verfahren und vorrichtung zur herstellung eines formkörpers durch selektives laserschmelzen*, EP Patent App. EP20,010,104,121, Aug. 2002. [Online]. Available: https://www.google.com/patents/EP1234625A1?cl=en22.

[62] S. Dadbakhsh and L. Hao, "Effect of layer thickness in selective laser melting on microstructure of al/5 wt.%fe2o3powder consolidated parts," *The Scientific World Journal*, vol. 2014, pp. 1–10, 2014. DOI: 10.1155/2014/106129. [Online]. Available: https://doi.org/10.1155%5C%2F2014%2F106129.

[63] M. M. Savalani and J. M. Pizarro, "Effect of preheat and layer thickness on selective laser melting (SLM) of magnesium," *Rapid Prototyping Journal*, vol. 22, no. 1, pp. 115–122, Jan. 2016. DOI: 10.1108/rpj-07-2013-0076. [Online]. Available: https://doi.org/10.1108%5C%2Frpj-07-2013-0076.

[64] M. Ma, Z. Wang, M. Gao, and X. Zeng, "Layer thickness dependence of performance in high-power selective laser melting of 1cr18ni9ti stainless steel," *Journal of Materials Processing Technology*, vol. 215, pp. 142–150, Jan. 2015. DOI: 10.1016/j.jmatprotec.2014.07.034. [Online]. Available: https://doi.org/10.1016%5C%2Fj.jmatprotec.2014.07.034.

[65] T. Mattes, A. Lohner, and C. Wilkening, *Method and apparatus for producing a three-dimensional object*, US Patent 5,730,925, Mar. 1998. [Online]. Available: https://www.google.com/patents/US5730925.

[66] J. Beaman and C. Deckard, *Selective laser sintering with assisted powder handling*, US Patent 4,938,816, Jul. 1990. [Online]. Available: https://www.google.com/patents/US4938816.

[67] A. Gasser, W. Meiners, and K. Wissenbach, *Vorrichtung für das selektive laserschmelzen zur herstellung eines formkörpers*, EP Patent 1,144,146, Mar. 2003. [Online]. Available: http://google.com/patents/EP1144146B1?cl=zh-cn.

[68] B. V. der Schueren and J. Kruth, "Powder deposition in selective metal powder sintering," *Rapid Prototyping Journal*, vol. 1, no. 3, pp. 23–31, Sep. 1995. DOI: 10.1108/13552549510094241. [Online]. Available: https://doi.org/10.1108%5C%2F13552549510094241.

[69] P. Regenfuss, L. Hartwig, S. Klotzer, R. Ebert, and H. Exner, "Microparts by a novel modification of selective laser sintering," in *Society of Manufacturing Engineers, Conference on Rapid Prototyping and Manufacturing*, Chicago, IL, 2003.

[70] R. Mertens, B. Vrancken, N. Holmstock, Y. Kinds, J.-P. Kruth, and J. V. Humbeeck, "Influence of powder bed preheating on microstructure and mechanical properties of h13 tool steel SLM parts," *Physics Procedia*, vol. 83, pp. 882–890, 2016. DOI: 10.1016/j.phpro.2016.08.092. [Online]. Available: https://doi.org/10.1016%5C%2Fj.phpro.2016.08.092.

[71] D. Buchbinder, W. Meiners, N. Pirch, K. Wissenbach, and J. Schrage, "Investigation on reducing distortion by preheating during manufacture of aluminum components using selective laser melting," *Journal of Laser Applications*, vol. 26, no. 1, p. 012 004, Feb. 2014. DOI: 10.2351/1.4828755. [Online]. Available: https://doi.org/10.2351%5C%2F1.4828755.

[72] T. Burkert and A. Fischer, "The effects of heat balance on the void formation within marage 300 processed by selective laser melting," in *26th Annual International Solid Freeform Fabrication Symposium*, (University of Texas at Austin), Austin, Texas, USA, 2015, pp. 745–757. [Online]. Available: https://sffsymposium.engr.utexas.edu/sites/default/files/2015/2015-61-Burkert.pdf.

[73] C. Hauser, T. Childs, K. Dalgarno, and R. Eane, "Atmospheric control during direct selective laser sintering of stainless steel 314s powder," in *10th Annual International Solid Freeform Fabrication Symposium*, 1999, pp. 265–272. [Online]. Available: https://sffsymposium.engr.utexas.edu/Manuscripts/1999/1999-030-Hauser.pdf.

[74] M. Beck, P. Berger, and H. Hugel, "The effect of plasma formation on beam focusing in deep penetration welding with CO 2 lasers," *Journal of Physics D: Applied Physics*, vol. 28, no. 12, pp. 2430–2442, Dec. 1995. DOI: 10.1088/0022-3727/28/12/007. [Online]. Available: https://doi.org/10.1088%5C%2F0022-3727%5C%2F28%5C%2F12%5C%2F007.

[75] W. Meiners, *Direct selective laser sintering of one-component metallic materials*. 1993, ISBN: 3826565711.

[76] J. Ion, *Laser processing of engineering materials: Principles, procedure and industrial application*. Butterworth-Heinemann, 2005, ISBN: 978-0-7506-6079-2.

[77] A. Ladewig, G. Schlick, M. Fisser, V. Schulze, and U. Glatzel, "Influence of the shielding gas flow on the removal of process by-products in the selective laser melting process," *Additive Manufacturing*, vol. 10, pp. 1–9, Apr. 2016. DOI: 10.1016/j.addma.2016.01.004. [Online]. Available: https://doi.org/10.1016%5C%2Fj.addma.2016.01.004.

[78] P. Y. Shcheglov, A. V. Gumenyuk, I. B. Gornushkin, M. Rethmeier, and V. N. Petrovskiy, "Vapor–plasma plume investigation during high-power fiber laser welding," *Laser Physics*, vol. 23, no. 1, p. 016 001, Nov. 2012. DOI: 10.1088/1054-660x/23/1/016001. [Online]. Available: https://doi.org/10.1088%5C%2F1054-660x%5C%2F23%5C%2F1%5C%2F016001.

[79] J. Greses, P. A. Hilton, C. Y. Barlow, and W. M. Steen, "Plume attenuation under high power nd:yttritium–aluminum–garnet laser welding," *Journal of Laser Applications*, vol. 16, no. 1, pp. 9–15, Feb. 2004. DOI: 10.2351/1.1642636. [Online]. Available: https://doi.org/10.2351%5C%2F1.1642636.

[80] I. Yadroitsev, I. Yadroitsava, P. Bertrand, and I. Smurov, "Factor analysis of selective laser melting process parameters and geometrical characteristics of synthesized single tracks," *Rapid Prototyping Journal*, vol. 18, no. 3, pp. 201–208, Apr. 2012. DOI: 10.1108/13552541211218117. [Online]. Available: https://doi.org/10.1108%5C%2F13552541211218117.

[81] B. Ferrar, L. Mullen, E. Jones, R. Stamp, and C. Sutcliffe, "Gas flow effects on selective laser melting (SLM) manufacturing performance," *Journal of Materials Processing Technology*, vol. 212, no. 2, pp. 355–364, Feb. 2012. DOI: 10.1016/j.jmatprotec.2011.09.020. [Online]. Available: https://doi.org/10.1016%5C%2Fj.jmatprotec.2011.09.020.

[82] W. J. Sames, F. A. List, S. Pannala, R. R. Dehoff, and S. S. Babu, "The metallurgy and processing science of metal additive manufacturing," *International Materials Reviews*, vol. 61, no. 5, pp. 315–360, 2016. DOI: 10.1080/09506608.2015.1116649.

[83] T. Craeghs, F. Bechmann, S. Berumen, and J.-P. Kruth, "Feedback control of layerwise laser melting using optical sensors," *Physics Procedia*, vol. 5, pp. 505–514, 2010. DOI: 10.1016/j.phpro.2010.08.078. [Online]. Available: https://doi.org/10.1016%5C%2Fj.phpro.2010.08.078.

[84] T. G. Spears and S. A. Gold, "In-process sensing in selective laser melting (SLM) additive manufacturing," *Integrating Materials and Manufacturing Innovation*, vol. 5, no. 1, Feb. 2016. DOI: 10.1186/s40192-016-0045-4. [Online]. Available: https://doi.org/10.1186%5C%2Fs40192-016-0045-4.

[85] J. Mireles, C. Terrazas, S. M. Gaytan, D. A. Roberson, and R. B. Wicker, "Closed-loop automatic feedback control in electron beam melting," *The International Journal of Advanced Manufacturing Technology*, vol. 78, no. 5-8, pp. 1193–1199, Jan. 2015. DOI: 10.1007/s00170-014-6708-4. [Online]. Available: https://doi.org/10.1007%2Fs00170-014-6708-4.

[86] D. D. Gu, W. Meiners, K. Wissenbach, and R. Poprawe, "Laser additive manufacturing of metallic components: Materials, processes and mechanisms," *International Materials Reviews*, vol. 57, no. 3, pp. 133–164, May 2012. DOI: 10.1179/1743280411y.0000000014. [Online]. Available: https://doi.org/10.1179%2F1743280411y.0000000014.

[87] GPI Prototype & Manufacturing Services, Ed. Selective Laser Sintering - SLS Materials, [Online]. Available: http://gpiprototype.com/selective-laser-sintering-sls-materials.html.

[88] W. Sames, F. Medina, W. Peter, S. Babu, and R. Dehoff, "Effect of process control and powder quality on inconel 718 produced using electron beam melting," in *8th International Symposium on Superalloy 718 and Derivatives*, Wiley-Blackwell, Dec. 2014, pp. 409–423. DOI: 10.1002/9781119016854.ch32. [Online]. Available: https://doi.org/10.1002%2F9781119016854.ch32.

[89] Advanced Powders & Coatings, Ed. (2017). Designed for additive manufacturing, [Online]. Available: http://advancedpowders.com/our-plasma-atomized-powders/spherical-powders-designed-for-additive-manufacturing/.

[90] N. K. Tolochko, Y. V. Khlopkov, S. E. Mozzharov, N. V. Sobolenko, and I. A. Yadroitsev, "Measurement of the absorption coefficient of freely poured one-component metallic powders and its change during laser sintering," *Powder Metallurgy and Metal Ceramics*, vol. 36, no. 7-8, pp. 433–437, Jul. 1997. DOI: 10.1007/bf02676008. [Online]. Available: https://doi.org/10.1007%2Fbf02676008.

[91] B. Liu, R. Wildman, C. Tuck, I. Ashcroft, and R. Hague, "Investigation the effect of particle size distribution on processing parameters optimisation in selective laser melting process," in *22nd Annual International Solid Freeform Fabrication Symposium*, 2011. [Online]. Available: https://sffsymposium.engr.utexas.edu/Manuscripts/2011/2011-18-Liu.pdf.

[92] Croft Additive Manufacturing, Ed. How does it work? The basics explained of SLM, [Online]. Available: http://www.croftam.co.uk/how-does-it-work/.

[93] D. Wang, Y. Yang, Z. Yi, and X. Su, "Research on the fabricating quality optimization of the overhanging surface in SLM process," *The International Journal of Advanced Manufacturing Technology*, vol. 65, no. 9-12, pp. 1471–1484, Jun. 2012. DOI: 10.1007/s00170-012-4271-4. [Online]. Available: https://doi.org/10.1007%2Fs00170-012-4271-4.

[94] R. Mertens, S. Clijsters, K. Kempen, and J.-P. Kruth, "Optimization of scan strategies in selective laser melting of aluminum parts with downfacing areas," *Journal of Manufacturing Science and Engineering*, vol. 136, no. 6, p. 061 012, Oct. 2014. DOI: 10.1115/1.4028620. [Online]. Available: https://doi.org/10.1115%2F1.4028620.

[95] W. J. Sames, "Additive manufacturing of inconel 718 using electron beam melting," PhD thesis, Texas A&M University, 2015.

[96] "M line factory - metal laser melting machine for series production," Concept Laser GmbH, Tech. Rep. [Online]. Available: https://www.concept-laser.de/fileadmin/Neue_Produkte/1610_M_LINE_FACTORY-EN.pdf.

[97] "Slm 500," SLM Solutions, Tech. Rep. [Online]. Available: https://slm-solutions.com/sites/default/files/attachment/page/2016/11/w_slm500_en.pdf.

[98] "Direct metal printers," 3D Systems, Tech. Rep. [Online]. Available: http://www.3dsystems.com/sites/www.3dsystems.com/files/dmp_brochure_09.20.16_usen_web.pdf.

[99] "Additive manufacturing - selective electron beam melting," Fraunhofer IFAM, Tech. Rep. [Online]. Available: http://www.ifam.fraunhofer.de/content/dam/ifam/en/documents/dd/Infobl%C3%A4tter/additive_manufacturing-electron_beam_melting_fraunhofer_ifam_dresden.pdf.

[100] "Electron beam melting," additively, Tech. Rep. [Online]. Available: https://www.additively.com/en/learn-about/electron-beam-melting.

[101] L. Thijs, F. Verhaeghe, T. Craeghs, J. V. Humbeeck, and J.-P. Kruth, "A study of the microstructural evolution during selective laser melting of ti–6al–4v," *Acta Materialia*, vol. 58, no. 9, pp. 3303–3312, May 2010. DOI: 10.1016/j.actamat.2010.02.004. [Online]. Available: https://doi.org/10.1016%2Fj.actamat.2010.02.004.

[102] S. S. Al-Bermani, M. L. Blackmore, W. Zhang, and I. Todd, "The origin of microstructural diversity, texture, and mechanical properties in electron beam melted ti-6al-4v," *Metallurgical and Materials Transactions A*, vol. 41, no. 13, pp. 3422–3434, Aug. 2010. DOI: 10.1007/s11661-010-0397-x. [Online]. Available: https://doi.org/10.1007%2Fs11661-010-0397-x.

[103] P. Edwards and M. Ramulu, "Fatigue performance evaluation of selective laser melted ti–6al–4v," *Materials Science and Engineering: A*, vol. 598, pp. 327–337, Mar. 2014. DOI: 10.1016/j.msea.2014.01.041. [Online]. Available: https://doi.org/10.1016%2Fj.msea.2014.01.041.

[104] L. N. Carter, C. Martin, P. J. Withers, and M. M. Attallah, "The influence of the laser scan strategy on grain structure and cracking behaviour in SLM powder-bed fabricated nickel superalloy," *Journal of Alloys and Compounds*, vol. 615, pp. 338–347, Dec. 2014. DOI: 10.1016/j.jallcom.2014.06.172. [Online]. Available: https://doi.org/10.1016%2Fj.jallcom.2014.06.172.

[105] L. Thijs, K. Kempen, J.-P. Kruth, and J. V. Humbeeck, "Fine-structured aluminium products with controllable texture by selective laser melting of pre-alloyed AlSi10mg powder," *Acta Materialia*, vol. 61, no. 5, pp. 1809–1819, Mar. 2013. DOI: 10.1016/j.actamat.2012.11.052. [Online]. Available: https://doi.org/10.1016%2Fj.actamat.2012.11.052.

[106] C. Ng, M. Savalani, M. Lau, and H. Man, "Microstructure and mechanical properties of selective laser melted magnesium," *Applied Surface Science*, vol. 257, no. 17, pp. 7447–7454, 2011, ISSN: 0169-4332. DOI: http://dx.doi.org/10.1016/j.apsusc.2011.03.004. [Online]. Available: http://www.sciencedirect.com/science/article/pii/S0169433211003576.

[107] J. Mireles, C. Terrazas, S. M. Gaytan, D. A. Roberson, and R. B. Wicker, "Closed-loop automatic feedback control in electron beam melting," *The International Journal of Advanced Manufacturing Technology*, vol. 78, no. 5-8, pp. 1193–1199, Jan. 2015. DOI: 10.1007/s00170-014-6708-4. [Online]. Available: https://doi.org/10.1007%5C%2Fs00170-014-6708-4.

[108] R. R. Dehoff, M. M. Kirka, W. J. Sames, H. Bilheux, A. S. Tremsin, L. E. Lowe, and S. S. Babu, "Site specific control of crystallographic grain orientation through electron beam additive manufacturing," *Materials Science and Technology*, vol. 31, no. 8, pp. 931–938, Dec. 2014. DOI: 10.1179/1743284714y.0000000734. [Online]. Available: https://doi.org/10.1179%5C%2F1743284714y.0000000734.

[109] S. A. Khairallah, A. T. Anderson, A. Rubenchik, and W. E. King, "Laser powder-bed fusion additive manufacturing: Physics of complex melt flow and formation mechanisms of pores, spatter, and denudation zones," *Acta Materialia*, vol. 108, pp. 36–45, Apr. 2016. DOI: 10.1016/j.actamat.2016.02.014. [Online]. Available: https://doi.org/10.1016%2Fj.actamat.2016.02.014.

[110] D. Dubé, M. Fiset, A. Couture, and I. Nakatsugawa, "Characterization and performance of laser melted AZ91d and AM60b," *Materials Science and Engineering: A*, vol. 299, no. 1-2, pp. 38–45, Feb. 2001. DOI: 10.1016/s0921-5093(00)01414-3. [Online]. Available: https://doi.org/10.1016%5C%2Fs0921-5093%5C%2800%5C%2901414-3.

[111] L. Jauer, B. Julich, M. Voshage, and W. Meiners, "Selective laser melting of magnesium alloys," *European Cells and Materials*, vol. 30, no. 8, 2015.

[112] M. Gieseke, C. Noelke, S. Kaierle, V. Wesling, and H. Haferkamp, "Selective laser melting of magnesium and magnesium alloys," in *Magnesium Technology 2013*, Wiley-Blackwell, Feb. 2013, pp. 65–68. DOI: 10.1002/9781118663004.ch11. [Online]. Available: https://doi.org/10.1002%5C%2F9781118663004.ch11.

[113] "Magnesium basics - physical properties," International Magnesium Association, Tech. Rep., 2016. [Online]. Available: http://www.gly.uga.edu/railsback/FundamentalsIndex.html.

[114] D. Errandonea, Y. Meng, D. Hausermann, and T. Uchida, "Study of the phase transformations and equation of state of magnesium by synchrotron x-ray diffraction," *Journal of Physics: Condensed Matter*, vol. 15, no. 8, p. 1277, 2003. [Online]. Available: http://stacks.iop.org/0953-8984/15/i=8/a=312.

[115] W. P. Gilbreath, "The vapor pressure of magnesium between 223 deg and 385 deg c," Tech. Rep., Mar. 1965, p. 11.

[116] F. Witte, "The history of biodegradable magnesium implants - a review," *Acta Biomaterialia*, vol. 6, no. 5, pp. 1680–1692, 2010.

[117] L. E. Murr, S. M. Gaytan, F. Medina, H. Lopez, E. Martinez, B. I. Machado, D. H. Hernandez, L. Martinez, M. I. Lopez, R. B. Wicker, and J. Bracke, "Next-generation biomedical implants using additive manufacturing of complex, cellular and functional mesh arrays," *Philosophical Transactions of the Royal Society of London A: Mathematical, Physical and Engineering Sciences*, vol. 368, no. 1917, pp. 1999–2032, 2010, ISSN: 1364-503X. DOI: 10.1098/rsta.2010.0010. [Online]. Available: http://rsta.royalsocietypublishing.org/content/368/1917/1999.

[118] T. Adams. (May 2013). Reviewing the development of metallic foams with john banhart, [Online]. Available: http://www.advancedsciencenews.com/reviewing-the-development-of-metallic-foams-with-john-banhart/.

[119] S. Szyniszewski. Research - Metallic Foam Sandwich Panels, [Online]. Available: http://www.szyniszewski.com/research/.

[120] Z. Y. Wang, Y. F. Shen, and D. D. Gu, "Development of porous 316l stainless steel with novel structures by selective laser melting," *Powder Metallurgy*, vol. 54, no. 3, pp. 225–230, Jul. 2011. DOI: 10.1179/003258909x12450768326947. [Online]. Available: https://doi.org/10.1179%5C%2F003258909x12450768326947.

[121] Y. F. Shen, D. D. Gu, and P. Wu, "Development of porous 316l stainless steel with controllable microcellular features using selective laser melting," *Materials Science and Technology*, vol. 24, no. 12, pp. 1501–1505, Dec. 2008. DOI: 10.1179/174328408x287691. [Online]. Available: https://doi.org/10.1179%5C%2F174328408x287691.

[122] W. E. King, H. D. Barth, V. M. Castillo, G. F. Gallegos, J. W. Gibbs, D. E. Hahn, C. Kamath, and A. M. Rubenchik, "Observation of keyhole-mode laser melting in laser powder-bed fusion additive manufacturing," *Journal of Materials Processing Technology*, vol. 214, no. 12, pp. 2915–2925, Dec. 2014. DOI: 10.1016/j.jmatprotec.2014.06.005. [Online]. Available: https://doi.org/10.1016%5C%2Fj.jmatprotec.2014.06.005.

[123] *Mini diode laser system*, DILAS Industrial Laser Systems, Galileo-Galilei-Strabe 10, 55129 Mainz,Germany. [Online]. Available: http://dilas.com/assets/media/products/DILAS-ILS_MiniDLSystem.pdf.

[124] I. Yadroitsev, P. Bertrand, and I. Smurov, "Parametric analysis of the selective laser melting process," *Applied Surface Science*, vol. 253, no. 19, pp. 8064–8069, Jul. 2007. DOI: 10.1016/j.apsusc.2007.02.088. [Online]. Available: https://doi.org/10.1016%5C%2Fj.apsusc.2007.02.088.

[125] STM32 Nucleo-32 development board with STM32F303K8 MCU, [Online]. Available: http://www.st.com/en/evaluation-tools/nucleo-f303k8.html.

[126] Arduino.cc, [Online]. Available: https://www.arduino.cc/ (visited on 06/20/2016).

[127] [Online]. Available: https://www.mbed.com/ (visited on 06/20/2016).

[128] S. Electronics. EasyDriver, [Online]. Available: https://www.sparkfun.com/products/12779.

[129] MikroElektronika. CAN SPI click 5V, [Online]. Available: https://shop.mikroe.com/click/interface/can-spi-5v.

[130] M. McCauley, *AccelStepper*, http://www.airspayce.com/mikem/arduino/AccelStepper/, 2010–2016.

[131] D. Austin, "Generate stepper-motor speed profiles in real time," *EE Times-India*, Jan. 2005. [Online]. Available: http://web.archive.org/web/20140705143928/http://fab.cba.mit.edu/classes/MIT/961.09/projects/i0/Stepper_Motor_Speed_Profile.pdf.

[132] Python Software Foundation. Python, [Online]. Available: https://www.python.org/.

[133] R. C. Ltd. Pyqt, [Online]. Available: https://riverbankcomputing.com/software/pyqt/intro.

[134] The Qt Company. Qt5, [Online]. Available: https://www.qt.io/developers/.

[135] Sublime Text 3, [Online]. Available: https://www.sublimetext.com/3 (visited on 06/18/2016).

[136] J. Damask, *Polarization optics in telecommunications*. New York: Springer, 2005, ISBN: 0-387-22493-9.

[137] H. Urey, "Spot size, depth-of-focus, and diffraction ring intensity formulas for truncated gaussian beams," *Appl. Opt.*, vol. 43, no. 3, pp. 620–625, Jan. 2004. DOI: 10.1364/AO.43.000620. [Online]. Available: http://ao.osa.org/abstract.cfm?URI=ao-43-3-620.

[138] A. J. Hart, A. Slocum, and P. Willoughby, "Kinematic coupling interchangeability," *Precision Engineering*, vol. 28, no. 1, pp. 1–15, Jan. 2004. DOI: 10.1016/s0141-6359(03)00071-0. [Online]. Available: https://doi.org/10.1016%2Fs0141-6359%2803%2900071-0.

[139] Slic3r. G-code Generator for 3D Printers, [Online]. Available: http://slic3r.org/.

[140] K. P. Co., Ed. Understanding vertical linear stage specifications, [Online]. Available: http://www.kohzuprecision.com/technology/positioning-stages/manual-stages/z-stage/.